Magnetotelluric Investigations of the Tintina Fault Zone for Geothermal Exploration at Watson Lake, Yukon

By

Erich George Slobodian

A thesis submitted in partial fulfillment of the requirements for the degree of

Master of Science

In

Geophysics

Department of Physics

University of Alberta

Abstract

Geothermal energy is being investigated as a renewable source of electricity and heat production for communities in northern Canada. The successful development of a geothermal energy project requires three key components: (1) there must be a source of sufficient heat at near-surface depths. Typically, geothermal projects require temperatures of at least 150°C for efficient electricity production while lower temperature resources can be directly used for heating, (2) the rock must contain pore fluids that can be used to transport the heat to the surface through pores, fractures, and boreholes, (3) the host rock must have sufficient permeability such that fluids can move easily through the subsurface in pores and fractures.

The community of Watson Lake, Yukon may be a potential site for a geothermal energy project. Studies have show that the area surrounding Watson Lake has high values of surface heat flow and temperatures that may exceed 200°C at depths of 6 km below the surface (Majorowicz and Grasby, 2014). The nearby Tintina Fault zone, a dextral strike-slip fault system, may represent a zone of elevated porosity through which pore fluids could flow and allow heat to be extracted for the production of electricity and heat. However, the exact location of the Tintina Fault zone is poorly constrained due to coverage by glacial deposits. Geophysical methods such as the magnetotelluric method must be utilized to better constrain the location of the Tintina Fault and to identify potential geothermal reservoirs within the fault zone.

The magnetotelluric (MT) method measures naturally occurring variations of Earth's magnetic and electric fields. Analysis of the time variations of these fields can be used to determine the subsurface resistivity structure of the Earth. The MT method is able to locate subsurface areas of low electrical resistivity that may be due to trapped pore fluids in the crust and upper mantle. This makes it one of the preferred geophysical methods for geothermal exploration.

During July and August of 2021, 36 broadband MT stations were deployed near the community of Watson Lake. These MT stations recorded time series data that produce apparent resistivity, phase, and tipper data in the frequency range of 0.001 – 100 Hz when transformed to the frequency domain. The data were filtered to remove noise from the signals. These data were then utilized in a 3D MT inversion to create a model of the spatial variation of electrical resistivity in three dimensions. This was done using the ModEM algorithm developed by Kelbert et al., (2014), which was run on the Cedar computing cluster provided by the Digital Research Alliance of Canada.

The resulting electrical resistivity model displays four key features of interest for geothermal development at Watson Lake. Two conducting bodies were resolved by the inversion, with electrical resistivity values in the ranges of 1 – 10 Ωm and 10 – 30 Ωm respectively. These features were named C1 and C2. Conductor C1 is located between Highway 37 and the Liard River and is approximately 15 km wide. The top of the conductor is situated at 500 m below sea level, and it extends to a depth of 3 km below sea level. Conductor C2 is located North of the Alaska Highway and East of Watson Lake, with a width of 3 km. The top of C2 is situated at 500 m below sea level and it extends to a depth of 10 km below sea level. Two resistive features were resolved with resistivity in the range of 300 – 1000 Ωm and named R1 and R2. It was determined that the low resistivity of C1 and C2 were most likely the result of either saline pore fluids or interconnected graphite films present within the block of rock located within the Tintina Fault zone. Analysis of the phase tensor data indicates that the Tintina Fault has a geologic strike of between N30°W and N45°W and is likely located further west than previously thought (Yukon Geological Survey, 2022).

Future studies are necessary to better characterize the geothermal potential of Watson Lake. These should include expanding the grid of MT stations to better constrain the features detected by the MT study and drilling test wells to sample pore fluids as well as measure the thermal gradient of the area.

Acknowledgements

I would firstly like to thank my supervisor, Martyn Unsworth, for his help and guidance throughout the entire process of researching and writing my thesis. This thesis would also not have been possible without the funding provided by Liard First Nation, Northern REACHE (Indigenous and Northern Affairs Canada), the Barkley Group, the Yukon Geological Survey, and Future Energy Systems. I would like to thank Travis Stewart, Zuneza Cove, Harlan Schilling, Tanya Ball, John Ebell, Maurice Colpron and Carolyn Relf and many others for making this project possible. I would also like to thank my fellow graduate students, Cedar Hanneson and Zoë Vestrum for their help in the MT station deployment, and for providing assistance and feedback during the data analysis and writing stages of this thesis, as well as the other members of our research group: Brandon Chase, Megan Caston, Javier Gonzalez, and Keytash Moshtaghian, for their helpful advice and moral support along the way. I would also like to thank my parents and siblings who supported me throughout my university experience. I would like to express gratitude to Jeff Witter, with whom I had insightful discussions regarding the comparison of the MT and gravity data. Robbie Porter, who provided transportation along the Liard River during data collection, is also thanked. Lastly, I would like to express thanks to the Digital Research Alliance of Canada for allowing me to use their Cedar computing cluster to run the 3-D inversions, and the authors of the ModEM inversion algorithm for allowing me to use their codes for 3-D inversions.

Table of Contents

List of Tables

List of Figures

Chapter 1: Introduction

1.1 Renewable Energy in Canada

There is a growing concern to reduce carbon emissions from heat and electricity generation in Canada. Canada currently produces electricity mainly through a combination of hydroelectric power, nuclear power, and burning fossil fuels, with renewable energy sources such as wind and solar also being used in a limited capacity (Canada Energy Regulator, 2023). Expanding the use of electricity production methods with low carbon emissions is critical for reducing overall carbon emissions in Canada. Canada's current usage of renewable energy methods to produce electricity is detailed below.

Hydroelectric energy production is the main source of electricity production in Canada, mainly in British Columbia and the Eastern provinces including Ontario and Quebec. This form of electricity production has minimal carbon emissions, but there are other environmental concerns associated with the creation of hydroelectric plants such as flooding and the impact on wildlife. In addition, the construction of a hydroelectric plant requires a reliable water supply, limiting the areas where a plant could be built.

Wind turbines and solar panels are other means of generating electricity with low carbon emissions. However, both methods suffer from the same main issues: (1) the intermittency of power generation, as the energy source is dependant on the weather and time of day, and (2) the necessity of long-term energy storage for times of peak grid demand. In addition, the production and disposal of solar panels has a number of environmental concerns.

Much of the energy produced in Canada is utilized for heating purposes, such as residential heating or in industrial processes. According to Natural Resources Canada (2022), in 2019 the average Canadian home utilized 63.6% of its energy consumption for space heating. Residential space heating can be in the form of electrically powered heaters, or through the direct combustion of fossil fuels and wood products. These processes make a considerable contribution to the country's carbon emissions. Alternative forms of renewable energy-based heating would help to reduce these emissions.

Electricity and heat production through geothermal power plants are alternative forms of low-carbon, renewable energy production that are underutilized in Canada. Geothermal plants are capable of producing constant, on-demand electricity without the need for specific weather conditions, which is one of the main disadvantages of wind and solar electricity generation, or the environmental concerns associated with hydroelectric plants. Canada has many potential areas that provide the necessary conditions for the operation of geothermal plants (such as high heat flow values, porous and permeable

rock types, and pore fluids, etc.) making this form of energy production a potential candidate to produce low-carbon electricity (Grasby et al., 2012). For electricity generation, temperatures exceeding 150°C are required, however lower temperature geothermal systems can also be utilized to provide a direct source of heating for residential buildings rather than for electricity generation. Direct use applications would further reduce the reliance on fossil fuel and electrical heating methods.

1.2 Importance of Geothermal Energy for Northern Canadian Communities

Communities in Northern Canada would benefit greatly from using geothermal as a source of energy. Other forms of renewable energy production such as solar are not viable options for these communities as they get very little sunlight during the winter months, limiting the amount of energy that can be produced. Geothermal energy can also be utilized by these communities directly as a source of residential heating in addition to supplying electricity. Many of these communities currently rely on fossil fuel burning plants for electricity, not only would geothermal energy production help to reduce carbon emissions from energy production, it would also reduce the need for costly fuel shipments from the South.

The Canadian territory of Yukon, located in the north-western most part of Canada, has a population of approximately 44,000 people (Government of Yukon, 2022) living in a collection of 18 cities, towns, and smaller communities. These communities are isolated from the main electrical grid of Canada, and thus are reliant on their own sources of electricity and heat production and distribution. Of the 18 northern communities, 13 are connected through a small-scale electrical grid called the Yukon Integrated System (YIS), with electrical power mainly generated through hydroelectric power. Diesel and liquified natural gas (LNG) generators are also utilized to supplement the power generation of the YIS in times of peak demand such as during the winter months for heating. The remaining communities obtain their electricity from micro-grid plants powered by diesel generators (Government of Yukon, 2018), which are a source of significant carbon emissions. For this reason, alternative energy sources such as geothermal energy are being investigated for energy production for those communities not served by the YIS. Not only would geothermal energy provide independence for these communities from the need for fuel shipped from Southern Canada for electricity production, but it could also be directly utilized for district heating for homes. A direct use geothermal system could provide an alternative source of energy for space heating which would reduce the need for electricity or fossil fuels. Direct use geothermal can also

be utilized to heat greenhouses, allowing for the production of fresh produce year-round, further reducing the reliance of these communities on shipments from the south.

Much of the Yukon territory may be suitable for geothermal energy production. The main geological properties necessary for geothermal energy production are:

(1) A source of heat at a depth accessible by drilling
(2) Pore fluids capable of transporting the heat
(3) Sufficiently permeable rock types to allow the extraction of the hot fluids

Studies have shown that many parts of Yukon have high values of heat flow, which implies that there are elevated temperatures relatively close to the surface. This is likely the result of the thin crust, mapped via Curie point depth mapping (Majorowicz and Grasby, 2014; Witter et al., 2018). Borehole data indicates a high surface heat flow and subsurface temperatures exceeding 200°C at a depth of 6 km for much of the territory (Majorowicz and Grasby, 2014). This could provide a source of heat for geothermal energy production.

Of the five communities that are not connected to the YIS, Watson Lake has high potential for the development of geothermal energy. The area surrounding the community has a relatively high heat flow that could provide a heat source. In addition, the community is located in the vicinity of the Tintina Fault, a dextral strike-slip fault running North-West through most of the Yukon territory, which could provide a zone of permeable fractured rock containing pore fluids necessary for the extraction of geothermal energy. A geothermal electricity plant near Watson Lake would allow the community to have less reliance on fuel shipments as well as reduce carbon emissions from the existing diesel-powered generating plant. Geothermal energy could also be utilized as a form of district heating. Hot fluids could be pumped into buildings to provide a source of heat as an alternative to electric or gas-powered heating systems. In order to determine if a geothermal plant at Watson Lake would be feasible, geophysical exploration techniques such as magnetotellurics (MT) must be utilized to identify potential sources of pore fluid in hot, permeable rock near the community.

1.3 Geothermal Exploration

Hickson and Yehia (2014) outline the main steps for the development of a geothermal energy project. They define three main phases of development:

(1) **Target identification** uses a combination of disciplines including geology and geophysics to determine whether an area has potential for geothermal development by identifying areas that may have the necessary heat, fluids, and permeability. Some techniques utilized in this stage include identifying areas with permeable rock types and sufficient values of crustal heat flow by mapping geologic structure and heat flow. Locating potential structures of interest such as clay caps formed through hydrothermal clay alteration or previously unmapped faults through the use of geophysical techniques can also be used in this stage to identify potential areas with hot, permeable rocks. Geophysical techniques such as electromagnetic methods or gravity surveys can also be utilized here to locate regions containing pore fluids. Test wells are also drilled to determine the regional temperature gradient.

(2) **Prospect evaluation** utilizes in-depth testing and a range of survey types to assess the potential for a geothermal project. Subsurface structures are mapped in more detail, the composition of pore fluids and host rock types are determined, and more detailed geophysical surveys are undertaken. In this stage, reservoir evaluation is started, with analysis of existing wells in the area and the testing of host rock permeability. Shallow test wells are drilled to determine the local temperature gradient.

(3) **Project appraisal** determines whether a geothermal project is economically and physically feasible. This involves analysis of fractures as well as stress and strain in the area. Geochemical analysis of the pore fluids and host rocks continues, as well as more geophysical surveys. Test wells are drilled, and injection tests are performed. After this stage, a detailed analysis of all collected data is performed and if the project is proven to be feasible, development continues.

1.4 Geothermal Exploration at Watson Lake

The potential geothermal project at Watson Lake is still in the target identification stage of development. Heat flow modelling utilizing borehole data in Yukon has shown that the Watson Lake area has heat flow rates that may be sufficient for geothermal energy production (Majorowicz and Grasby, 2014). The high heat flow may be the result of thinned crust in the area. A study of Curie point depth mapping, which utilized aeromagnetic data to determine the thickness of the crust for parts of Yukon, found an average crustal thickness of approximately 20-30 km near Watson Lake, which is

thinner than the global average and would allow for greater heat flow to the surface (Witter et al., 2018). This could be due to the thin lithosphere in the area, which would indicate a shallow asthenosphere is responsible for the high temperature gradient. In addition, the elevation of Watson Lake is close to the global average. This combined with the lower-than-average crustal thicknesses could be the result of a hot, low density mantle below Watson Lake maintaining isostatic equilibrium. The thin crust might also be explained as a pull-apart basin formed by movement along the Tintina Fault zone. In order to better identify potential areas of interest for geothermal development near Watson Lake, smaller regional scale geophysical surveys must be undertaken.

In addition to these thermal studies, gravity data for the area has also been collected and analyzed. The results of the gravity survey suggest that the survey area contains a sedimentary basin extending from the surface to a depth of 500 m below sea level. This basin appears bounded on either side by fault strands, the locations of which are consistent with structures that are part of the Tintina Fault system (Witter, 2022). Sedimentary basins are an important target for geothermal development as they are composed of relatively porous, permeable rock types that enable the circulation of pore fluids. In addition, the rock types forming sedimentary basins are typically softer than crystalline igneous rocks, which is beneficial for reducing the cost of drilling wells. A detailed 3D MT survey in the same area as the gravity survey could indicate whether any pore fluids are present within the basin, which would allow for the further development of a geothermal project in the area.

Seismic reflection surveys and magnetic surveys may also be helpful in identifying areas of interest for geothermal energy development near Watson Lake. Seismic reflection techniques could be used to better image the fault zone, which would aid in the identification of geothermal targets. However, these types of surveys are relatively expensive and would be difficult to deploy in the Watson Lake area. Magnetic techniques could also be used to identify anomalies such as basalts in the basement rock which could provide an indication of past volcanic activity but would be limited in resolving near-surface features in the crust that would be of interest for geothermal development. Witter (2022) provides a discussion on aeromagnetic data collected in the area. The magnetic data show several strongly magnetic features interpreted to be volcanic in origin.

1.5 Magnetotelluric Methods for Geothermal Exploration

One of the first steps in geothermal exploration is the identification of potential resources in the study area. This is an interdisciplinary step involving studying the geology of the area, the geochemistry of the host rock and pore fluids, and utilizing geophysical techniques to better model the geologic structure (Hickson and Yehia, 2014). Magnetotellurics (MT) is a geophysical method that can be used in this stage of resource identification. This method involves determining the subsurface electrical resistivity of the Earth. Field measurements utilize instruments capable of measuring electric fields within the Earth that are induced by time variations of the Earth's magnetic field which is also measured. The equipment consists of induction coils oriented along three perpendicular axes (North, East, and vertically downward, into the Earth) which measure the magnetic source signals, and four electrodes place North, South, East, and West of the survey site, which measure the induced electric fields. MT data is collected at multiple sites which is processed and filtered, then inversion programs use the MT data to generate models of the subsurface electrical resistivity in the survey area. Converting magnetotelluric data into a resistivity model of the Earth is an inverse problem, which means that there will be multiple acceptable models that fit the measured MT data. To address this non-uniqueness, statistical methods are used along with prior geologic knowledge in order to select a final resistivity model. For geothermal energy exploration, the main target of interest is hot water located in the pores and fractures of permeable rock near the surface. This would have significantly lower electrical resistivity than the surrounding solid, dry rock. Thus, magnetotellurics can be used to locate such areas by identifying potential areas of low subsurface resistivity (Munoz, 2014).

1.6 Magnetotelluric Exploration at Watson Lake

A limited amount of MT data has been collected in the Watson Lake area, primarily as a part of the Lithoprobe Slave-Northern Cordillera Lithosphere Evolution (SNORCLE) transect (Ledo et al., 2002). However this MT data is insufficient for determining if the area is suitable for geothermal development. A more focused survey with a finer spaced grid of MT stations is required.

During July and August of 2021, a 3D magnetotelluric survey was conducted near the community of Watson Lake. The goal of this survey was to identify potential sources of geothermal energy along the Tintina fault and to better constrain the location of the Tintina Fault. This thesis documents the results of the MT data collection, processing, and inversion and serves to interpret the resulting inversion models in order to determine if there are any conducting bodies located within the vicinity of the survey

area that could potentially serve as sources of geothermal energy production. This work was completed in order to:

(1) Define near surface geology with regards to the development of geothermal energy

In order to be suitable for geothermal energy production, the geology of the survey area must contain relatively porous, permeable rock through which pore fluids can be circulated to extract heat. It is also necessary that there is sufficient heat present to provide pore fluids at the temperatures necessary for heating and electricity production. These geologic features can be identified via the MT method. Pore fluid within the host rock will lower the electrical resistivity of the host rock, making it easily identifiable in the MT inversion model. Alternatively, MT can also image clay caps formed through hydrothermal alteration of the host rock. These clay caps are formed of minerals such as smectite and illite and have significantly lower values of electrical resistivity than the surrounding rock and can often act as a seal for hot circulating fluids below, making them potential targets for geothermal exploration (Munoz, 2014). Smectite and illite form at temperatures between 100 – 300 °C, this fact allows the measurement of subsurface resistivity to also be used to determine subsurface temperatures in the areas where these minerals form (Ussher et al., 2000).

(2) Constrain the location of the Tintina Fault

An extension of the Northern Rocky Mountain Trench Fault, the Tintina Fault is a dextral strike-slip fault that runs through much of the Yukon territory. Previous studies of the fault suggest that it is oriented with a strike of between N45°W and N50°W (Ledo et al., 2002) and could be a potential source of fractured, permeable rock and fluids for a geothermal system at Watson Lake. However, the location of the fault in the vicinity of Watson Lake is poorly constrained due to glacial overburden and many geologic maps of the area offer conflicting information on the location of the fault. The bedrock geology map from the Yukon Geological Survey places the fault West of the community of Watson Lake, between the Liard River and the junction between the Alaska highway and Highway 37 (Yukon Geological Survey, 2022). Witter (2022) provided an analysis of gravity data collected in the Watson Lake area and suggested that the fault zone lies further West, closer the junction between the Alaska highway and Highway 37. An analysis of

the MT data collected in the area could help to better constrain the location of the fault, which is necessary to identify potential areas of fractured rock and fluid for geothermal production.

1.7 Chapter Overview

The remaining chapters of this thesis will outline the geology of the study area and provide a basic overview of geothermal development. Then the magnetotelluric method will be outlined and discussed, followed by a discussion of the MT data collection, processing, inversion, and finally the interpretation of the preferred resistivity model at Watson Lake. The structure of the thesis is given below.

Chapter 2 provides a brief overview of the geology of the Watson Lake area, as well as a review of the previous studies conducted in the area to determine the viability of geothermal energy production. Previous investigations of the location of the Tintina Fault are also described.

Chapter 3 provides a description of geothermal energy exploration and production including using geothermal energy for electricity production and direct heating. Enhanced Geothermal Systems (EGS) and closed loop systems are also discussed.

Chapter 4 discusses the theory of magnetotellurics and the application of magnetotellurics for geothermal exploration. It provides detailed derivations of important equations and formulae as well as an overview of data processing and inversion methods. It also expands the theory of magnetotellurics from a one-dimensional case to two and three dimensions. Other important properties including the tipper and phase tensor are also discussed.

In chapter 5, a summary of the Watson Lake magnetotelluric data collection and processing is given. This chapter also explains the time series processing in detail and looks at the results of the pseudosection plots of apparent resistivity, phase, and tipper for the survey area. Plots of the phase tensor and induction vector data is utilized to determine the dimensionality of the MT data and to estimate an average strike of the fault.

Chapter 6 describes the 3D data inversion process that was used to convert the Watson Lake MT data into models of true resistivity varying with depth. Select inversion results are shown for several different inversions including an impedance tensor-only inversion, a rotated data inversion, and an inversion utilizing the impedance tensor and tipper data. The results are displayed in numerous ways including vertical and horizontal cross-sections as well as plots of data fit. Some results of synthetic MT data inversions and resolution tests are also shown.

An interpretation of the inversion model results is given in Chapter 7. Here I discuss the location of conductive regions determined by the inversion and provide possible explanations for their structure and composition. I attempt to determine the most likely explanation of the low resistivity features (conductors) imaged. This is done in part by comparing the MT results with the results of a gravity survey conducted in the area in order to better constrain the possible explanations of the conducting bodies. The results of our inversions are also used in order to better constrain the location of the Tintina Fault in the study area.

The eighth and final chapter serves to briefly summarize the main points of the study and to provide commentary on potential future studies of geothermal development in the area.

Chapter 2: Previous Geology, Geophysical, and Geothermal Studies of Yukon

2.1 Geologic and tectonic overview

The Yukon territory is located in the North-western most part of Canada, bordering the Northwest Territories to the East, Alaska to the West, and British Columbia to the South. The territory is located in the Canadian Cordillera, a mountain belt located on the Western portion of Canada (Monger and Price, 2002). This mountain belt was formed along the passive margin of North America, which itself formed initially due to rifting caused by the break-up of the supercontinent Rodinia, approximately 750 Ma. The rifting resulted in the creation of an oceanic basin, the boundary of which would eventually form the Cordillera (Dickinson, 2004; Monger and Price, 2002). Subduction beneath the North American plate has resulted in the accretion of the terranes that compose the Cordillera. The terranes are typically bounded by faults and evidence suggests that the terranes formed far from each other and their present locations (Monger and Price, 2002). Fossil evidence suggests that the terranes are formed from exotic material that was transported to North America where tectonic processes resulted in the accretion of the material on the Western part of North America (Johnston, 2008). This terrane accretion due to subduction is responsible for the westward growth of North America over the last 390 million years. (Monger and Price, 2002).

The Cordillera previously experienced extensive strike-slip motion, likely due to the Northward motion of the ribbon continent which formed its western components (including the intermontane belt) during the Late Cretaceous (Johnston, 2008).

A possible explanation for current strain experienced in the Cordillera could be due to the ongoing collision of the Yakutat block with North America. The collision is thought to be the cause of seismicity within the Mackenzie and Richardson Mountain ranges, causing activity along the faults of the Cordillera, mainly the Denali fault, and to some extent the Tintina Fault (Mazzotti and Hyndman, 2002).

The tectonic setting of the Canadian Cordillera makes it favourable for the development of geothermal energy. The heat needed for geothermal energy production is supplied by the past subduction and accretion of terranes, while the various strike-slip faults within the Cordillera, such as the Denali and Tintina Faults, may provide a source of fractured, permeable rock which would facilitate the movement of hot pore fluids to the surface.

In the context of geothermal exploration, movement on a fault is required to maintain the permeability of the fractured rock and allow hot fluids to move upwards and form geothermal reservoirs near the

surface. A study by Finley et al., (2022) of hydrothermal systems in the Southern Canadian Cordillera describes the relation between fault activity and geothermal resources along faults. They found that geothermal springs are preferentially located along recently seismically active faults such as the Columbia River Fault, Purcell Trench Fault, and Southern Rocky Mountain Trench Fault. Thus, it is important to consider the rate of fault movement when locating areas of interest for geothermal development as active faults are more likely to provide the permeability needed for pore fluid circulation and heat transport to the surface. Long-term regional fault activity can be determined by mapping the offset of geological units, modelling earthquake activity, and utilizing GPS measurements, while short-term, local movement can be difficult to measure.

2.2 The Omineca Belt

As a result of the subduction and terrane accretion described above, the Canadian Cordillera can be separated into five distinct morphogeological belts running approximately parallel to each other in a north-west direction to south-east direction. From West to East, these belts are the Insular belt, the Coast belt, the Intermontane belt, the Omineca belt, and the Foreland belt (Monger and Price, 2002). The main study area of this thesis at Watson Lake is located within the Omineca belt.

Located in the centre of the Canadian Cordillera between the Intermontane and Foreland belts, the Omineca belt consists mainly of sedimentary and igneous type rocks ranging in age from Paleoproterozoic to Early Cenozoic (Monger and Price, 2002). The Omineca belt is identified by the higher metamorphic grade of the rocks compared with the those in the Intermontane and Foreland belts which border it on the West and East respectively (Monger, 1989). The main structural feature of the Omineca belt is the Tintina Fault, a right-lateral strike-slip fault with an offset of approximately 430 km and an estimated slip rate of 0.5 mm/yr (Gabrielse et al., 2006; Leonard et al., 2008). A detailed analysis of previous studies of the Tintina Fault is provided later in the chapter. The area surrounding the Tintina Fault and Watson Lake is primarily composed of rocks from four different terranes: The Cassiar terrane, Yukon-Tanana terrane, Slide Mountain terrane, and North America-basinal strata (Yukon Geological Survey, 2020; Colpron et al., 2005). A map of the geology of the region from Cook et al., (2004) is shown below in Figure 2.1.

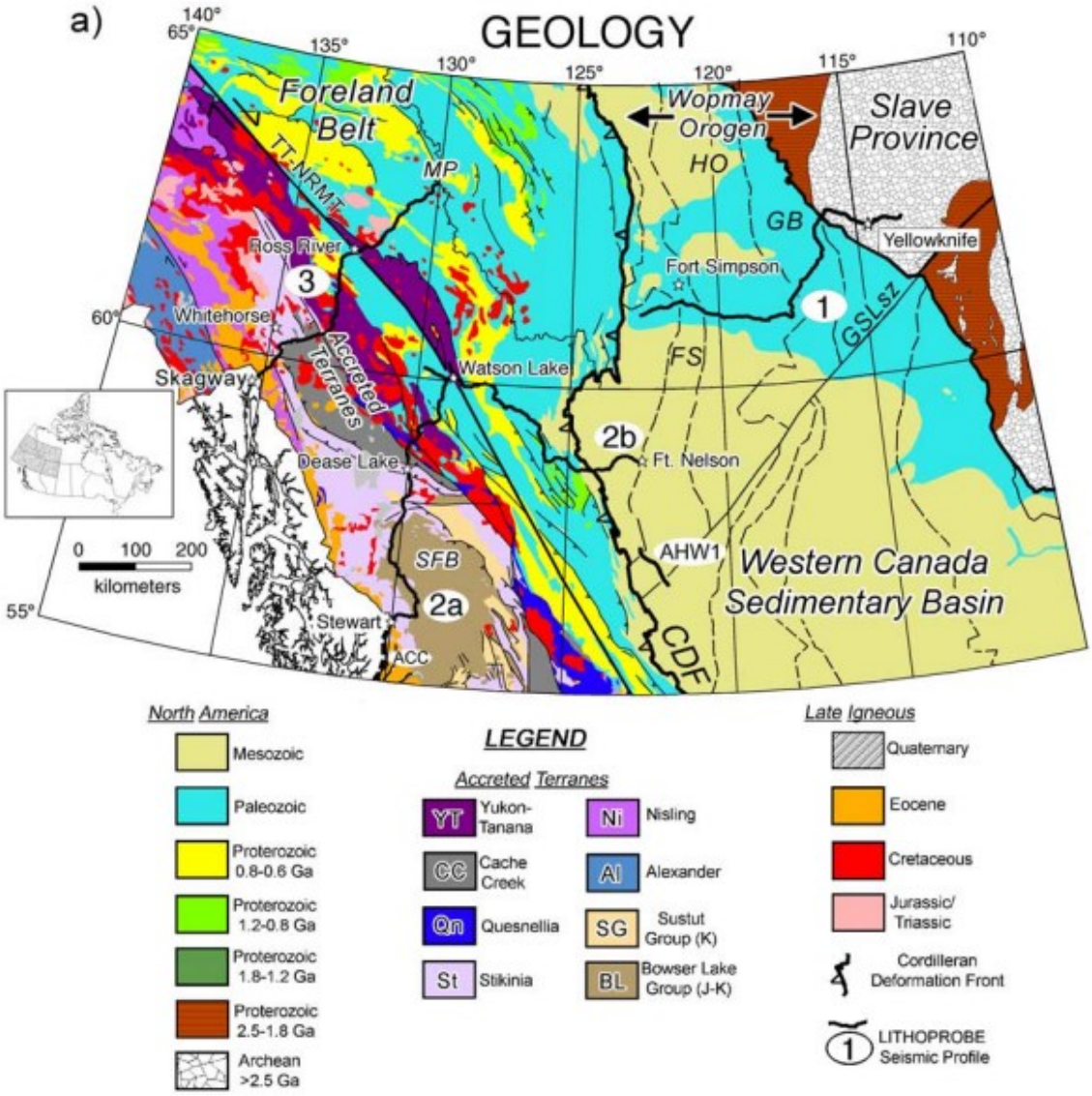

Figure 2.1: Map of the seismic lines crossing the Tintina Fault from the SNORCLE survey (From Cook et al., 2004, ©2004 by the American Geophysical Union).

2.2.1 Description of Terranes

The **Cassiar Terrane** is located mainly Southwest of the Tintina Fault and to the East of the Tintina Fault, separating the Slide Mountain terrane from the North America-basinal strata. It contains rocks of mainly Neoproterozoic to Triassic in age, consisting of carbonate, siliciclastic, and shale rock types (Yukon Geological Survey, 2020). It was shifted approximately 430 km Northwest by Eocene movement along the Tintina Fault (Gabrielse et al., 2006).

The **Yukon-Tanana Terrane** is located directly Northeast of the Tintina Fault. It consists mainly of metasedimentary rock from the Late Devonian to the Late Permian (Yukon Geological Survey, 2020), the Western portion of the Yukon-Tanana terrane was shifted approximately 430 km Northwest along the Tintina Fault during the Eocene (Gabrielse et al., 2006).

The **Slide Mountain Terrane** is placed Northeast of the Yukon-Tanana terrane in the study area. Its main rock types are igneous rocks ranging from mafic to ultra mafic in composition, along with cherts and argillite originating from the Late Devonian to the Early Permian (Yukon Geological Survey, 2020).

The **North America-Basinal Strata** is located in the Eastern-most portion of the study area and contains mainly Neoproterozoic to Triassic rocks consisting of shales, cherts, and other siliciclastic rocks (Yukon Geological Survey, 2020).

2.3 The Tintina Fault

The Tintina Fault is one of the main geologic features of the Canadian Cordillera. The tectonic history of the Canadian Cordillera has been dominated by subduction processes and terrane accretion, accompanied by strike-slip motion. The Baja British Columbia hypothesis suggests that the portion of the cordillera west of the Omineca belt had formed at southern latitudes near present-day Baja, California, and was transported northward during the Late Cretaceous (Umhoefer, 1987). This movement is believed to be responsible for the many dextral strike-slip faults that strike north-west within the Cordillera such as the Denali fault and Northern Rocky Mountain Trench Fault (Monger and Irving, 1980; Umhoefer, 1987). The Tintina Fault is also thought to have formed this way and is a Northern extension of the Rocky Mountain Trench Fault, which runs through the North-Western United States and British Columbia. The Tintina Fault is a right-lateral strike-slip fault located in the Northern section of the Canadian Cordillera. The fault is oriented with a Northwestern strike and displays between 430 and 490 km of horizontal displacement, most of which appears to have occurred during the Eocene (Gabrielse et al., 2006). The fault has a current estimated rate of movement of 0.5mm/yr (Leonard et al., 2008). In the study area near Watson Lake, the fault separates the Cassiar terrane Southwest of the fault and the Yukon-Tanana terrane, Northeast of the fault (Yukon Geological Survey, 2020).

The Tintina fault area has previously been studied as part of the Lithoprobe Slave-Northern Cordillera Lithosphere Evolution (SNORCLE) project (Ledo et al., 2002; Cook et al., 2004; Ledo et al., 2004). As part of the SNORCLE transect, magnetotelluric data were collected and inverted along several 2D profiles

crossing the fault (Ledo et al., 2002; Ledo et al., 2004). Three seismic lines crossing the fault were also collected (Cook et al., 2004).

Ledo et al., (2002), discuss the results of a study featuring 3 2D MT profiles crossing the Tintina Fault. One profile crosses the Southern section of the fault near Watson Lake, while the other two profiles cross further North (Figure 2.2). They used the 2D inversion algorithm developed by Rodi and Mackie (2001) to create resistivity models of the MT data. The results of their 2D inversions suggest that the Fault has an apparent strike between N45°W and N50°W, and they model several conducting bodies located in the Fault area (labeled A, B, and C in Figure 2.3) which are interpreted to be due to interconnected graphite films (Ledo et al., 2002). All 3 profiles also display a deep, near-vertical resistive structure that is interpreted to be a part of the deeper structure of the fault (Labeled D in Figure 2.3).

Another MT study of the Tintina Fault by Ledo et al., (2004) utilized a 2D MT profile crossing the Yukon territory in order to image the structure of the lithosphere below the Northern Cordillera. Their profile consisted of 42 MT stations oriented North-East from Northern British Columbia, through Yukon, and into the Northwest Territories. The results of their MT data inversions show the Tintina Fault as a highly resistive, near-vertical fault, which extends into the mantle, similar to the results of the previous study from Ledo et al., (2002).

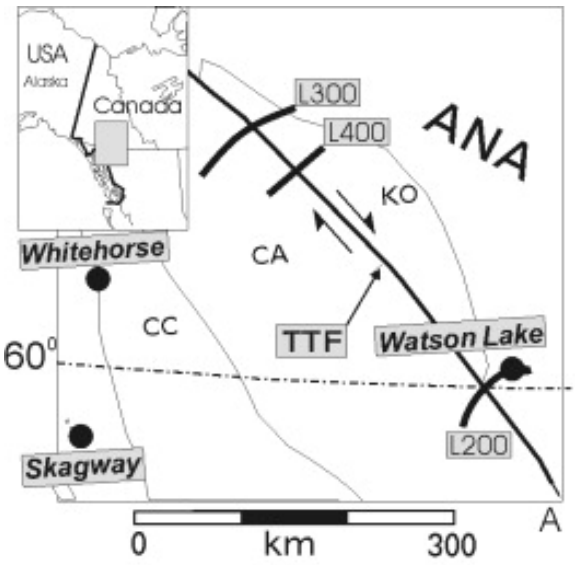

Figure 2.2: Map of Southwest Yukon, showing the location of the SNORCLE MT profiles crossing the Tintina Fault (From Ledo et al., 2002, ©2002 by the American Geophysical Union). ANA = Ancestral North America, CA = Cassiar Terrane, CC =Cache Creek Terrane, KO = Kootenay Terrane, TTF = Tintina Fault.

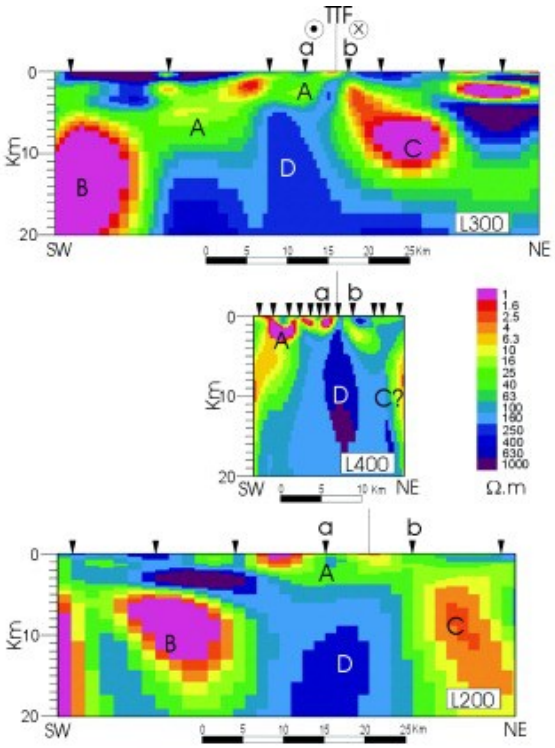

Figure 2.3: Results of the SNORCLE MT inversion models (From Ledo et al., 2002, ©2002 by the American Geophysical Union). TTF = Tintina Fault.

MT studies along other strike-slip faults provide insight into the relationship between fault activity and electrical resistivity structures along the fault. A zone of low resistivity was imaged by a 2D MT survey on the San Andreas Fault by Unsworth et al., (1997). The cause of the low resistivity was interpreted to be a mix of high salinity pore fluids within the heavily fractured damaged zone of the fault, and clay minerals. Other numerous MT studies along the San Andreas fault have shown that the active portions of the fault tend to have fault-zone conductors associated with fluid flow along the fault, while the tectonically locked portions of the fault tend to be more resistive due to the presence of solid, crystalline rock types and resistive basement rock (Unsworth et al., 1999; Bedrosian et al., 2002; Becken and Ritter, 2012). In addition to the Tintina Fault, the SNORCLE transect also consisted of an MT study across the Great Slave Lake Shear Zone (GSLsz). The results of this survey show that the inactive GSLsz contains a resistive structure along the fault (Wu et al., 2002). The GSLsz was also imaged using a 2D and 3D anisotropic inversions by Yin et al., (2014). This study also imaged a highly resistive structure along the fault. In both of these studies along the GSLsz, the resistive structure was interpreted to be a result of resistive mylonites that were metamorphosed to granulite facies. E. Wang et al., (2018) identified four conducting bodies along the GSLsz in their analysis of broadband MT data collected along the shear zone. The Kiskatinaw and Hottah conductors identified in their study were interpreted to be due to the presence of graphite and/or sulphide minerals. In addition to graphite and sulphides, saline pore fluids were also identified as potential cause of the other two conductors, The Ksituan-Chinchaga and Chinchaga-Buffalo Head conductors. Since the Tintina Fault is considered inactive with a slip rate of 0.5mm/yr (Leonard et al., 2008), the presence of highly resistive features along the fault trace is consistent with these previous studies and any potential conductors imaged may have similar explanations to the GSLsz conductors identified by E. Wang et al., (2018).

The SNORCLE transect also included three seismic reflection profiles crossing the Tintina Fault (Figure 2.1). In particular, lines 2a and 2b both cross the fault in the study area near Watson Lake (Cook et al., 2004). The seismic reflection results show an area west of Watson Lake that exhibits anomalously low reflectivity which is interpreted to be caused by the deformed and fractured rock within the near-vertical Tintina Fault zone. This area is wider near the surface with a horizontal extent of approximately 15 – 20km and extends to a depth of approximately 33 km. North of lines 2a and 2b, line 3 crosses the fault near the community of Ross River. The low reflectivity area of the fault zone is also apparent in this data (Figure 2.4).

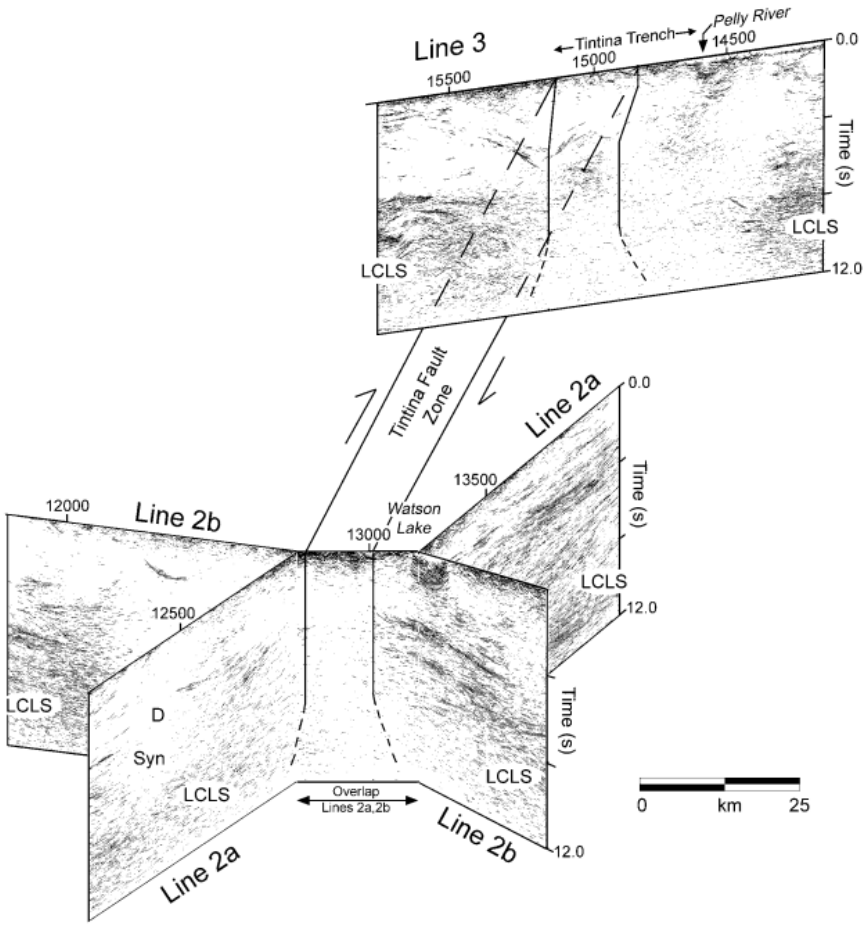

Figure 2.4: Results of the seismic profiles, displaying the zone of low reflectivity interpreted to be the Tintina Fault Zone (From Cook et al., 2004, ©2004 by the American Geophysical Union). LCLS = Lower Crustal Layered Sequence.

2.4 Conclusions

The geology of Yukon is defined by past tectonic processes including subduction, terrane accretion, and strike-slip motion. This has resulted in a complex and diverse regional geology for the territory. The formation of the Tintina Fault is a result of these processes, and the fractured rock of the fault zone could provide a source of permeable material to accommodate pore fluid flow, which would be beneficial for geothermal energy production. The development of geothermal resources requires a focus mainly on local geology in order to identify near-surface features of interest, thus it is necessary to better constrain the location of the Tintina Fault near Watson Lake and identify conductive zones along the fault that may indicate the presence of pore fluids. This is done using the magnetotelluric exploration method, the details of which are explored in later chapters.

Chapter 3: Geothermal Energy

3.1 Introduction to Geothermal Energy

Geothermal energy is a low-carbon, renewable energy source that can be utilized for both electricity and heat production. The source of energy in a geothermal system is heat produced by the Earth that is then transferred into pore fluid within the host rock. The main sources of heat are (1) radiogenic decay of isotopes such as Uranium, Thorium, and Potassium trapped within the host rock and (2) residual heat from the formation of the Earth. Heat is often transferred through advection of magma or other fluids.

Most of the Earth's subsurface has very high temperatures, but the majority of the heat is inaccessible for energy production. In order to utilize this heat, near-surface heat sources must be located. These could be in the form of rock types with higher concentrations of radioactive isotopes or in areas near active tectonic regimes such as near volcanoes where molten rock accumulates heating up the surrounding region. To extract the heat necessary for energy production, the rocks must also contain pore fluid which circulates within the rock, gathering heat. The rock must also be permeable enough such that the pore fluid can easily circulate and be extracted. Depending on the temperature of the pore fluid the heat can either be used directly for heating or for electricity generation. For electricity production, temperatures exceeding 150°C are typically needed.

If the pore fluid is mainly composed of steam, it can be used to directly power turbines, producing electricity. Lower temperature reservoirs containing mainly water can be utilized in binary cycle generators, which are based on the organic Rankine cycle, where hot water is used to boil a liquid with lower boiling point than water, such as ammonia, to produce steam to power the turbine. If the temperature of the fluid is insufficient for electricity production it can be used directly for heating in residential buildings or green houses (Barbier, 2002). For areas where high heat flow is present, but no fluids are available, an Enhanced Geothermal System (EGS) may be developed. In these systems, the host rock is fractured with high pressure fluids in order to enhance the permeability of the rock. Fluids can then be injected into the host rock in order to extract the heat (Olasolo et al., 2016). Alternatively, a closed-loop system where fluid is injected and circulated through wells but kept separate from the host rock are possible as well, eliminating the need for pre-existing fluids and permeable rock types (Van Horn et al., 2020).

Geothermal energy is currently being utilized in many countries with abundant sources of near surface heat. The largest producers of electricity with geothermal energy are currently the United States, Indonesia, Philippines, and Turkey (Richter, 2022). These systems can be developed in volcanically active

areas, such as the Geysers geothermal field in California, USA and the Hellisheidi power station in Iceland. They can also be developed along strike-slip fault zones, where fractured rock within the fault zone allows for fluid circulation. Examples of fault-based geothermal systems include the numerous projects in the basin and range province of the United States. Studies have shown that parts of Canada may also have the necessary conditions required for geothermal energy production (Figure 3.1), although there is currently no grid-scale electricity production (Grasby et al., 2012).

One of the main limitations of geothermal systems is the cost of drilling wells, therefore it is imperative to identify potential near-surface sources of heat and fluid to reduce the associated cost of drilling. In addition, the host rock must have sufficient permeability to allow for the extraction of the pore fluid. It is therefore necessary to utilize geological and geophysical analysis of potential areas of development in order to determine the feasibility of a geothermal project.

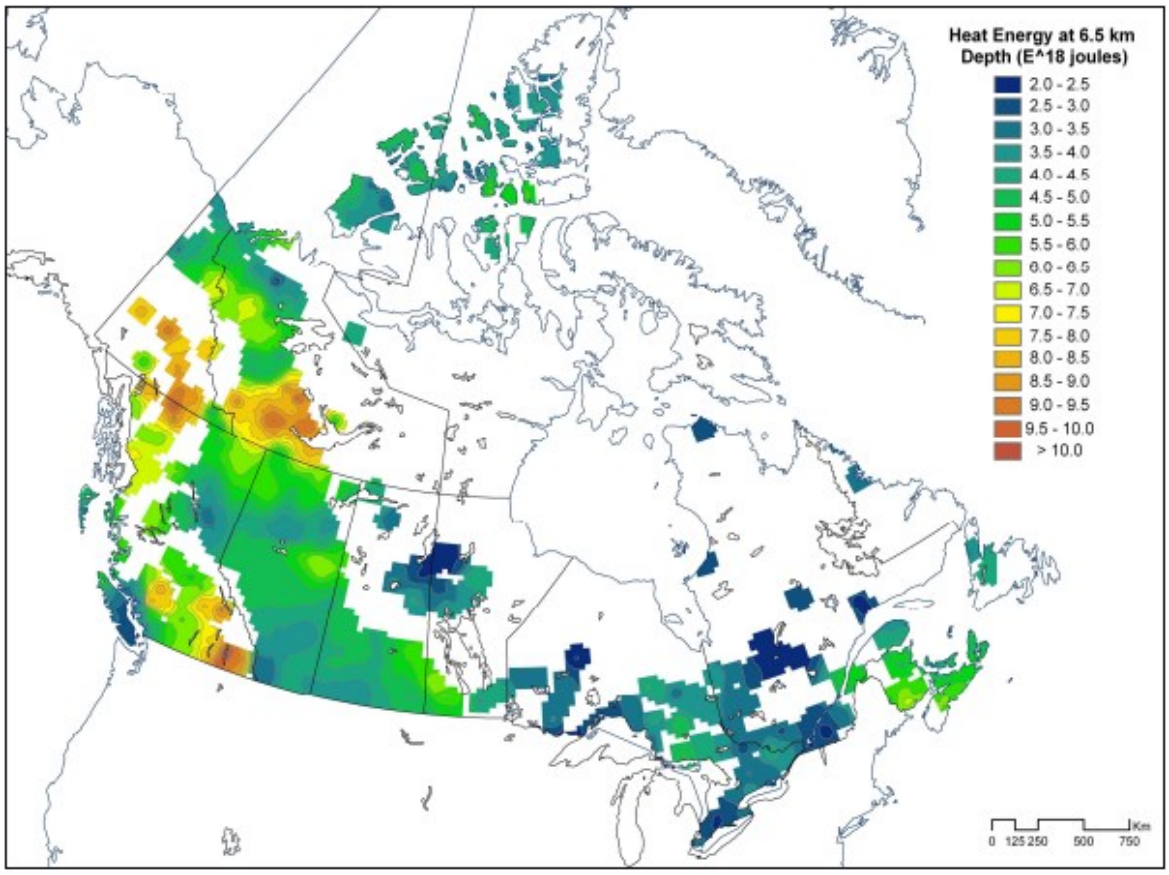

Figure 3.1: Map showing the in-place available geothermal energy for Canada at a depth of 6.5 km. White areas indicate regions where no data are available. (From Grasby et al., 2012, © Her Majesty the Queen in Right of Canada 2012. Licenced under the Open Government Licence – Canada https://open.canada.ca/en/open-government-licence-canada).

3.2 Geothermal Exploration

Geothermal exploration can be split into three main phases following the scheme of Hickson and Yehia (2014):

(1) Target Identification
(2) Prospect Evaluation
(3) Project Appraisal

Geophysics is an important component in all three phases in order to help identify the location and extent of potential geothermal resources. Some common geophysical methods utilized for geothermal exploration include gravity surveys, seismic surveys, and electromagnetic (EM) methods. Magnetotellurics (MT) is an electromagnetic method that is widely used for geothermal exploration. The depth of investigation of the MT method is greater than other EM methods, reaching depths greater than 1 km below the Earth's surface. This makes it ideal for locating areas of low electrical resistivity which may indicate the presence of a geothermal reservoir or areas of hydrothermal clay alteration (Pellerin et al., 1996; Ussher et al., 2000).

The main goal of geothermal exploration is to identify areas that have sufficiently high heat flow values for energy production and the necessary permeable rock types containing hot pore fluids. Areas with high heat flow are identified first in regional studies, then focused geological, geochemical, and geophysical studies are undertaken to determine if the area meets the requirements for further development.

Geothermal energy production also faces many challenges to development. The main challenge is associated with the cost of drilling wells. This can be one of the most expensive aspects of development and there is no guarantee that a drilled well will encounter an economically usable resource. Careful consideration of the collected data from the Target Identification and Prospect Evaluation stages must be used to select the best drill sites. Another limitation on the development of geothermal energy is the proper management of geothermal reservoirs. Monitoring must be done to ensure that heat and fluids are not extracted from the reservoir faster than they are replenished so that energy production can continue well into the future. Government legislation also has an effect on the development of geothermal systems, mainly concerning the ownership and control of the pore space needed. These are important concepts that need to also be considered before further development continues.

3.3 Geothermal Energy Production

Barbier (2002) provides an overview of geothermal energy production, the main points of which are summarized below.

In order to efficiently utilize geothermal energy, three main components of the subsurface are necessary.

(1) Heat must be available near the surface of the Earth in the area below the geothermal plant. This can be supplied via radiogenic heat of radioactive isotopes such as Uranium, Thorium, or Potassium present in the host rock, or via conduction from nearby magma sources if the geothermal plant is in a volcanically active area.
(2) There must also be some form of pore fluid present within the rock that will be heated by the heat source to suitable temperatures for electricity production. The fluid must also be located near the surface in order to allow for easier and more cost-effective extraction.
(3) Finally, the host rock must be porous and permeable enough such that pore fluids can circulate within the rock to effectively absorb the heat and be easily extracted. This can be achieved via primary porosity within the rock, or secondary porosity such as fractures from faulting. This can also be improved by inducing fractures within the rock such as in an engineered geothermal system discussed in more detail in Section 3.4.

Pore fluid within a geothermal system is typically liquid water or steam. Systems containing mostly water are referred to as “Water dominated”, and are further classified as either “Hot water fields” where the system contains almost entirely water at temperatures up to 100 °C, or “Wet steam fields” where the reservoir contains a mixture of mostly pressurized water and some steam exceeding temperatures of 100 °C. According to Barbier (2002), wet steam fields make up the majority of geothermal reservoirs exploited for energy production. If a reservoir contains mainly steam as the pore fluid, it is identified as a “Vapour dominated field”.

Geothermal systems can be classified into two main categories depending on how the energy resource is utilized: direct use or electricity production.

For direct use systems, the fluids are extracted and used for direct heating via a heat exchanger. The cooled fluids are then recirculated into the reservoir. This heating can be in the form of space heating for residential buildings, greenhouses, bathing, and other industrial processes such as pulp and paper

processing, milk pasteurization, fish farming, and curing concrete (Barbier, 2002; Fridleifsson, 2001; Lund et al., 2005).

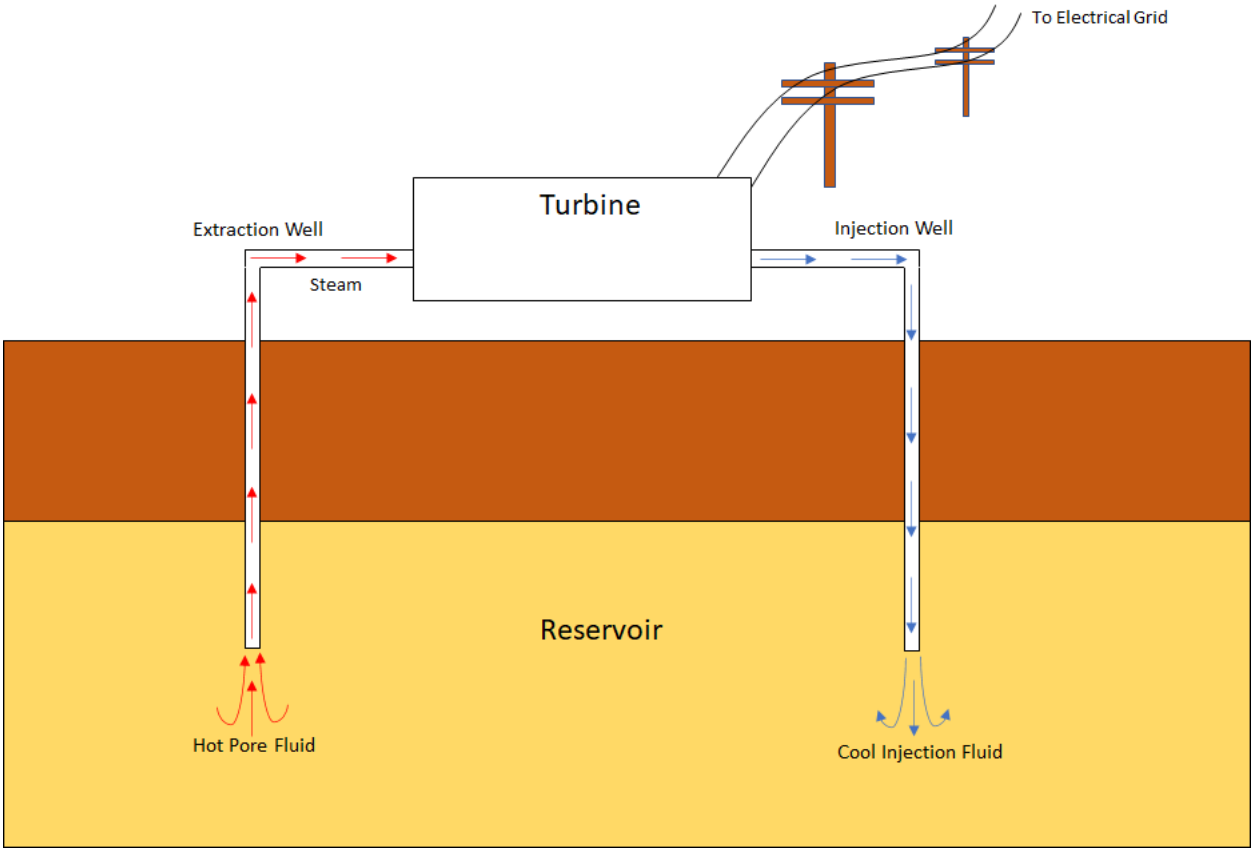

Figure 3.2: Schematic of a typical geothermal power plant. Hot pore fluid is extracted and used to create steam to power a turbine to produce electricity. The cooled fluid is then reinjected back into the reservoir.

In the case of electricity generation, the fluid is extracted and used to produce steam, either directly or by heating some other fluid via a heat exchanger in what is known as a "binary cycle plant". One advantage to using a second fluid for the steam production is that fluids with lower boiling points than water, such as ammonia, can be used which allows for electricity production from geothermal sources with lower temperatures. The steam is then used to rotate turbines to generate the electricity and the cooled fluid is then condensed and either returned to the host rock to circulate through the rock, absorbing heat until it is extracted again or, in the case of a binary cycle plant, condensed and reused (Barbier, 2002). Typical geothermal systems require the use of 2 or more wells to be used for extraction and injection of the pore fluid (Figure 3.2).

3.4 Engineered Geothermal Systems

One of the main necessities for the development of conventional geothermal resources is the presence of fluids within a permeable host rock that will allow the pore fluid to circulate. For areas with a high temperatures, but no fluids or permeability, it is still possible to extract heat. This requires the development of an Engineered Geothermal System (EGS), also called Enhanced Geothermal Systems or Hot Dry Rock Projects (Duchane and Brown, 2002). This process requires the creation of permeability and injection of fluids in a process is similar to hydraulic fracturing used in oil and gas exploration, in which a fluid is injected into the host rock in order to create more fractures within the rock, thus allowing for a more efficient way of extracting the resource. In the case of EGS, the resource extracted is the heat from the rock, rather than oil or natural gas typically extracted through hydraulic fracturing. EGS can be used in areas without high permeability to allow for the extraction of heat that would otherwise be inaccessible (Olasolo et al., 2016).

A report from Tester et al., (2006) details the advantages of EGS in the United States and challenges that it may experience. The report estimates that the total energy available for extraction in the United States via EGS is approximately 2000 times the country's annual energy consumption. However, to reliable extract deeper resources below 3 – 5 km depth, new advancements in drilling technologies (specifically aimed at lowering drilling costs) need to be undertaken. EGS can also be described as a form of "heat mining" since without careful monitoring of fluid extraction, heat can be extracted from the rock faster than it is able to be recharged, cooling the rock and reducing the amount of usable energy. Another disadvantage is the fluid lost within the rock during circulation. This requires constant injection of new pore fluids which can be problematic in areas with unreliable water supplies.

One advantage of EGS is that it could also be utilized as a way of storing Carbon dioxide (CO_2) within the subsurface. Studies (Brown, 2000; Tester et al., 2006; C. Wang et al., 2018) have been undertaken that show the potential of using CO_2 as a working fluid for geothermal systems instead of water-based fluids. This method would have several advantages over water-based systems. First, CO_2 has thermal properties that make it more effective at capturing heat than water. This would allow for more efficient heat extraction in lower temperature reservoirs. CO_2 would also prevent the build-up of scale within the porosity of the rock. This limitation in water-based systems is caused by dissolved compounds precipitating on the pore surface, effectively reducing porosity and permeability within the reservoir. Since the CO_2 fluid cannot contain dissolved compounds like water can, this would no longer be a limitation. The final advantage would be the eventual sequestration of the CO_2 within the host rock.

Since some pore fluid is typically lost over time within the host rock in a geothermal system, using CO_2 as the working fluid would allow the geothermal system to provide the dual purpose of generating electricity and capturing CO_2 within the subsurface.

Like hydraulic fracturing, EGS has caused concerns over induced seismicity created from injecting fluids into the Earth. This induced seismicity could cause large scale earthquakes and damage to nearby urban areas. One example of this is the now suspended EGS project in Basel, Switzerland, where injection of fluids initiated several earthquakes causing damage to homes and infrastructure within the city, totalling to over $7 million dollars in damages (Kraft et al., 2009). Another example of EGS induced seismicity occurred in 2017 at the Pohang EGS project in South Korea where fluid injection activated a previously unknown fault in the area, inducing a M_w 5.5 Earthquake which caused damages totalling over $75 million, many hospitalizations, and one death (Ellsworth et al., 2019). It is clear from these incidents that seismic activity near EGS projects must be closely monitored to help prevent future incidents from occurring.

3.5 Closed-loop Geothermal Systems

An alternative to traditional geothermal and enhanced geothermal systems, closed-loop systems offer many advantages for energy production (Van Horn et al., 2020). Closed- loop systems require only high near-surface thermal gradients to function as the fluid is supplied and contained separately from the host rock. For these systems, the extraction and injection wells are cased and connected to form a loop of pipe that allows fluids to circulate without coming in direct contact with the host rock. An advantage of this is that porous, permeable rock types, and pore fluid within the host rock are not required for operation and no fluids are lost during operation. In addition, these systems can use fluids other than water with better thermal properties in order to more effectively extract heat for electricity generation.

Closed-loop systems can have a variety of configurations such as a “u-loop” system consisting of two or more vertical wells connected by horizontal segments, or a coaxial system with the injection and extraction wells situated concentrically within the same vertical well. A disadvantage of this is that some forms of closed-loop systems require horizontal drilling to connect the extraction and injection wells, thus the cost of production is typically significantly higher than conventional geothermal systems. This generally limits their use to areas with shallow thermal resources. The Canadian based company

Eavor Technologies is currently developing closed-loop geothermal systems with successful testing sites in Alberta (Eavor Technologies Inc., 2023a) and in New Mexico (Eavor Technologies Inc., 2023b).

3.6 Motivation for Geothermal Energy Development in Yukon

The electrical grid of Yukon is not connected to the main electrical grid of the rest of Canada. Most communities in Yukon are connected by a small-scale grid known as the Yukon Integrated System (YIS) which is mainly supplied power through the use of hydroelectric dams located near the city of Whitehorse and is also supplemented with diesel powered generating stations during times of peak electricity demand. While the YIS services most of the communities of Yukon, many smaller communities in the territory are not directly connected to the YIS and must rely on their own electrical generation, typically in the form of diesel or natural gas-powered generators (Government of Yukon, 2018). Other alternative forms of energy such as wind and solar are not considered suitable candidates due to a lack of reliable energy sources. For example, during the winter months Yukon receives very little sunlight due to the territory's northern location, meaning that solar energy would be unable to provide the energy needs during these times. Recent studies (Majorowicz and Grasby, 2014, Witter et al., 2018) have shown that many communities in the Yukon territory have the potential to generate electricity via geothermal powerplants due to the area having high surface heat flow values, likely a result of crustal thinning in the area due to a thin asthenosphere and hot, low density mantle below. If suitable amounts of fractured rock and pore fluid are present in the vicinity of these northern communities, then geothermal energy production could be a viable alternative to fossil fuels for electricity generation. The territory also contains many major faults such as the Tintina Fault which runs through most of the territory and could provide a source of fractured, permeable rock capable of hosting the necessary pore fluid. In particular, the community of Watson Lake lies directly East of the Tintina Fault and is not currently serviced by the YIS, making it an ideal candidate for potential geothermal energy production. This could be in the form of electricity generation for local use or directly for residential heating.

3.7 Geothermal Potential of Yukon

There are many conditions that need to be satisfied for geothermal energy production to be considered physically possible and economically feasible for an area. Conventional geothermal systems require

near-surface heat, circulating pore fluid to extract the heat, and rock with sufficient permeability for fluid extraction. It is necessary to determine whether or not these conditions are met for the study area before further geothermal development can occur.

3.7.1 Subsurface Temperatures

Many studies have recently been undertaken to determine whether it is both physically possible and economically feasible to install and operate geothermal plants in Yukon. Determining the subsurface temperature of the study area is a crucial first step.

A 2018 study from Witter et al., used Curie point depth mapping in order to measure the crustal thickness of Yukon. Areas with thinner crust might be possible candidates for geothermal systems since a thin crust is often associated with a higher crustal heat flow. They used public domain magnetic survey data that had been collected for Yukon and found that there was an average crustal depth of between 20 and 30 km, with an average basal temperature of 900°C and a geothermal gradient of between 25 and 27°C/km. This lower-than-average crustal thickness may be the result of movement along the Tintina Fault creating a pull-apart basin in the area.

Majorowicz and Grasby (2014) have also published a report looking at the economic feasibility of geothermal energy production in Yukon. Using publicly available temperature data collected from boreholes across Northern Canada, they determine that there is a high geothermal potential for much of the Yukon. In particular, they modelled the temperature in the Watson Lake area to vary between approximately 80-90 °C at a depth of 2 km and approximately 200-240°C at a depth of 6 km with a heat flow of approximately 100-110 mW/m^2. Using these values, along with an assumed fluid flow rate of 30 l/s, Majorowicz and Grasby (2014) suggest that geothermal energy production would be “economically competitive” with diesel and natural gas energy production.

3.7.2 Rock Permeability and Pore Fluids

Fault zones are a potential source of the permeable rock necessary for geothermal development and may also contain circulating pore fluid within the permeable fractures. Extensional stress in the vicinity of the fault zone causes fractures to form, increasing the porosity and permeability of the rock, thereby allowing pore fluid to concentrate and circulate within the rocks of the fault zone. For the area near Watson Lake, the Tintina Fault zone may provide a source of this fractured, permeable rock. Due to

glacial till coverage, the exact location of the fault is poorly constrained and more detailed geophysical surveys such as MT and gravity will need to be utilized to better locate the fault and determine whether the necessary fractured rock is present, and whether it contains circulating pore fluids.

3.8 Conclusions

Geothermal energy is a form of alternative energy that is being investigated as a potential source of heating and electricity for northern communities in Canada. Much of Yukon has been shown to have sufficiently high heat flow to make geothermal energy production feasible, but this also requires a source of pore fluids and a source of permeable rock through which the pore fluids can circulate. The community of Watson Lake lies close to the strike-slip Tintina Fault which could potentially provide the necessary permeable rock through the form of fractures within the rock along the fault zone. If pore fluid is present within these fractures and is at a suitable temperature for heating or electricity production, then a geothermal power plant may be feasible as an alternative to diesel for the community's power generation. Further studies need to be undertaken to determine whether pore fluid is present within the rock, including the collection and analysis of gravity and magnetotelluric data. A full analysis of the gravity survey can be found in Witter (2022), the remainder of this thesis will detail the collection and analysis of the magnetotelluric data.

Chapter 4: The Magnetotelluric Method

4.1 Introduction

The Magnetotelluric (MT) method is a geophysical method for measuring the resistivity of the Earth. The method was first proposed by Tikhonov (1950) and Cagniard (1953) and utilizes naturally occurring electromagnetic (EM) signals that travel through the atmosphere into the Earth to determine variations in subsurface electrical resistivity. In this chapter, a brief introduction to the MT method is given. A more in-depth explanation can be found in Simpson and Bahr (2005), which details the main concepts of the magnetotelluric method.

As the EM signals travel through the Earth (Figure 4.1), they attenuate according to the skin depth equation (derived below in section 4.2.4) and thus low frequency signals will propagate deeper in the Earth than high frequency signals. This property of the EM signals allows for depth variations of resistivity to be measured. MT measures electric and magnetic fields that are used to compute an apparent resistivity. The measured apparent resistivity can be thought of as a weighted average of the resistivity of the subsurface. It is therefore necessary to use the measured apparent resistivity data to create inversion models of how true resistivity varies spatially within the subsurface.

The basic workflow for the MT method is shown in Figure 4.2 below. Raw time series MT data must first be collected using specialized equipment to measure the EM signals. The time series data is then transformed to obtain measurements of the impedance in the frequency domain. This data can then be used to calculate the apparent resistivity of the Earth.

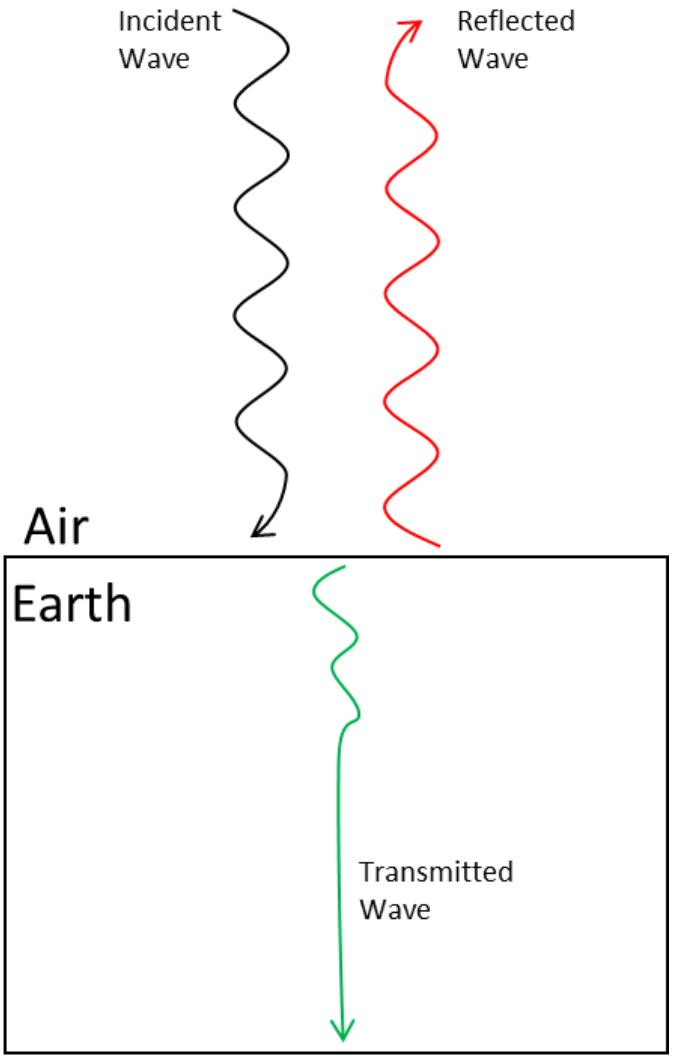

Figure 4.1: Diagram showing the propagation of MT signals in the Earth. The incident wave is partially reflected off the Air-Earth boundary, and partially transmitted through. The transmitted wave attenuates as it travels downward (Modified from Unsworth, 2019a)

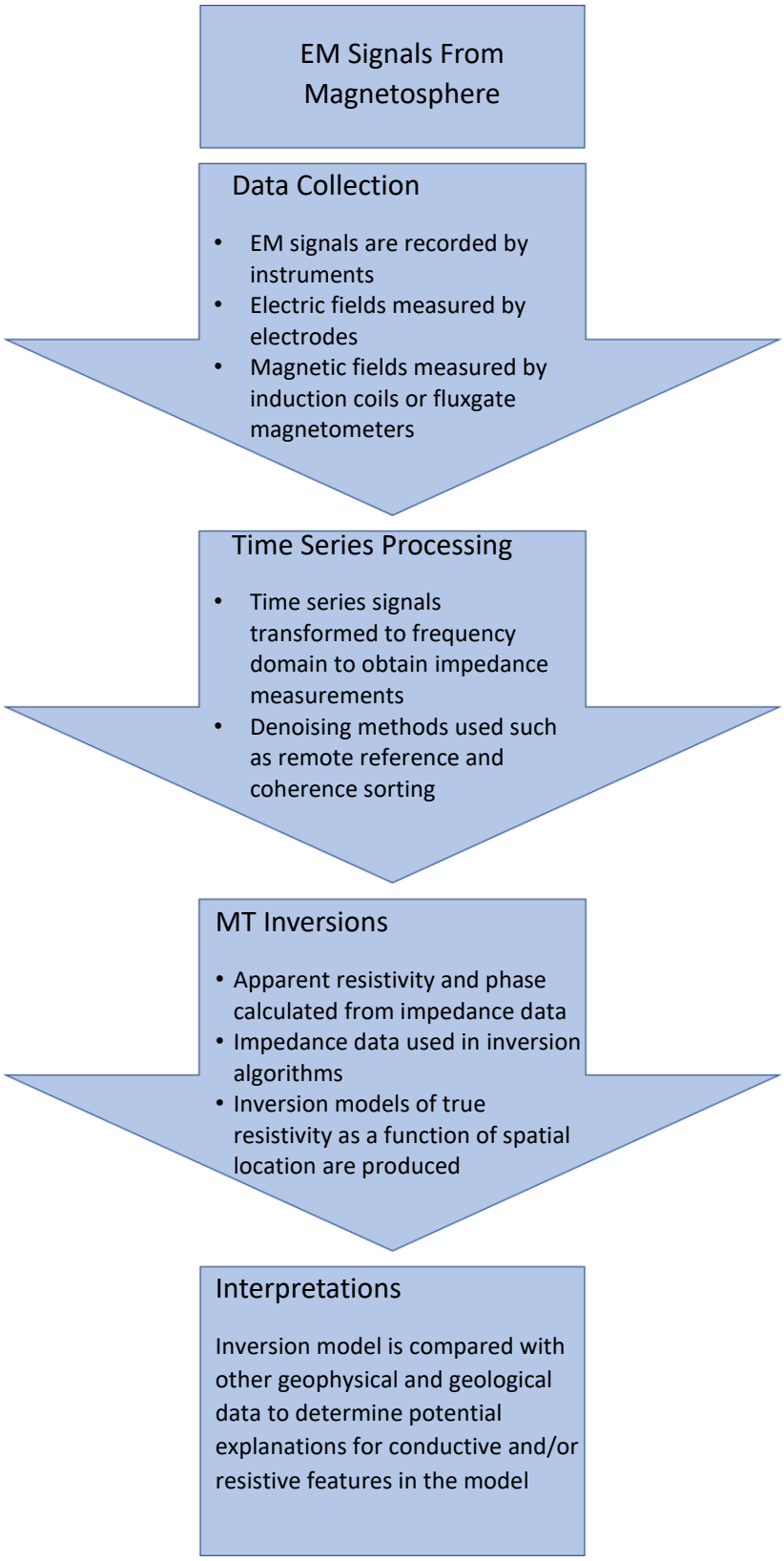

Figure 4.2: Workflow for magnetotelluric data collection, processing, and inversion.

4.2 Mathematical Basis: Responses of an Earth With a 1D, 2D, and 3D Resistivity Structure

Detailed derivations of the equations governing the magnetotelluric method can be found in Chapter 2 of Simpson and Bahr (2005) and Unsworth (2019a and 2019b). They are summarized in the sections below.

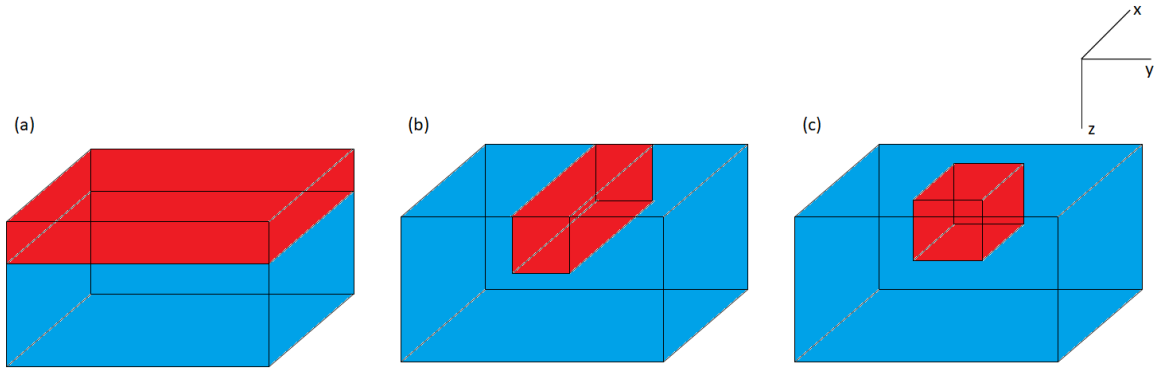

Figure 4.3: Examples of 3-D resistivity structures where the variations occur in (a) 1D, (b) 2D, and (c) 3D. Red and blue regions have different values of electrical resistivity.

4.2.1 Magnetotelluric Response of a 1D Resistivity Structure

For a 1D resistivity model of the Earth (Figure 4.3 (a)), the electrical resistivity will only vary in one direction (i.e. with depth), while the resistivity remains constant horizontally. This is the simplest form of resistivity model and is governed by a single equation for the impedance of the Earth, as well as the skin depth equation, both derived below.

The main equations governing MT can be derived starting from Maxwell's equations:

$$\nabla \cdot \boldsymbol{E} = \frac{Q}{\epsilon_0} \qquad (4.1)$$

$$\nabla \cdot \boldsymbol{B} = 0 \qquad (4.2)$$

$$\nabla \times \boldsymbol{E} = -\frac{\partial \boldsymbol{B}}{\partial t} \qquad (4.3)$$

$$\nabla \times \boldsymbol{B} = \mu_0 \boldsymbol{J} + \mu_0 \epsilon_0 \frac{\partial \boldsymbol{E}}{\partial t} \qquad (4.4)$$

where $\boldsymbol{E}$ is the electric field vector (V/m), Q is the charge density (C/m^3), ε_0 is the permittivity of free space, $\boldsymbol{B}$ is the magnetic flux density (T), t is time (s), μ_0 is the magnetic permeability of free space, and $\boldsymbol{J}$ is the current density (A/m^2).

By taking the curl of (4.3), equation (4.4) can be combined with (4.3) to form the equation:

$$\nabla(\nabla \cdot \boldsymbol{E}) - \nabla^2 \boldsymbol{E} = -\frac{\partial}{\partial t}(\mu_0 \boldsymbol{J} + \mu_0 \epsilon_0 \frac{\partial \boldsymbol{E}}{\partial t}) \qquad (4.5)$$

Then substituting

$$\boldsymbol{J} = \sigma \boldsymbol{E} \qquad (4.6)$$

where σ is the electrical conductivity of the medium (S/m), and assuming that there are no free electric charges present (i.e. $\nabla \cdot \boldsymbol{E} = 0$), the following second-order partial differential equation can be obtained:

$$\nabla^2 \boldsymbol{E} = \mu_0 \sigma \frac{\partial \boldsymbol{E}}{\partial t} + \mu_0 \epsilon_0 \frac{\partial^2 \boldsymbol{E}}{\partial t^2} \qquad (4.7)$$

The right-hand side of this equation can then be separated into two parts. The conduction current component, which propagates via the movement of charged particles (electrons):

$$\mu_0 \sigma \frac{\partial \boldsymbol{E}}{\partial t} \qquad (4.7a)$$

and the displacement current component, which relies on the rate of change of the electric field with respect to time for propagation:

$$\mu_0 \epsilon_0 \frac{\partial^2 \boldsymbol{E}}{\partial t^2} \qquad (4.7b)$$

To solve (4.7), it is assumed that the time variation of the electric and magnetic field components is harmonic. A solution can be found of the form:

$$\boldsymbol{E}(x, y, z, t) = \boldsymbol{A}(x, y, z) e^{-i\omega t} \qquad (4.8)$$

where $\boldsymbol{A}$ is some function of x, y, and z, and ω is the angular frequency, $2\pi f$. Substituting this value into equation (4.7), it can be shown that:

$$\nabla^2 \boldsymbol{A} = -i\omega\mu_0\sigma\boldsymbol{A} + \omega^2 \mu_0 \epsilon \boldsymbol{A} \qquad (4.9)$$

where the term:

$-i\omega\mu_0\sigma\boldsymbol{A}$ (4.9a)

represents the contribution from the conduction current and:

$\omega^2\mu_0\epsilon_0\boldsymbol{A}$ (4.9b)

represents the contribution from the displacement current. Taking the ratio between (4.9a) and (4.9b) and assuming typical values used in MT for ω and σ such as 10 Hz, 0.01 S/m respectively, it can be shown that the displacement current term is much smaller than the conduction current term, since MT primarily deals with EM signals diffusing in the Earth. Thus, the displacement current can be neglected from (4.9), which can then be simplified to:

$\nabla^2\boldsymbol{A} = -i\omega\mu_0\sigma\boldsymbol{A}$ (4.10)

Next, it is assumed that the wave is polarized in the x-direction, and that it is planar and travelling downward, in the z-direction. Thus:

$$\boldsymbol{A} = \begin{pmatrix} E_x \\ 0 \\ 0 \end{pmatrix} \quad (4.11)$$

and

$$\frac{\partial E_x}{\partial x} = \frac{\partial E_x}{\partial y} = 0 \quad (4.12)$$

Then (4.10) becomes:

$$\frac{\partial^2 E_x}{\partial z^2} = -i\omega\mu_0\sigma E_x \quad (4.13)$$

with solution:

$$E_x = E'e^{kz} \quad (4.14)$$

where E' is value of the electric field at the surface ($E_x(z=0)$), and k has a value of

$$k = \sqrt{-i\omega\mu_0\sigma} = \pm(1-i)\sqrt{\frac{\omega\mu_0\sigma}{2}} \quad (4.15)$$

If it is assumed that E_x must remain bounded as the depth approaches infinity, then only the negative solution for k is valid and the solution becomes:

$$E_x(z) = E'e^{-(1-i)\sqrt{\frac{\omega\mu_0\sigma}{2}}z} \quad (4.16)$$

This can then be inserted into equation (4.10) to obtain:

$$E_x(z,t) = E'e^{-(1-i)\sqrt{\frac{\omega\mu_0\sigma}{2}}z}e^{-i\omega t} \qquad (4.17)$$

This equation governs how the electric field component propagates through the Earth with increasing depth. It shows a dependence on both the electrical conductivity of the Earth (the inverse of electrical resistivity) and the frequency of the EM signal. From this equation, it can also be seen that the MT signals oscillate and attenuate as they travel deeper within the Earth. Using a similar method of derivation, an equation can also be found for the other horizontal electric field component E_y.

4.2.2 Impedance

The Impedance, Z, is the ratio between perpendicular electric and magnetic field components:

$$Z_{xy}(\omega) = \frac{E_x(\omega)}{H_y(\omega)} \qquad (4.18)$$

It can be used to determine the apparent resistivity of the Earth at a frequency, ω. Calculation of the impedance will remove information about the origin of the EM signals, but it allows for the determination of the Earth's resistivity structure. In order to calculate the impedance, the magnetic field component must be calculated. It can be shown, using Maxwell's equations, that the magnetic component is related to the respective perpendicular electric field component by:

$$H_y = \frac{1}{i\omega\mu_0}\frac{\partial E_x}{\partial z} \qquad (4.19)$$

Using a solution for E_x derived in section 4.2.1:

$$E_x = E'e^{-kz}e^{-i\omega t} \qquad (4.20)$$

where k and E' are defined as in (4.14) and (4.15), H_y then becomes:

$$H_y = \frac{1}{i\omega\mu_0}\frac{\partial}{\partial z}\left(A'e^{-kz}e^{-i\omega t}\right) = -\frac{k}{i\omega\mu_0}A'e^{-kz}e^{-iwt} \qquad (4.21)$$

Combining equations (4.18), (4.20), and (4.21) the Impedance can be written as:

$$Z_{xy}(\omega) = -\frac{i\omega\mu_0}{k} = -\frac{i\omega\mu_0}{\sqrt{-i\omega\mu_0\sigma}} = \frac{\sqrt{-i\omega\mu_0}}{\sigma} \qquad (4.22)$$

Taking the magnitude of Z_{xy}, it can be shown that:

$$\left|Z_{xy}(\omega)\right|^2 = \left|\frac{\sqrt{-i\omega\mu_0}}{\sigma}\right|^2 = \frac{\omega\mu_0}{\sigma} = \rho\omega\mu_0 \qquad (4.23)$$

where ρ is the apparent resistivity. Equation (4.23) can then be rearranged to obtain:

$$\rho(\omega) = \frac{\left|Z_{xy}(\omega)\right|^2}{\omega\mu_0} = \frac{1}{\omega\mu_0}\left|\frac{E_x(\omega)}{H_y(\omega)}\right|^2 \qquad (4.24)$$

This describes the apparent resistivity as a function of frequency, calculated using the measured perpendicular electric and magnetic components of the MT signal.

4.2.3 Phase

Another important component of MT data is the phase, which is the phase difference between the perpendicular electric and magnetic field components of the MT signal. Since E_x and H_y are complex values, they can be represented as:

$$E_x = |E_x|e^{i\phi_E} \qquad (4.25)$$

and

$$H_y = \left|H_y\right|e^{i\phi_H} \qquad (4.26)$$

where φ_E and φ_H are the phase angles of E_x and H_y respectively. Thus, the impedance can be written as:

$$Z_{xy} = \left|Z_{xy}\right|e^{i\phi_{xy}} = \left|Z_{xy}\right|e^{i(\phi_E - \phi_H)} \qquad (4.27)$$

where

$$\phi_{xy} = (\phi_E - \phi_H) = \tan^{-1}\left(\frac{Im(Z_{xy})}{Re(Z_{xy})}\right) \qquad (4.28)$$

The values $Im(Z_{xy})$ and $Re(Z_{xy})$ are the imaginary and real components of the impedance respectively. The phase angle φ_{xy} can be thought of as the phase difference between E_x and H_y.

4.2.4 Skin Depth

The skin depth, δ, describes the depth at which the EM signal has attenuated to 1/e (≈37%) of its original magnitude. It is used for estimating the depth of measured apparent resistivity values based on the

frequency of the signal. This value can be solved for by taking the modulus of (4.16) and solving for the depth (in meters) at which it has attenuated by 1/e:

$$|E_x| = |A|e^{-\sqrt{\frac{\omega\mu_0\sigma}{2}}z} \qquad (4.29)$$

$$\frac{|A|}{e} = |A|e^{-\sqrt{\frac{\omega\mu_0\sigma}{2}}\delta} \qquad (4.30)$$

$$1 = \sqrt{\frac{\omega\mu_0\sigma}{2}}\,\delta \qquad (4.31)$$

$$\delta = \sqrt{\frac{2}{\omega\mu_0\sigma}} = \sqrt{\frac{1}{f\sigma(4\pi^2*10^{-7})}} \approx \frac{503}{\sqrt{\sigma f}} \qquad (4.32)$$

From this it can be seen that the skin depth is inversely proportional to the frequency of the MT signal which means that lower frequency signals will attenuate slower than high frequency signals and have a greater skin depth. This means lower frequency signals will propagate further through a medium than higher frequency signals.

4.2.5 The Impedance Tensor in 1D

From equation (4.18), it can be seen that the impedance is dependant on the perpendicular components of the electric and magnetic fields and can be expressed as a tensor quantity:

$$\begin{bmatrix}E_x\\E_y\end{bmatrix} = \begin{bmatrix}Z_{xx} & Z_{xy}\\Z_{yx} & Z_{yy}\end{bmatrix}\begin{bmatrix}H_x\\H_y\end{bmatrix} \qquad (4.33)$$

For a 1D resistivity structure, the values of the diagonal components of the impedance tensor will equal zero, since the MT signals produce no parallel electric and magnetic field components. Also, because the measured apparent resistivity of the Earth does not vary in the *x* or *y* directions for a 1D resistivity structure, the magnitude of the impedance is equal for both Z_{xy} and Z_{yx}. Then (4.33) becomes:

$$\begin{bmatrix}E_x\\E_y\end{bmatrix} = \begin{bmatrix}0 & Z\\-Z & 0\end{bmatrix}\begin{bmatrix}H_x\\H_y\end{bmatrix} \qquad (4.34)$$

(note that the sign difference of Z_{xy} and Z_{yx} in (4.34) is due to the perpendicular orientation of the measured impedance values).

4.2.6 Magnetotelluric Response of a 2D Resistivity Structure

Assume an Earth structured such that the resistivity only changes in two dimensions, that is, the resistivity varies with depth in the z-direction, laterally in the y-direction, and remains constant in the x-direction (Figure 4.3 (b)). Maxwell's equations (4.3) and (4.4) can then be used to form two sets of equations, one independent of B_x known as the transverse electric mode (or TE):

$$\frac{\partial B_z}{\partial y} - \frac{\partial B_y}{\partial z} = \mu\sigma E_x \quad (4.35)$$

$$\frac{\partial E_x}{\partial z} - \frac{\partial E_z}{\partial x} = -i\omega B_y \quad (4.36)$$

$$\frac{\partial E_y}{\partial x} - \frac{\partial E_x}{\partial y} = -i\omega B_z \quad (4.37)$$

and one set independent of E_x known as the transverse magnetic mode (or TM):

$$\frac{\partial E_z}{\partial y} - \frac{\partial E_y}{\partial z} = -i\omega B_x \quad (4.38)$$

$$\frac{\partial B_x}{\partial z} - \frac{\partial B_z}{\partial x} = \mu\sigma E_y \quad (4.39)$$

$$\frac{\partial B_y}{\partial x} - \frac{\partial B_x}{\partial y} = \mu\sigma E_z \quad (4.40)$$

It can then be shown that equations (4.35), (4.36), and (4.37) can then be combined to form one equation in terms of E_x:

$$\frac{\partial^2 E_x}{\partial y^2} + \frac{\partial^2 E_x}{\partial z^2} = i\omega\mu\sigma E_x \quad (4.41)$$

and equations (4.38), (4.39), and (4.40) can be combined similarly to form one equation in terms of B_x:

$$\frac{\partial^2 B_x}{\partial y^2} + \frac{\partial^2 B_y}{\partial x^2} = i\omega\mu\sigma B_x \quad (4.42)$$

From these equations, the impedances for the transverse electric and transverse magnetic modes can be calculated (Z_{xy} and Z_{yx} respectively).

The impedance of the 2D Earth can be described by an impedance tensor such that:

$$\begin{bmatrix} E_x \\ E_y \end{bmatrix} = \begin{bmatrix} 0 & Z_{xy} \\ Z_{yx} & 0 \end{bmatrix} \begin{bmatrix} H_x \\ H_y \end{bmatrix} \quad (4.43)$$

where $|Z_{xy}| = |Z_{yx}|$ only in the 1D Earth, otherwise $Z_{xy} \neq Z_{yx}$. Thus, depending on which perpendicular components of the MT signal are measured (E_x and H_y, or E_y and H_x) a different value for apparent resistivity will be measured (ρ_{xy} or ρ_{yx}, respectively). In the 2D case, the diagonal components of the impedance tensor are both zero when either the x-axis or y-axis is aligned with the strike direction of the 2D resistivity structure.

4.2.7 Magnetotelluric Response of a 3D Resistivity Structure

Consider an Earth where resistivity varies in all three directions (Figure 4.3 (c)). Maxwell's equations can no longer be separated into the TE and TM modes as in the 2D case. The 3D impedance tensor then becomes:

$$\begin{bmatrix} E_x \\ E_y \end{bmatrix} = \begin{bmatrix} Z_{xx} & Z_{xy} \\ Z_{yx} & Z_{yy} \end{bmatrix} \begin{bmatrix} H_x \\ H_y \end{bmatrix} \qquad (4.44)$$

where the diagonal components, Z_{xx} and Z_{yy}, have a non-zero value regardless of the orientation of the x and y axes, and generally $Z_{xy} \neq Z_{yx}$.

4.2.8 Tipper

The variation of the vertical magnetic field, H_z, can also be used. The ratio between the vertical magnetic field component and each horizontal component is called the "tipper":

$$T_{zx} = \frac{H_z}{H_x} \qquad (4.45)$$

$$T_{zy} = \frac{H_z}{H_y} \qquad (4.46)$$

This is a dimensionless, complex value that is sensitive to conducting bodies within the subsurface (Unsworth, 2019b).

4.2.9 The Phase Tensor

The phase tensor is a component of MT data that is resistant to galvanic distortion effects and can be used to determine the dimensionality of MT data as well as to determine the geologic strike for a regional conducting area. Caldwell et al., (2004) define the phase tensor as:

$$\boldsymbol{\Phi} = \boldsymbol{X}^{-1}\boldsymbol{Y} = \begin{bmatrix} \phi_{11} & \phi_{12} \\ \phi_{21} & \phi_{22} \end{bmatrix} \qquad (4.47)$$

where $\boldsymbol{X}$ and $\boldsymbol{Y}$ are the real and imaginary components respectively of the impedance tensor $\boldsymbol{Z}$:

$$\boldsymbol{Z} = \boldsymbol{X} + i\boldsymbol{Y} \qquad (4.48)$$

$\boldsymbol{\Phi}$ can be rewritten using coordinate invariants φ_{max}, φ_{min}, β, and the angle α as:

$$\boldsymbol{\Phi} = \begin{bmatrix} \cos(\alpha-\beta) & -\sin(\alpha-\beta) \\ \sin(\alpha-\beta) & \cos(\alpha-\beta) \end{bmatrix} \begin{bmatrix} \phi_{max} & 0 \\ 0 & \phi_{min} \end{bmatrix} \begin{bmatrix} \cos(\alpha+\beta) & \sin(\alpha+\beta) \\ -\sin(\alpha+\beta) & \cos(\alpha+\beta) \end{bmatrix} \qquad (4.49)$$

where φ_{max} and φ_{min} are the singular values of $\boldsymbol{\Phi}$, and α and β are given by:

$$\alpha = \frac{1}{2}\tan^{-1}\frac{\phi_{12}+\phi_{21}}{\phi_{11}-\phi_{22}} \qquad (4.50)$$

and

$$\beta = \frac{1}{2}\tan^{-1}\frac{\phi_{12}-\phi_{21}}{\phi_{11}+\phi_{22}} \qquad (4.51)$$

Using this form, the phase tensor can be represented geographically as an ellipse where the major and minor axes are given by φ_{max} and φ_{min} respectively, and the ellipse is aligned with the major axis having an angle of $(\alpha - \beta)$.

For MT data that is 1-dimensional, the singular values will be equal, and thus the phase tensor will be plotted as a circle, with no preferential orientation. For 2D data, the value of β will be zero, and the ellipse will align itself parallel to the strike of a local conducting feature, however due to a 90° ambiguity in the 2D phase tensor, either the major or the minor axis will align with the strike and thus the interpretation of the strike direction requires other knowledge of the study area. For 3-dimensional MT data, β will no longer be non-zero. This is typically represented by colouring the ellipse to indicate its value of β. This is detailed further in Caldwell et al. (2004).

4.3 Synthetic Examples of 1D, 2D, and 3D Resistivity Structures

Three synthetic models were constructed to display the differences between the predicted response of 1D, 2D, and 3D magnetotelluric data. These synthetic models utilized the same station geometry and frequency ranges as the real MT data analyzed in the next chapter.

4.3.1 MT Response of a 1D Resistivity Model

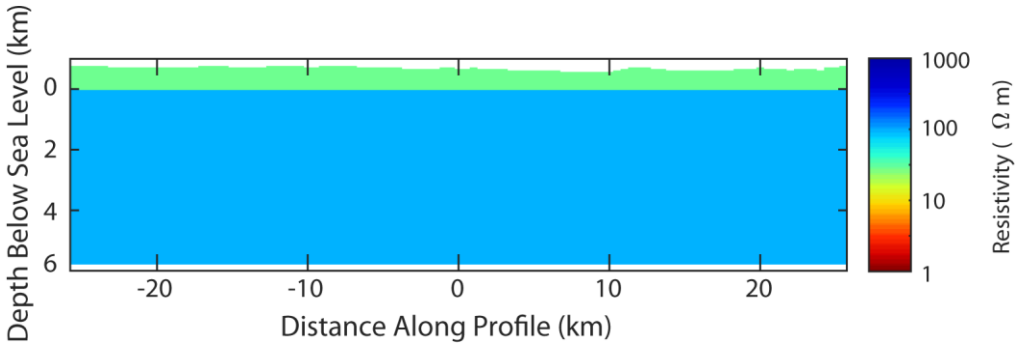

Figure 4.4: 1D synthetic model of a 1 km thick 30 Ωm layer above a 100 Ωm halfspace.

To demonstrate the data response for a 1D MT model, a synthetic model was created consisting of a 1 km thick 30 Ωm layer above a 100 Ωm halfspace (Figure 4.4). The apparent resistivity and phase curve for this model can be seen below in Figure 4.5, pseudosections are shown in Figure 4.6. Note that ρ_{xy} and ρ_{yx} are equal for 1D MT data. The two layers are well resolved in the pseudosections.

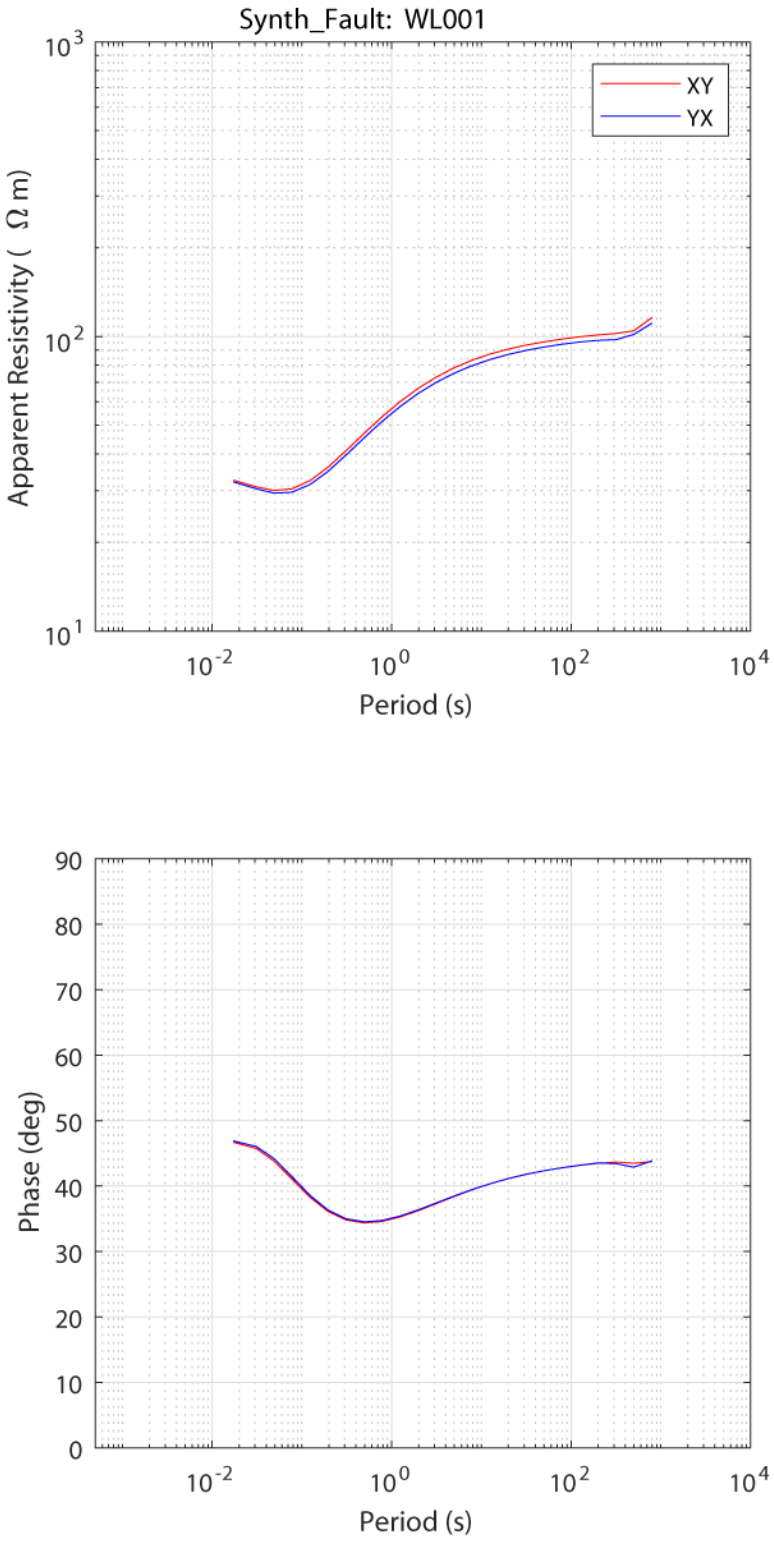

Figure 4.5: Apparent resistivity and phase curves for the 1D resistivity model. The model consists of a 30 Ωm layer that is 1 km thick situated above a 100 Ωm halfspace.

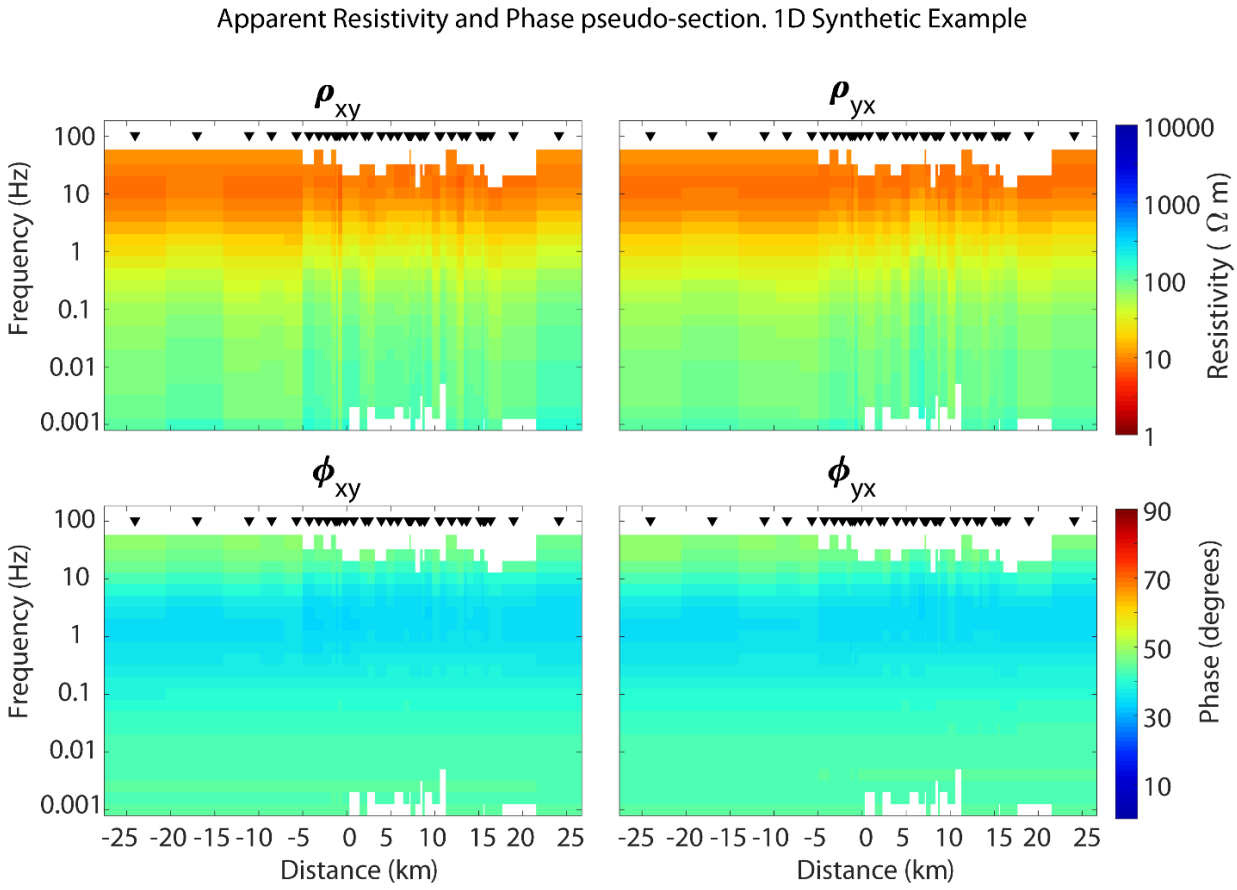

Figure 4.6: Apparent resistivity and phase pseudosections for a 1D resistivity model.

4.3.2 Example of a 2D MT Model

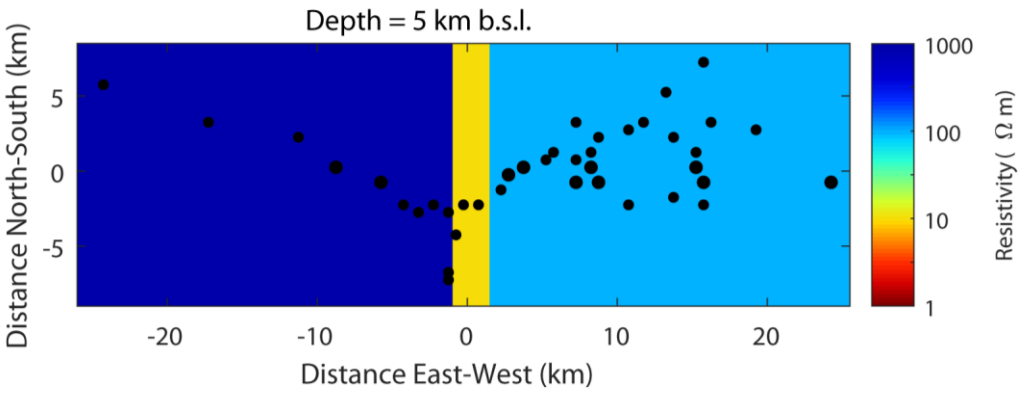

Figure 4.7: Horizontal slice of 2D synthetic model.

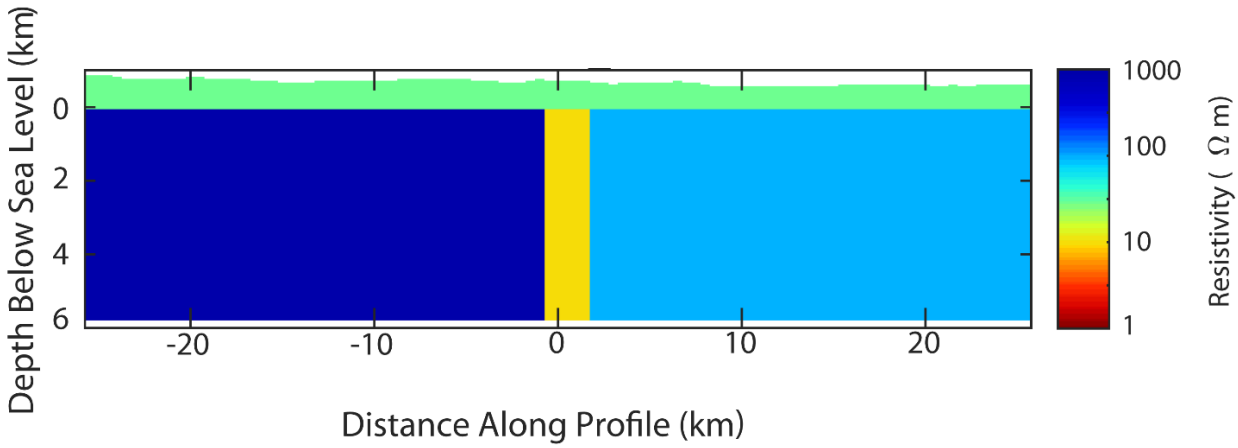

Figure 4.8: Vertical slice of 2D synthetic model.

The example for a 2D MT model consists of a 1 km 30 Ωm layer over a hypothetical fault system. The western portion of the fault system is a 1000 Ωm block and the eastern portion is a 100 Ωm block. Situated in the middle of these blocks is a 2 km wide 10 Ωm fault. The fault system extends infinitely in the x-direction (Figures 4.7 and 4.8). A pseudosection showing the data response for a profile perpendicular to the fault can be seen in Figure 4.9. For this 2D MT dataset, ρ_{xy} and ρ_{yx} are equivalent to the TE and TM modes respectively. It can be seen in the pseudosection plot that the locations of the upper conducting layer, western resistive block, and fault are well resolved, while the eastern 100 Ωm block is not.

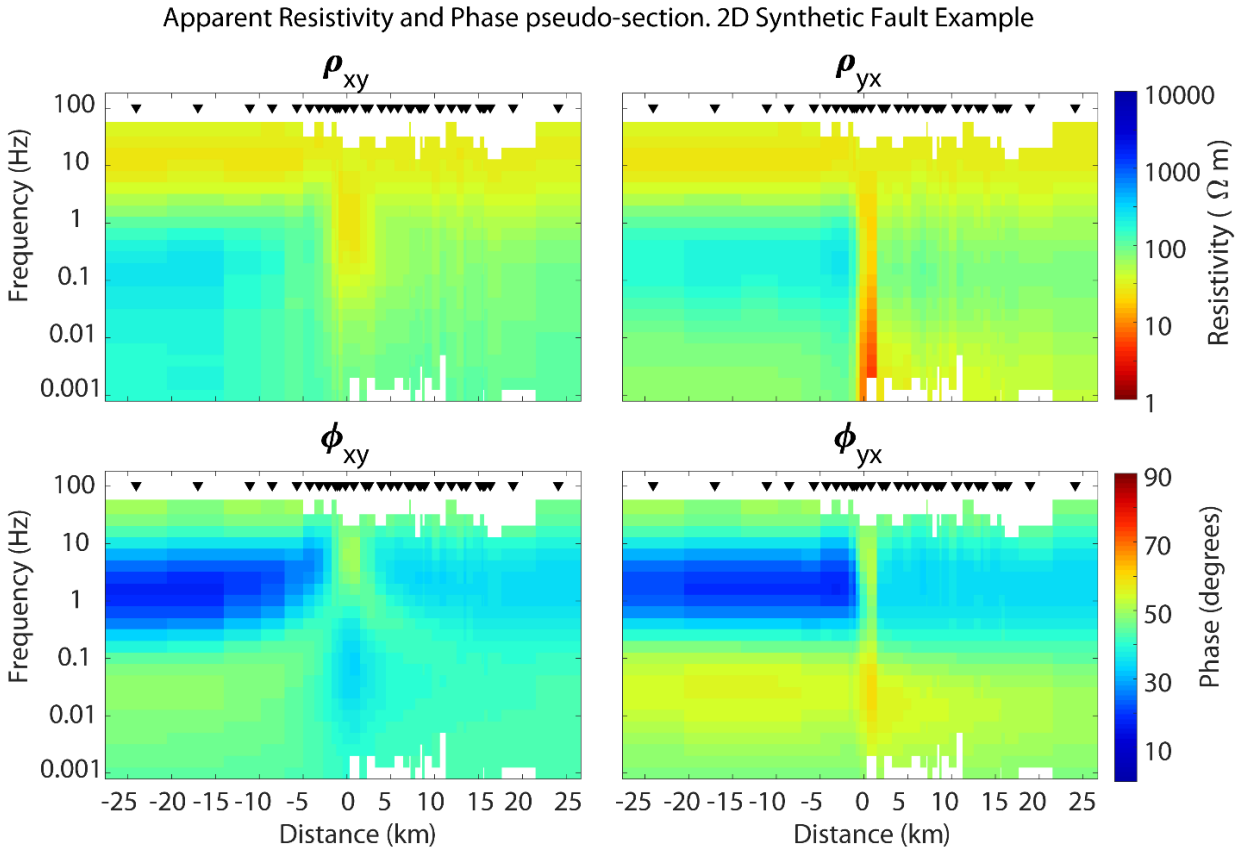

Figure 4.9: Pseudosections of apparent resistivity and phase for the 2D synthetic fault example.

4.3.3 Example of a 3D MT Model

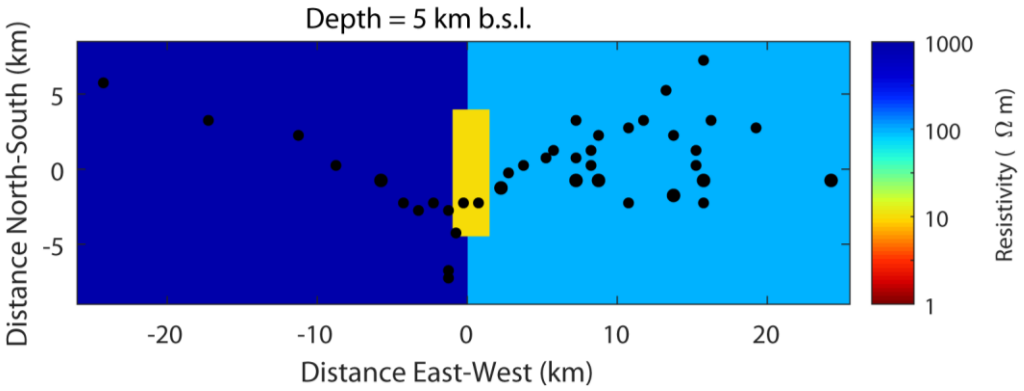

Figure 4.10: Horizontal slice of 3D synthetic model.

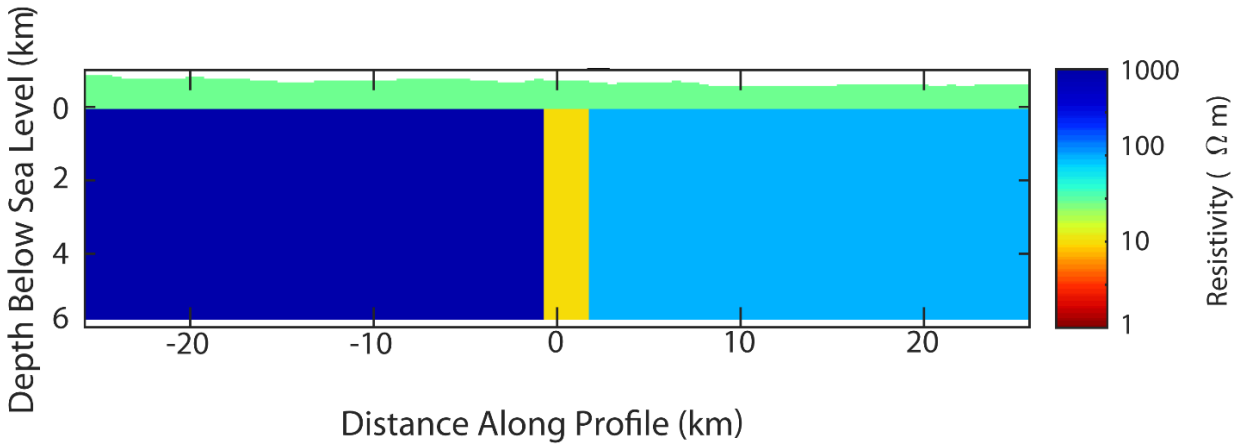

Figure 4.11: Vertical slice of 3D synthetic model.

The 3D example model is very similar to the 2D model, except the 10 Ωm conducting fault has a horizontal extent of 8 km in the strike direction (Figures 4.10 and 4.11). A pseudosection taken below a E-W profile can be seen in Figure 4.12. Unlike the 2D case, TE and TM modes cannot be resolved as the diagonal components of the impedance tensor are non-zero. Despite this, the pseudosection is very similar to the 2D case.

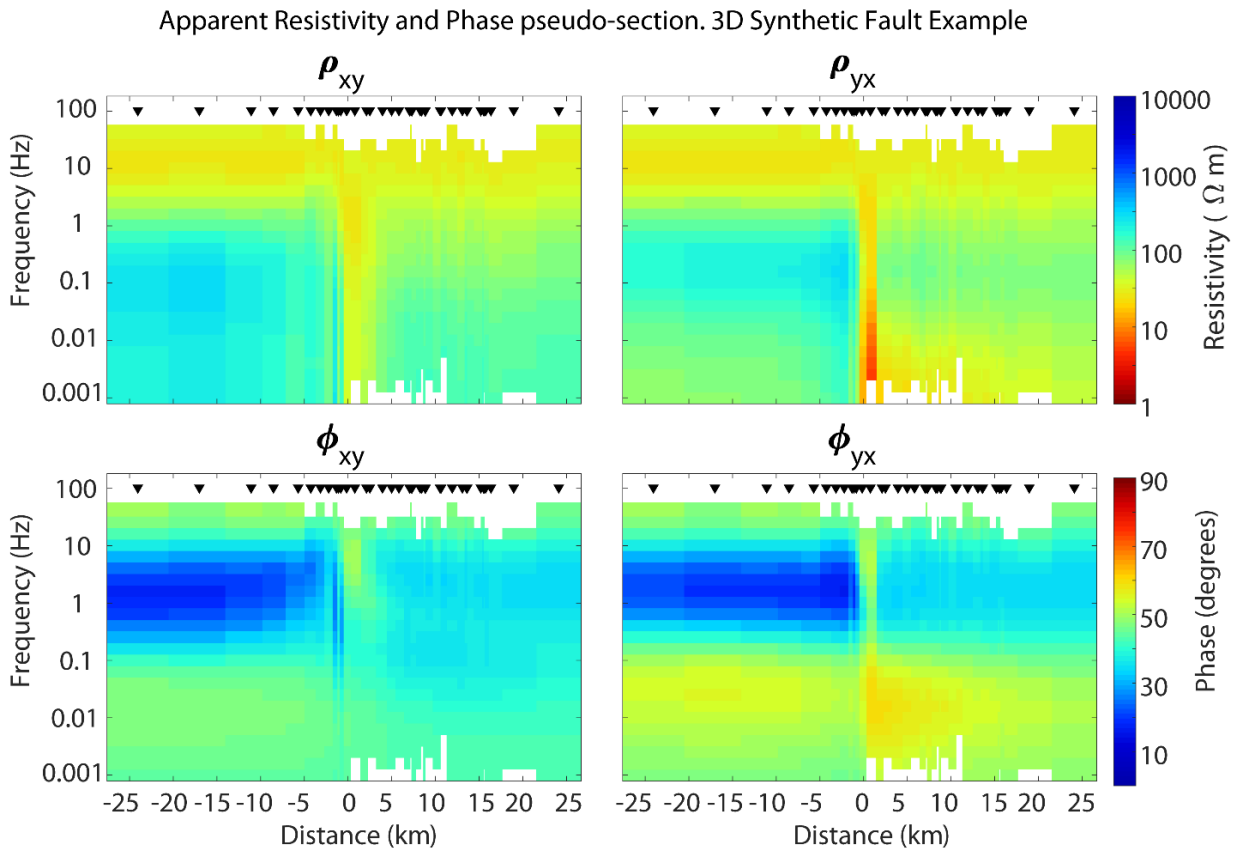

Figure 4.12: Pseudosections of apparent resistivity and phase for the 3D synthetic fault example.

4.4 MT Data Collection

MT signals occur in various frequency ranges. Low frequency signals below 1 Hz are generated by interactions between Earth's magnetic field and solar wind, while high frequency signals above 1 Hz are caused by lightning strikes. Data is typically collected using induction coils (for broadband MT 10000 – 0.001 Hz) or fluxgate magnetometers (long period MT, 0.0001 – 1 Hz) for the magnetic component of the field and non-polarizing electrodes for the electric component. Three magnetic field sensors are buried mutually perpendicular to each other facing North, East, and vertically downward, while four non-polarizing electrodes are buried North, South, East, and West of the survey site forming two perpendicular dipoles (Figure 4.13). Note that for a long period MT survey, fluxgate magnetometers are used in place of the induction coils for the magnetic field measurements. The equipment is left to record for an amount of time ranging from hours to weeks depending on the desired recording frequencies. The data is then processed using software in order to calculate the apparent resistivity, phase, and tipper at each collected frequency which can then be used as inputs for inversion algorithms which can

calculate potential subsurface resistivity models.

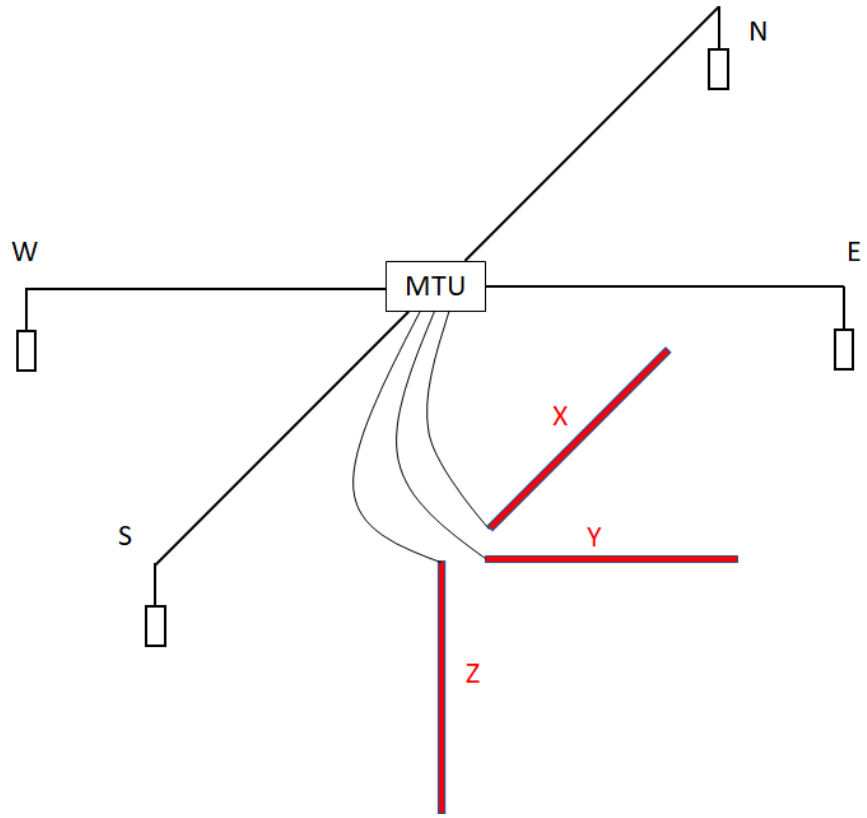

Figure 4.13: Schematic of a typical magnetotelluric station. 4 electrodes are buried North, South, East, and West of the control unit and connected to the control unit via wires. 3 induction coils are buried facing North, East, and downward and are also connected to the control unit. The control unit is powered by a 12V battery which can be supplemented with a solar panel for longer period surveys.

From the skin depth equation derived in section 4.2.4, the depth of investigation of an MT survey will depend on the lowest frequency recorded. Thus, there are several types of MT techniques that depend on the frequencies measured, the depth of investigation required for the survey, and the type of magnetic field sensors used (Unsworth, 2019c):

- **Audio magnetotellurics (AMT)** utilizes high frequency signals between 10000 – 1 Hz, with a depth of penetration of 1 – 2 km, and a recording time of several hours. Magnetic field measurements are made with induction coils.
- **Broadband magnetotellurics (BBMT)** utilizes frequencies between 1000 – 0.001 Hz with a depth of penetration up to 10 km. These surveys usually require station recording times of 1 -2 days and also utilize induction coils to measure the magnetic fields.

- **Long period magnetotellurics (LMT)** uses frequencies in the range of $1 – 10^{-4}$ Hz, reaching depths of up to hundreds of kilometers, and requiring recording times of several weeks per station. These surveys require the use of fluxgate magnetometers to measure the magnetic field data.

4.5 Magnetotelluric Time Series

The MT signals are recorded by the equipment as raw time series data which must be converted into frequency domain impedance data in order for the data to be analyzed and interpreted. This can be done using a variety of methods including algorithms developed for research purposes or commercial software packages. For the analysis of the Watson Lake MT data, both the Egbert processing method (Egbert, 1997) and the Phoenix EMPower software were utilized.

The raw measurements of the electric and magnetic field data are recorded as functions of time. The frequency spectra of the electric and magnetic field components are required in order to calculate the impedance, so the data must be transformed into the frequency domain. This is done by applying a Fourier transform to the time series data. Then the data is sampled for each frequency by taking a weighted average of adjacent frequencies. In this stage preliminary denoising techniques such as coherence sorting, which looks for coherence between electric and magnetic field data for specific frequencies, and remote referencing (Gamble et al., 1979), which looks for coherence between the magnetic signals of two nearby stations, can be utilized. If the signals are found to be incoherent then data points are removed until the desired level of coherence is reached, or a maximum mount of data points are removed. After the incoherent noise is removed, the frequency spectra data for the electric and magnetic fields are obtained and impedance can be calculated via equation 4.18 above. It is important to note that by converting the raw time series data into the impedance data, information regarding the origin of the signals is lost and cannot be recovered.

4.6 Magnetotelluric Inversion

Time series processing converts the raw time series data into measurements of apparent resistivity and phase as a function of frequency. However, the measured values of apparent resistivity are not the true resistivity of the subsurface as a function of depth and horizontal location, they are averaged over the surrounding area as the EM signal propagates through the subsurface and are a function of frequency.

Models of true resistivity as it varies spatially are required to obtain a meaningful interpretation of the data. The process of inversion takes the measured apparent resistivity, phase, and tipper data and uses it to create a model of true resistivity as a function of horizontal location and depth. Due to the nature of the inverse problem, there are an infinite number of possible models that can explain a given set of measured MT data, so statistical methods are used to determine the most likely resistivity model depending on the inversion parameters. Inversion can be undertaken for 1D, 2D, and 3D MT data, but the computational power and computing time required for the algorithms will be much greater for higher dimensional inversions. 1D inversions can be done using a typical desktop computer and may take on the order of minutes to complete, 2D inversions can also be performed on a desktop, but may take on the order of hours to complete. For 3D inversions, specialized computing clusters such as the Cedar cluster provided by the Digital Research Alliance of Canada are necessary. These inversions may take on the order of days to weeks to complete.

4.7 Interpretation of Resistivity

Once a resistivity model has been obtained, the resistivity values can be interpreted. Variations in subsurface electrical resistivity are the result of variations in the composition of the structure of the Earth. Figure 4.14 below displays ranges of typical resistivity values for common rock types and mineral deposits (Palacky, 1988). Pure materials will conduct electricity depending on the availability of charge carriers within the material. For example, saline fluids contain many free ions which can allow electric currents to easily flow within the fluid. Materials such as sulphides and graphite will have free electrons available to act as charge carriers, giving them low values of electrical resistivity. Other materials where free charges are not freely available will act as resistors, these can include many mineral types such as quartz and feldspar.

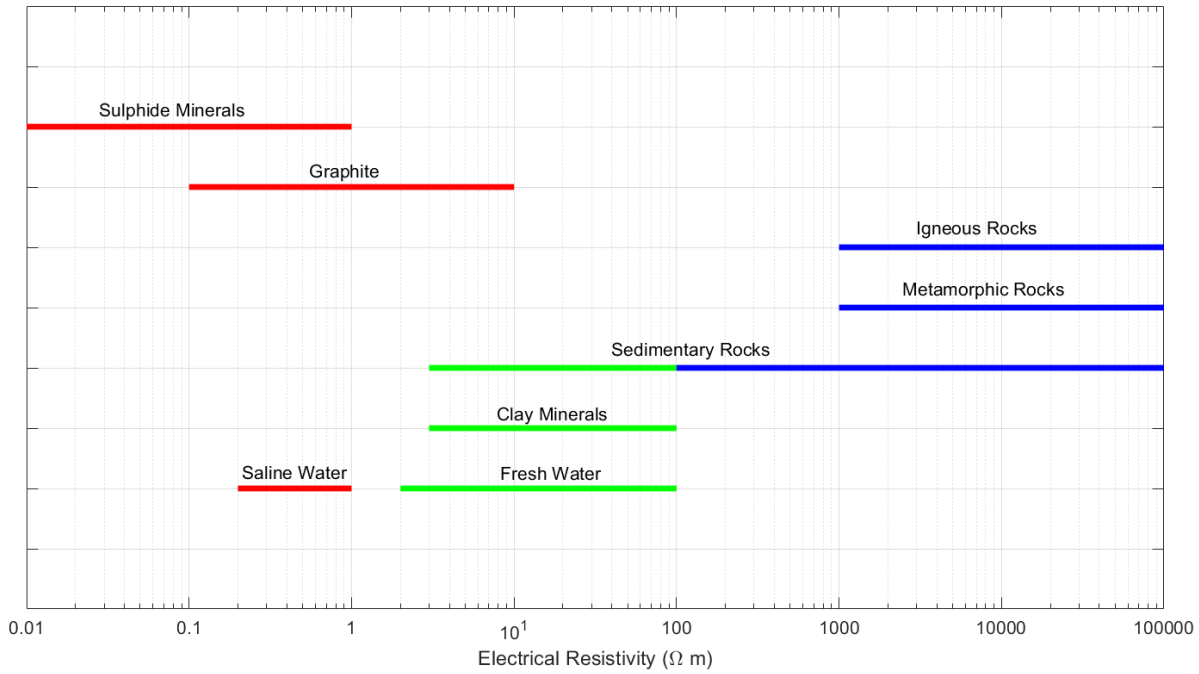

Figure 4.14: Electrical Resistivity ranges for various rock types and materials (modified from Palacky, 1988).

Most rocks are composed of a mixture of different mineral types and thus the resistivity of the rock will depend on the material it is composed of and the relative proportions of those materials. To determine the resistivity in these cases, mixing laws such as Archie's law must be used. Archie's Law is expressed as:

$$\rho = \rho_w a S^{-n} \phi^{-m} \qquad (4.52)$$

where ρ is the resistivity of the rock, ρ_w is the resistivity of the pore fluid, a is the tortuosity of the rock, S is the saturation of the pores, n is an empirical constant (equal to 1), ϕ is the porosity of the rock, and m is the cementation factor (equal to 2 in the case of spherical pores, or 1 in the case of ellipsoidal pores) (Archie, 1942). This demonstrates that the bulk resistivity of the rock is independent of the rock grains and instead depends only on the fluid within the pore space.

Fluid resistivity can also be determined using the amount of Total Dissolved Solids (TDS) in the fluid using the empirical equation described from observations of borehole fluids in Alberta

$$\rho_w = 4.5 * TDS^{-0.85} \qquad (4.53)$$

Where TDS is measured in g/litre (Block, 2001).

Clay minerals conduct electricity through an electrical double layer on the surface of the clay which allows for enhanced ion movement. This causes the clay to have very low values of electrical resistivity. Certain clays will also form via hydrothermal alteration at specific temperatures, such as smectite (~100 °C) and illite (200 – 300 °C) allowing them to act as a geothermometer (Ussher et al., 2000). If these types of clays are imaged by the MT inversion model, it can indicate the temperature of the surrounding rock is suitable for geothermal development.

Partial melt will also have a lower resistivity than solid rock with the same composition. This is because it is much easier for ions to flow through the melt than through the solid rock, and thus it is also easier for electricity to flow (Unsworth, 2019d).

Different rock types will have different compositions and therefore conduct electricity differently. For example, sedimentary rocks such as shales and sandstones will typically have lower values of electrical resistivity than igneous and metamorphic rocks. Typically, felsic igneous rocks will also have higher values for resistivity than mafic igneous rocks.

Sedimentary rocks are often composed of resistive grains, but the pore space between grains may contain fluids that can alter the resistivity. Saline pore fluids will lower the resistivity according to Archie's law and typically control the bulk resistivity of the rock (Nesbitt, 1993), while resistive fluids such as hydrocarbons will increase the bulk resistivity. Rocks with larger values of porosity and saturation will also have lower resistivity as the proportion of pore fluids within the rock will be greater.

Igneous rock types will be mainly resistive unless there is conducting material present, such as sulphides or graphite. From Figure 4.14, sulphides and graphite have some of the lowest values of resistivity for geological materials, the presence of these materials in igneous rock types can greatly reduce the bulk resistivity.

Once magnetotelluric inversions are completed, it is necessary to interpret the possible causes of the conductors and/or resistors present in the inversion model. It is often useful to compare the MT data with the results of other geophysical surveys undertaken in the survey area and with the known geology

of the area to better constrain possible explanations for the inversion model features. These concepts are explored in more detail in later chapters.

4.8 Conclusions

The magnetotelluric method is a preferred electromagnetic geophysical method for locating potential sources of geothermal energy. The method utilizes naturally occurring electromagnetic waves that travel from the atmosphere into the Earth to model subsurface electrical resistivity variations. Areas of low electrical resistivity are targets for geothermal energy production as the low resistivity values could be indicative of the hot pore fluid necessary for the operation of a geothermal energy plant. Higher resistivities generally indicate dry rocks, but it should be noted that the transition from smectite to illite is associated with an increase in resistivity and can indicate an increase in temperature. Here, the basic mathematical and physical concepts governing the MT method are discussed, the next chapter will focus on MT data collection and processing.

Chapter 5: Magnetotelluric Data Collection and Processing at Watson Lake

5.1 Introduction

The operation of conventional geothermal systems requires the presence of heat, pore fluid, and permeable rock types. The heat is the energy source used by the geothermal system while the pore fluid is necessary to extract the heat needed for electricity production. Permeable rock allows for circulation of the pore fluid within the hot rock, and aid in the extraction of the hot pore fluids. Geophysical techniques can be utilized to identify areas where pore fluids within permeable rock types may be present. Electromagnetic (EM) techniques are often used to locate these areas since they model the subsurface electrical resistivity, and the pore fluid would have a much lower electrical resistivity than the surrounding host rock.

It is not possible to directly measure the temperature of the subsurface using EM methods, however, EM methods can be used to locate areas such as clay caps which can be utilized to indirectly estimate past and present temperatures. Clay caps are created through hydrothermal alteration of the host rock, which could indicate the past or current presence of hot pore fluids. These clay caps are composed of high conductivity clay minerals such as illite and smectite, making them easily identifiable by electrical resistivity methods. These minerals will form at specific temperature ranges. Illite can be found at temperatures between 200 – 300°C, while smectite forms at temperatures below 200°C. Areas with temperatures between 100 – 300°C can be characterized by interbedded layers of smectite and illite. Identification of these minerals can therefore allow for the estimation of past or present temperatures (Ussher et al., 2000).

One favoured technique for measuring subsurface electrical resistivity is the magnetotelluric (MT) method detailed in the previous chapter. MT is often used for geothermal exploration because it has a deeper depth of investigation than other EM techniques, allowing it to locate potential areas of hot pore fluids required for geothermal development (Pellerin et al., 1996). As geothermal exploration began at Watson Lake, the only previous MT data collected in the Watson Lake area was that collected as part of the Lithoprobe SNORCLE transect (Ledo et al., 2002). It consisted of a 2D profile with a broad station spacing of 10-15 km between stations which was inadequate for locating near-surface features that would be of interest for geothermal exploration. A 3D survey grid with finer station spacing is required to obtain data with the necessary near-surface resolution. The collection of this new MT data set was undertaken in the summer of 2021. This chapter describes the collection and processing of the 3D MT grid at Watson Lake and discusses the results of the phase tensor and induction vector analysis.

5.2 MT Data Collection

Geothermal exploration requires shallow reservoirs within the upper 1- 10 km of Earth's crust to be economically feasible, and thus a BBMT survey was conducted to locate shallow electrical resistivity anomalies.

Broadband magnetotelluric data were collected in the Watson Lake area during the summer 2021 field season from July 19 to August 4. A total of 36 separate MT stations were deployed and allowed to run overnight to collect data. At 10 of the 36 stations, the battery at the station was replaced and it was allowed to continue to collect MT data for another night, resulting in a total of 46 separate data runs. This was done not only to increase the sample size of data for those stations, but to also allow for simultaneous data collection at multiple sites to utilize the remote reference method (Gamble et al., 1979) for noise removal during processing.

MT stations were mainly deployed by truck along the Alaska Highway and along Highway 37 to the South. Stations were deployed with a spacing of approximately 1 km between stations (Figure 5.1). The equipment was typically placed several hundred meters into the forest along the highway in order to reduce potential noise caused by nearby traffic and to prevent potential theft or vandalism. Several MT stations were also placed along the banks of the Liard River, approximately perpendicular to the highway. Details for each station including recording dates, locations, configurations, etc. can be found in Table 5.1. Recording times for each MT station are plotted in Figure 5.2.

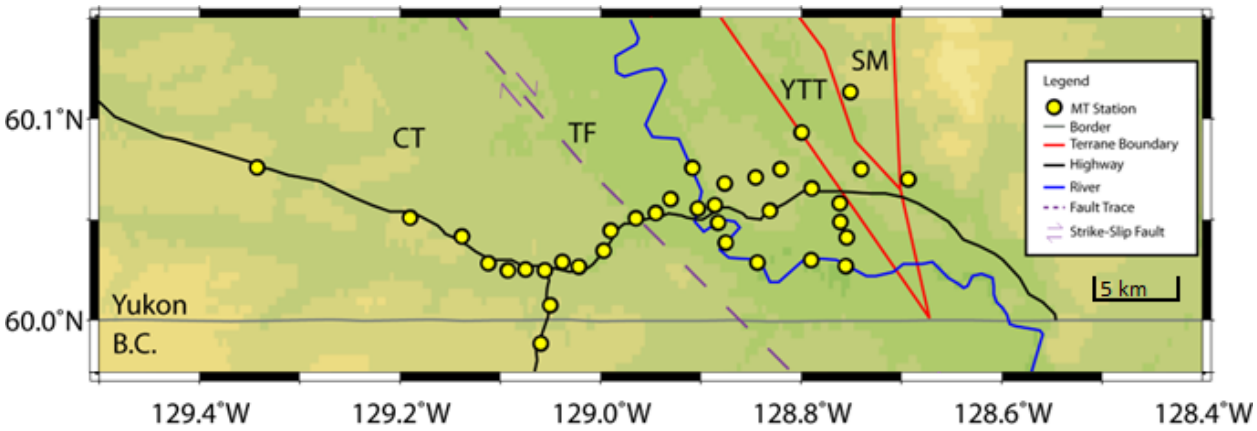

Figure 5.1: Map of survey area showing stations collected during summer 2021. The trace of the Tintina Fault is also plotted (Yukon Geological Survey, 2022) as well as the terrane boundaries (Yukon Geological Survey, 2020). TF = Tintina Fault, CT = Cassiar Terrane, YTT = Yukon-Tanana Terrane, SM = Slide Mountain Terrane.

Station Name	Date(s) of Recording	Number of Data Runs	Latitude (°N)	Longitude (°W)	Elevation (m)	N-S Dipole Length (m)	E-W Dipole Length (m)	Data Type	D+ RMS misfit (XY/YX)	Raw Data File Name
WL001	02/08/21 03/08/21	2	60.0759	129.3421	828.969	43	44	Z, T	0.29/0.28	10352_2021-08-02-180141 10352_2021-08-03-160214
WL002	24/07/21	1	60.0510	129.1894	824.345	77	71	Z, T	0.26/0.26	10379_2021-07-24-223107
WL003	02/0821	1	60.0416	129.1378	754.272	45	55	Z	0.28/0.26	10430_2021-08-02-203336
WL004	25/07/21	1	60.0283	129.1115	733.285	52	88	Z, T	0.48/0.16	10352_2021-07-25-205214
WL005	19/07/21 20/07/21 21/07/21	3	60.0247	129.0921	741.876	52	57	Z, T	0.31/0.26	10351_2021-07-20-013752 10351_2021-07-20-161706 10351_2021-07-21-172131
WL006	20/07/21	1	60.0252	129.0745	730.712	79	102	Z, T	0.49/0.32	10379_2021-07-20-194349
WL007	22/07/21	1	60.0248	129.0552	726.431	56	57	Z, T	0.42/0.64	10351_2021-07-22-182558
WL008	19/07/21	1	60.0290	129.0377	737.212	56	60	Z, T	0.25/0.22	10352_2021-07-20-010344
WL009	20/07/21 21/07/21	2	60.0266	129.0213	725.006	73	62	Z, T	0.32/0.40	10352_2021-07-20-224244 10352_2021-07-21-164750
WL010	25/07/21	1	60.0345	128.9967	664.525	88	71	Z, T	0.30/0.30	10379_2021-07-25-232158
WL011	22/07/21 23/07/21	2	60.0445	128.9897	710.281	84	50	Z, T	0.30/0.27	10352_2021-07-22-215249 10352_2021-07-23-233345
WL012	21/07/21 22/07/21	2	60.0533	128.9447	636.208	109	77	Z, T	0.40/0.43	10379_2021-07-21-213724 10379_2021-07-22-223738
WL014	23/07/21	1	60.0602	128.9299	613.528	56	52	Z, T	0.20/0.28	10351_2021-07-23-180224
WL015	30/07/21	1	60.0554	128.9026	604.979	51	58	Z, T	0.28/0.41	10379_2021-07-30-181439
WL016	28/07/21	1	60.0572	128.8859	631.662	50	42	Z, T	0.22/0.20	10351_2021-07-29-000342
WL017	23/07/21	1	60.0710	128.8451	743.169	88	73	Z, T	0.32/0.23	10379_2021-07-23-222309
WL018	24/07/21	1	60.0750	128.8202	716.492	51	56	Z, T	0.26/0.22	10352_2021-07-24-182121
WL019	28/07/21	1	60.0932	128.7993	717.793	46	46	Z, T	0.23/0.24	10379_2021-07-28-184837
WL020	30/07/21 31/07/21	2	60.1133	128.7509	754.083	51	50	Z, T	2.40/0.62	10351_2021-07-30-214934 10351_2021-07-31-202457
WL021	31/07/21 01/08/21	2	60.0679	128.8760	741.36	32	32	Z, T	0.32/0.42	10379_2021-07-31-174055 10379_2021-08-01-223503
WL022	31/07/21	1	60.0655	128.7892	690.502	27	26	Z, T	0.26/0.34	10430_2021-07-31-194140
WL023	01/08/21	1	60.0700	128.6929	704.628	43	41	Z, T	1.05/1.17	10352_2021-08-01-175217
WL030	26/07/21	1	60.0411	128.7544	671.673	55	56	Z, T	0.28/0.21	10351_2021-07-26-183506
WL031	27/07/21	1	60.0488	128.7608	681.372	55	55	Z, T	0.16/0.29	10351_2021-07-27-202403
WL032	28/07/21	1	60.0582	128.7612	668.206	71	52	Z, T	0.26/0.26	10352_2021-07-28-212358
WL035	27/07/21	1	60.0750	128.7400	721.033	85	51	Z, T	0.23/0.35	10352_2021-07-27-175002
WL040	25/07/21	1	60.0507	128.9645	646.662	58	49	Z, T	0.39/0.33	10351_2021-07-25-173928
WL050	26/07/21	2	60.0074	129.0497	784.704	69	73	Z, T	0.29/0.24	10379_2021-07-26-224830

	27/07/21									10379_2021-07-27-233934
WL051	01/08/21 02/08/21	2	59.9884	129.0594	814.582	53	55	Z, T	0.26/0.18	10351_2021-08-01-211246 10351_2021-08-02-215716
WL057*	03/08/21	1	60.0545	128.8309	749.324	44	54	Z, T	N/A	10430_2021-08-03-232040
WL058	03/08/21	1	60.0484	128.8826	603.106	54	54	Z, T	0.20/0.22	10351_2021-08-03-211925
WL059	03/08/21	1	60.0269	128.7552	606.253	33	31	Z, T	0.32/0.43	10379_2021-08-03-194041
WL060	29/07/21	1	60.0299	128.7898	598.019	57	50	Z, T	0.26/0.24	10351_2021-07-29-194600
WL061	29/07/21	1	60.0286	128.8432	600.404	51	54	Z, T	0.39/0.20	10352_2021-07-29-212933
WL062	29/07/21	1	60.0385	128.8750	601.511	56	45	Z, T	0.25/0.20	10379_2021-07-30-010036
WL063	29/07/21	1	60.0757	128.9081	605.933	47	44	Z	0.17/0.31	10430_2021-07-29-233038

*Table 5.1: Station data for Watson Lake 2021 MT survey. Displays the names, dates, locations, configurations, data types (Z = Impedance, T = Tipper) and D+ RMS misfits for collected stations. *Note that station WL057 was omitted from data inversions due to poor data quality.*

5.3 Field Measurements

MT data were collected using Phoenix MTU 5C equipment. The instruments consist of a control unit, a battery, three induction coils, and five electrodes. The induction coils were placed with two horizontal coils oriented North-South and East-West and a third coil oriented vertically. The induction coils and electrode dipoles were deployed in geomagnetic coordinates. This was done for ease of deployment (as it was not required to know the magnetic declination at each site prior to installation) and due to the various processing methods used to analyze the data. Some processing methods will automatically calculate the magnetic declination if the site is aligned to geomagnetic North, while others require the values to be set manually, which can be done after the survey has completed. The induction coils were also buried in order to prevent noise in the signal. If the coil moves in the geomagnetic field while recording, the movement will appear as noise in the signal as the coil will no longer be aligned in the correct direction. By burying the coils, they are kept stable and this reduces movement that may be caused by the wind, footsteps, or nearby traffic. Burying the coils also serves to insulate them from effects caused by temperature changes which can also cause noise in the recorded signal. For two stations where digging was difficult, only the horizontal coils were deployed, and vertical magnetic field data was not recorded.

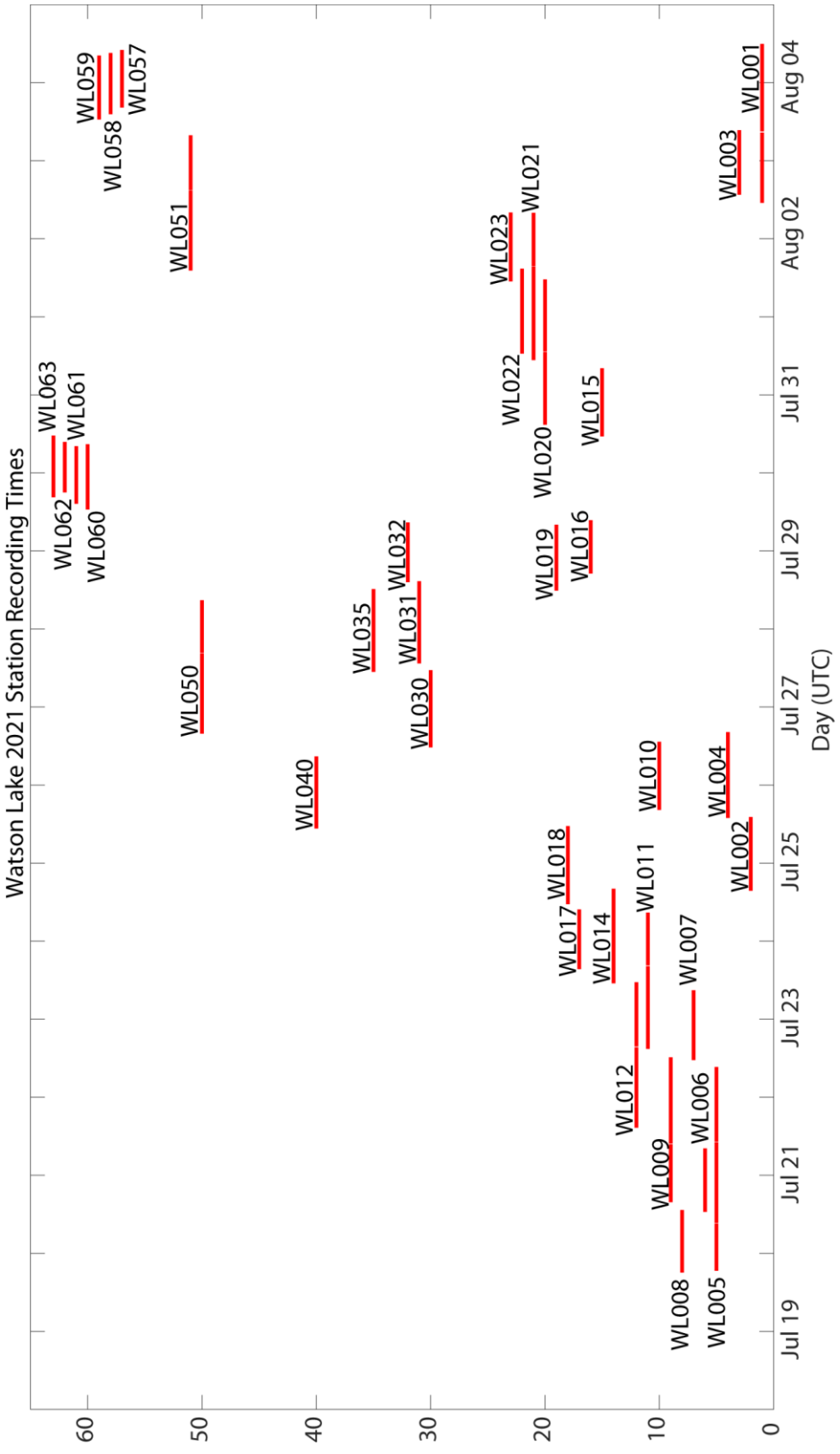

Figure 5.2: Plot showing the recording times for the Watson Lake 2021 MT station.

The electrodes were placed in dipole configurations with one electrode at each of the cardinal directions (North, South, East, West) and approximately 100 m of separation between electrodes, and the fifth was placed at the center of each station to act as a ground for the control unit. The electrodes were buried with bentonite clay to retain moisture. To reduce digging, some stations were deployed in a "T" configuration, with two electrodes at the site centre and three placed at the cardinal directions or an "L" configuration with three electrodes at the site centre and two placed at locations with directions perpendicular to each other. Longer dipoles will result in less noise in the measured signal as the electrodes will be further from potential noise caused by the rest of the equipment, however this can result in noise created by the dipole wires as well. One benefit of using shorter dipoles would be the reduced amount of labour and cost associated with the deployment of the MT station, since less wire is needed, and the stations will be deployed more quickly with shorter dipole lengths. However there is a trade-off between reducing the cost of deploying an MT station by using shorter dipoles, and the reduction of MT data quality related to the shorter wire lengths.

It must also be considered whether the assumptions required for the MT method mentioned in the previous chapter are satisfied. In Northern latitudes, the planar wave assumption may not be as valid due to interference from the aurora. This can be accounted for by adopting a method similar to Jones and Spratt (2002), where interference from the aurora is identified using vertical magnetic field measurements and MT data is only processed using time intervals where the interference is considered low.

5.4 MT Time Series

The time series MT data were collected using a continuous 150 Hz sampling band with sparse high frequency sampling at 24 KHz. In general, MT data collection utilizes multiple recording bands to reduce the overall size of the dataset. To record signals within a specific frequency range, the sampling frequency must be at least twice as large as the highest frequency in the desired range:

$$f_{sample} = 2 * f_{max} \qquad (5.1)$$

Where f_{sample} is the sampling frequency of the data (Hz) and f_{max} is the maximum recorded frequency (Hz). Additionally, signals must be recorded for an amount of time inverse to the lowest frequency and at least 20 cycles are usually needed to obtain an accurate measurement of the signal. That is:

$$T_{recording} = \frac{20}{f_{min}} \qquad (5.2)$$

where $T_{recording}$ is the length of time required to record the signal (seconds) and f_{min} is the minimum frequency within the recording range (Hz) (Unsworth, 2019c). Thus, it is not necessary to record the entire frequency range with the same sampling frequency required for the high frequency data as this would result in excessive amounts of data for the lower frequency signals. Instead, the frequency range is split into separate bands with their own sampling frequencies to reduce the necessary file size for the dataset. An example of the recorded time series for station WL017 is shown in Figure 5.3. It shows the variations in voltages measured over time for the electrode dipoles (top two panels) and the induction coils (bottom three panels). These signals are then converted into measurements of the electric and magnetic fields respectively.

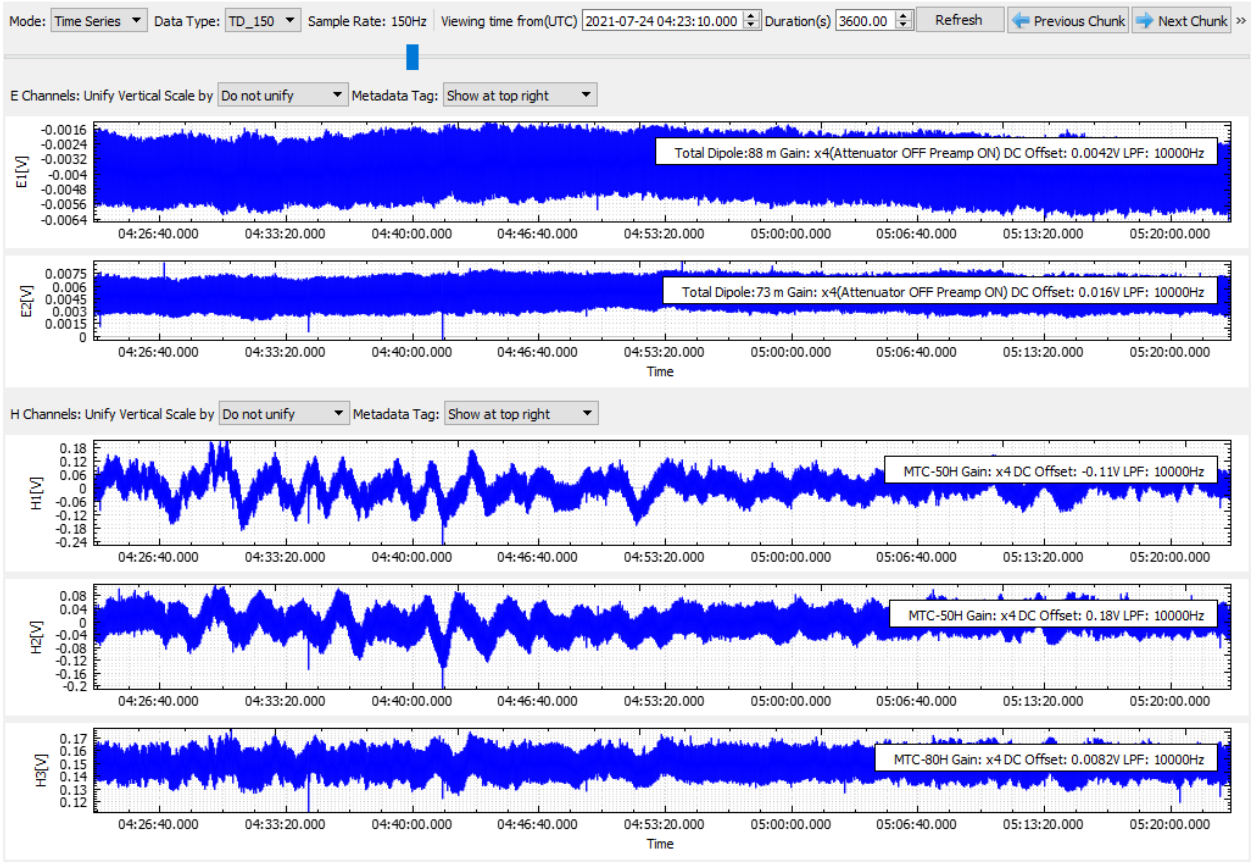

Figure 5.3: Screenshot from Phoenix EMPower software showing time series data for station WL017 for an hour of recording time. The top two curves display the raw North-South electric field data (E1) and the raw East-West electric field data (E2). The bottom three curves show the raw magnetic field data for the North-South (H1), East-West (H2), and vertical (H3) magnetic fields.

5.5 MT Data Processing From Time-Domain to Frequency Domain

The workflow for MT data processing was described in detail in Chapter 4. This chapter describes the processing of the Watson Lake MT dataset using this workflow.

As described previously, MT data are recorded as the raw measurements of time variations in the electric and magnetic fields within the Earth. The data analysis used to determine the resistivity structure of the Earth takes place in the frequency domain. This requires that the recorded time series data are converted into measurements of the electric and magnetic field from which the frequency domain impedance data can be calculated. The raw data set often contains many data points and depending on the recording times and sampling frequencies, can often be several gigabytes in size.

The data was collected as a time series (see Figure 5.3) and must be Fourier transformed into the frequency domain in to obtain usable apparent resistivity values for each corresponding signal frequency. After being transformed into the frequency domain, the data is then stacked either by directly stacking or by weighted stacking of neighbouring frequencies. After the data is obtained, remote reference and/or robust denoising methods can be used to remove noise in the signal that is the result of interference from sources other than the MT signals (Simpson and Bahr, 2005).

The remote reference method for denoising requires that two stations were being recorded simultaneously. This method compares the magnetic field or electric measurements at both stations in order to remove local noise from the station data. The noise can have a variety of sources including signals from power lines, electrical noise from nearby pipelines, or movement of the sensors. Since it is expected that local noise at one station will have no correlation with noise at the second station, while the source magnetic field signals should be the same provided the stations are located close to one another, the noise can be removed from both sets of station data (Gamble et al., 1979). This method is limited due to the inability to directly distinguish between noise and MT signal. If a station with relatively low levels of local noise uses a station with large amounts of noise present as a reference, it may result in a noisier signal after remote referencing. Comparisons should be made between station data before and after remote referencing to ensure that it has led to improvements in the data.

The Watson Lake MT data were processed with:

(1) Phoenix EMPower software.

and

(2) the Egbert time series processing method (Egbert, 1997).

Stations with multiple days of data runs were processed with those runs Fourier transformed before having their spectra stacked to yield more data samples per run and thus a more reliable average of the collected data. Remote reference and coherence sorting techniques were also applied to the data in order to reduce noise in the signal. Figure 5.4 displays the apparent resistivity, phase, and tipper data for station WL017 after remote referencing and coherence sorting and WL007 after coherence sorting. Both plots display a continuous signal with very little noise. Apparent resistivity, phase, and tipper curves can be found for all stations in the appendix.

In general, data quality across all stations was good, with very little noise likely due to the remote locations of the stations, away from power lines carrying large amounts of current. There were two stations that had issues with the data quality. The first station, WL057 had issues where the collected data below 0.1 Hz was out of phase. This station was not included in the data inversions. The other station, WL058 was left overnight along the Liard River. When recovered the next day it was evident that an animal (likely a wolf) had dug up one of the induction coils and chewed through the cable resulting in a loss of signal. The data recorded before the signal was cut-off was still in the frequency range collected at the other stations (100 – 0.001 Hz) and the station was included in the data inversions. Figures displaying the apparent resistivity, phase, and tipper curves for these two stations can be found in the appendix. In addition to the 35 usable stations from 2021, five stations from the SNORCLE transect were also included in the data inversions (Ledo et al., 2002). The resulting apparent resistivity, phase, and tipper curves were then manually edited to remove any remaining noisy data points.

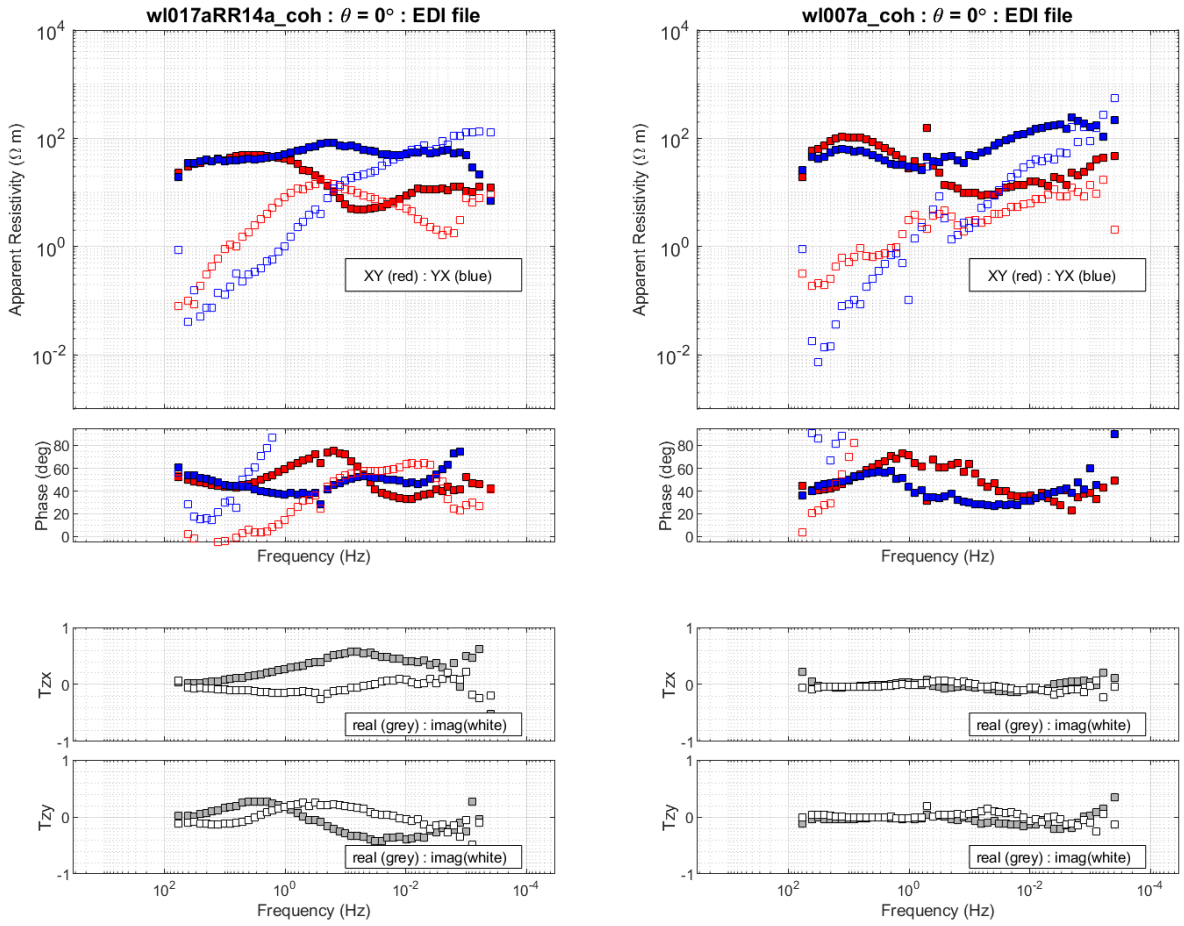

Figure 5.4: Apparent resistivity, phase, and tipper curves for stations WL017 after time series processing, remote reference, and coherence sorting have been applied and WL007 after time series processing and coherence sorting have been applied produced by the Egbert (1997) Processing code. The red curves represent data collected with the North-South electric field and the East-West magnetic field components. The Blue curves represent data collected with the East-West electric fields and the North-south Magnetic field components. Filled symbols represent the off-diagonal components of the impedance tensor (Z_{xy} (red) and Z_{yx} (blue)), while unfilled symbols represent the diagonal components (Z_{xx} (red) and Z_{yy} (blue)). The bottom two curves show the tipper data, the ratio between the vertical and horizontal magnetic field components. As the tipper is a complex value, both real and imaginary parts are plotted in grey and white respectively. Note that due to the skin effect, on these plots decreasing frequency is analogous to increasing depth.

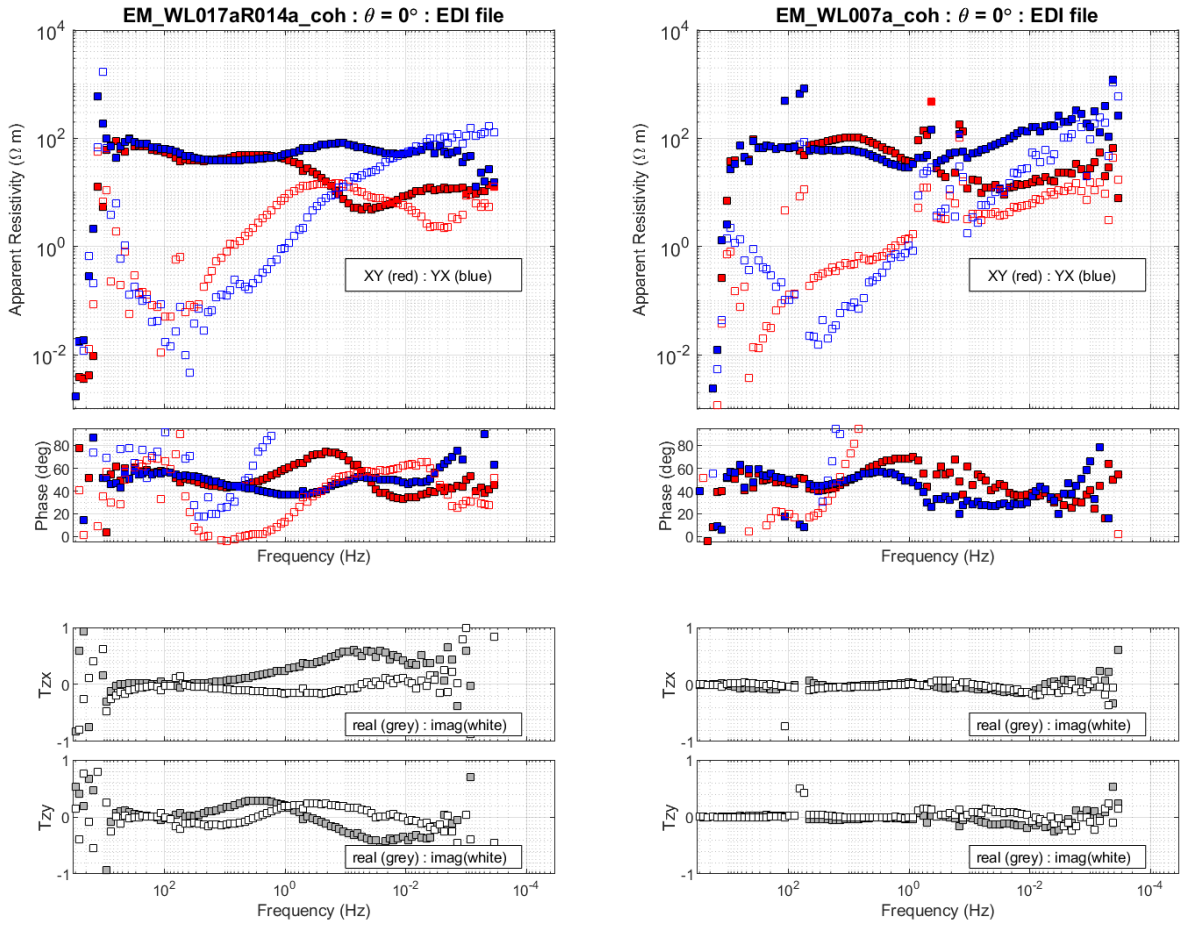

Figure 5.5: Apparent resistivity, phase, and tipper curves for stations WL017 after time series processing, remote reference, and coherence sorting have been applied and WL007 after time series processing and coherence sorting have been applied produced by the EMPower software. Note the similarities between the curves and those in Figure 5.4, confirming that station rotations from geomagnetic coordinates to geographic coordinates were correctly applied. The red curves represent data collected with the North-South electric field and the East-West magnetic field components. The Blue curves represent data collected with the East-West electric fields and the North-south Magnetic field components. Filled symbols represent the off-diagonal components of the impedance tensor (Z_{xy} (red) and Z_{yx} (blue)), while unfilled symbols represent the diagonal components (Z_{xx} (red) and Z_{yy} (blue)). The bottom two curves show the tipper data, the ratio between the vertical and horizontal magnetic field components. As the tipper is a complex value, both real and imaginary parts are plotted in grey and white respectively. Note that due to the skin effect, on these plots decreasing frequency is analogous to increasing depth.

5.6 Rotation Angle

For MT, the alignment of the equipment is crucial to proper data collection. For processing and analysis, the data must be aligned with geographic north, however the equipment is often deployed aligned with geomagnetic north to avoid complications with having to determine the magnetic declination for each site. After collection the data can then be rotated to geographic coordinates using the site's magnetic declination. In the EMPower software, magnetic declination must be manually input for each station, while the Egbert processing method assumes the stations are aligned with geomagnetic north and automatically calculates declination from the station GPS data and applies the rotation. As this survey was the first to utilize the Phoenix 5C equipment, care was taken to ensure that the rotations were correctly applied to the dataset. Comparison of the apparent resistivity, phase, and tipper curves for stations WL017 and WL007 for the Egbert method (Figure 5.4) and the EMPower software (Figure 5.5) is shown above. The similarity between the curves for both stations confirms that rotations were applied correctly.

5.7 D+ editing

To aid in the editing of anomalous data points, the D+ model for 1D MT data developed by Parker (1980) is used. This attempts to find a smooth curve model to fit the apparent resistivity and phase curves for a station and expresses the misfit between the smooth curve model and station data as a Root Mean Squared (RMS) misfit:

$$RMS\ misfit = \sqrt{\frac{\sum_{i=1}^{N}\left(\frac{\rho_i^{data} - \rho_i^{model}}{\rho_i^{error}}\right)^2 + \left(\frac{\phi_i^{data} - \phi_i^{model}}{\phi_i^{error}}\right)^2}{2N}} \qquad (5.3)$$

where N is the total number of resistivity data points, ρ_i^{data} and ρ_i^{model} are the apparent resistivity values of the station data and the model data respectively, ρ_i^{error} is the error value associated with the data measurement, φ_i^{data} and φ_i^{model} are the phase values of the station data and model data respectively, and φ_i^{error} is the error value of the measured phase. Note that this value is unitless, and an RMS misfit of 0 would indicate a perfect match between the measured data and the model. For real data where there is noise present, the RMS misfit would ideally be in the range of 1 – 1.5. This ensures a good match between the model and the data, while preventing the noise present in the data from being fit to the model.

Removal of anomalous data points will improve the RMS misfit; however care must be taken to ensure that the data is not over-edited with the intent of matching the D+ curve, rather it should be used as a

visual aid for obtaining smoother, more realistic data curves. Thus the data is not directly fit to the D+ curve, instead the D+ curve is utilized to visually identify anomalous data points which are then manually removed. The RMS misfit values obtained from the D+ curves for each station are listed in Table 5.1.

5.8 Instrument calibrations

The Phoenix induction coils utilized for the survey contain calibration coils within their design to ensure that the recorded instrument signals are within the proper ranges for the equipment. All coils used in the survey were calibrated during the data collection, and the calibrations were utilized by both processing methods to ensure that the data recordings were correct.

5.9 Dimensionality

5.9.1 Dimensionality – Phase Tensors

As described in detail in section 4.9, the phase tensor can be utilized to determine the dimensionality of the MT data, which will determine which type of inversion is appropriate to use when converting the data into a model of subsurface resistivity. The dimensionality characterizes how the electrical resistivity varies spatially and is represented by the shape and colour of the phase tensor plots. MT data that is 1D will be plotted as uncoloured circles with beta skew of 0°, while 2D MT data is plotted as coloured ellipses with beta skew of 0°. MT data that is 3D will plot as ellipses with non-zero values of beta skew.

The phase tensor pseudosection displayed in Figure 5.6 shows the phase tensor's geographic orientation for each station plotted for each available frequency at the stations projected to a line running West-East through the survey area. In general, near the surface the phase tensors are primarily 2-dimensional as they are plotted as ellipses with low values of beta skew with a magnitude less than 2°. As frequency decreases (analogous to an increase in depth), the phase tensors start to align to a preferential direction and beta skew increases to a magnitude of 5°, signalling the presence of a conducting body and the data becomes more 3-dimensional. This is most evident in the area between Watson Lake and Highway 37 at periods greater than 3 seconds where the ellipses are mainly dark red or dark blue in colour indicating high values of beta skew of either 5° or -5° respectively. From this it can be concluded that the Watson Lake MT data set is primarily 3D and thus 3D inversion techniques must be used for modelling the resistivity.

Phase tensor plots can also be used to determine the locations of conducting bodies and to determine the strike of linear conducting features such as faults. Plots of the phase tensor in map view are shown for select frequencies with rose diagrams displaying the preferential strike orientation in Figures 5.7, 5.8, 5.9, and 5.10. Here it is seen that at the highest frequencies there is no preferential strike direction or alignment of the phase tensor plots. As the frequency decreases to between 12 and 0.08 Hz, the ellipses align to the Northwest with a preferential strike between N45°W and N30°W. This strike direction is consistent with previous studies of the Tintina Fault (Ledo et al., 2002). Note that there is a 90° ambiguity in the preferential strike direction due to the nature of the phase tensor, a Northwest strike angle was selected due to the results of previous studies on the Tintina Fault. Below 0.08 Hz, the phase tensors plotted west of 129° of longitude, and the junction at highway 37, remain aligned to the Northwest while the easternmost phase tensors change alignment. This change in alignment is indicative of crossing a conducting body (in this case, the Tintina Fault). Thus, from the phase tensor plots, it can be estimated that the Tintina Fault crosses through the centre of the survey area between Junction 37 and the Liard River, with a strike of between N45°W and N30°W.

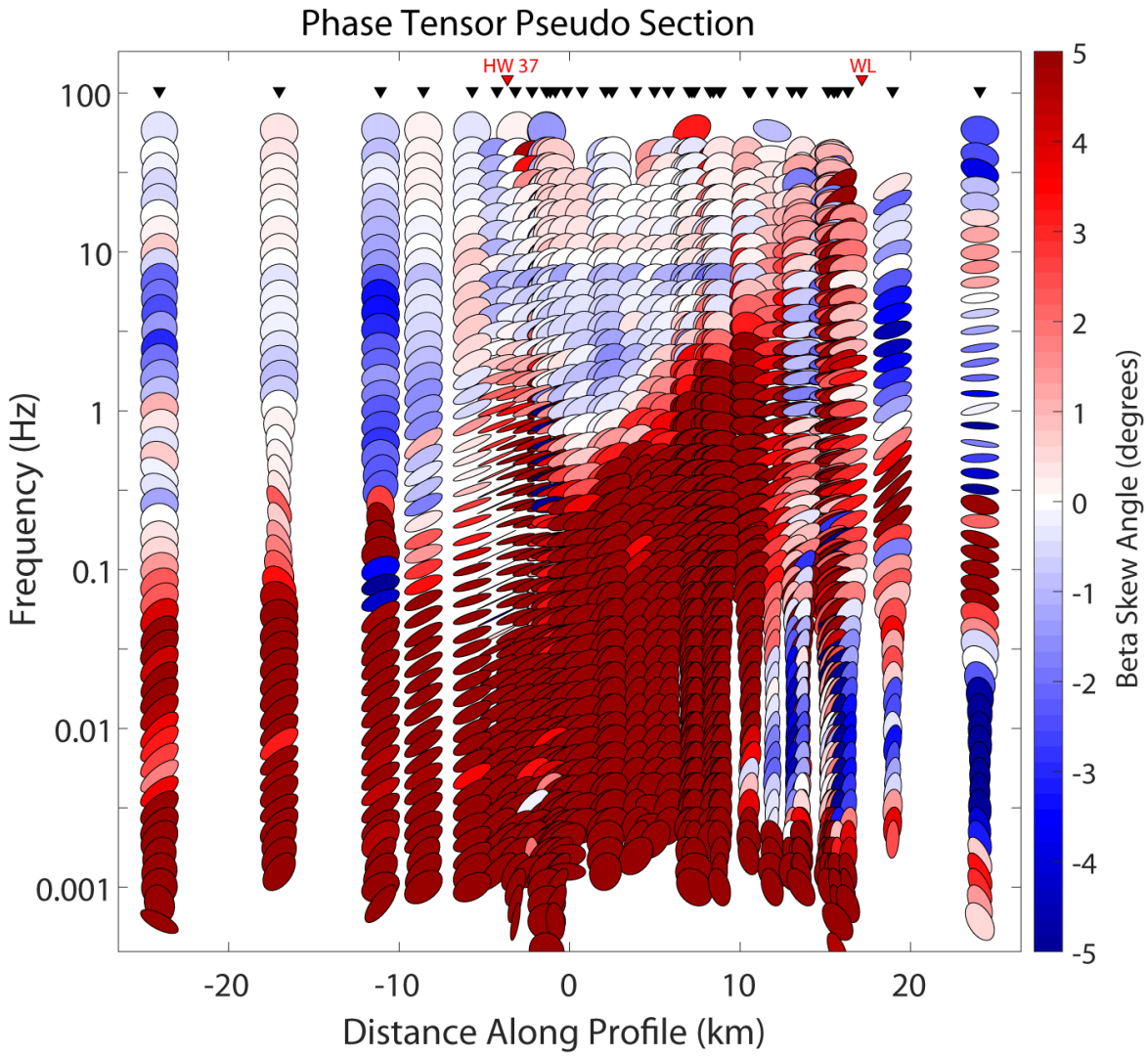

Figure 5.6: Phase tensor pseudosection for all stations projected to a line running West-East. The ellipses are coloured to represent their beta-skew angle, blue represents negative values of beta-skew, red represents positive values.

5.9.2 Dimensionality – Induction Vectors

Induction vectors are a way of plotting the vertical magnetic field components and can be used to determine dimensionality and locate conducting bodies. The components of the induction vectors are calculated as:

$$I_x = \frac{H_z}{H_x} \qquad (5.3)$$

and

$$I_y = \frac{H_z}{H_y} \qquad (5.4)$$

with real and imaginary components that can be plotted separately (Unsworth, 2019b). Depending on the convention used, the induction vectors will either point towards conductors (Parkinson convention) or away from them (Wiese convention). For a 2D MT data profile, the induction vectors will align perpendicular to the strike of a conducting feature, with the direction they point reversing after crossing the conducting feature. The real and imaginary components will plot parallel. For a 3D MT dataset, the real and imaginary induction vectors will not lie parallel to each other (Booker, 2014).

From analysis of the Parkinson induction vectors in Figures 5.7, 5.8, 5.9, and 5.10, it appears that the majority of the data can be described as 3D, which is consistent with the analysis of the phase tensor data.

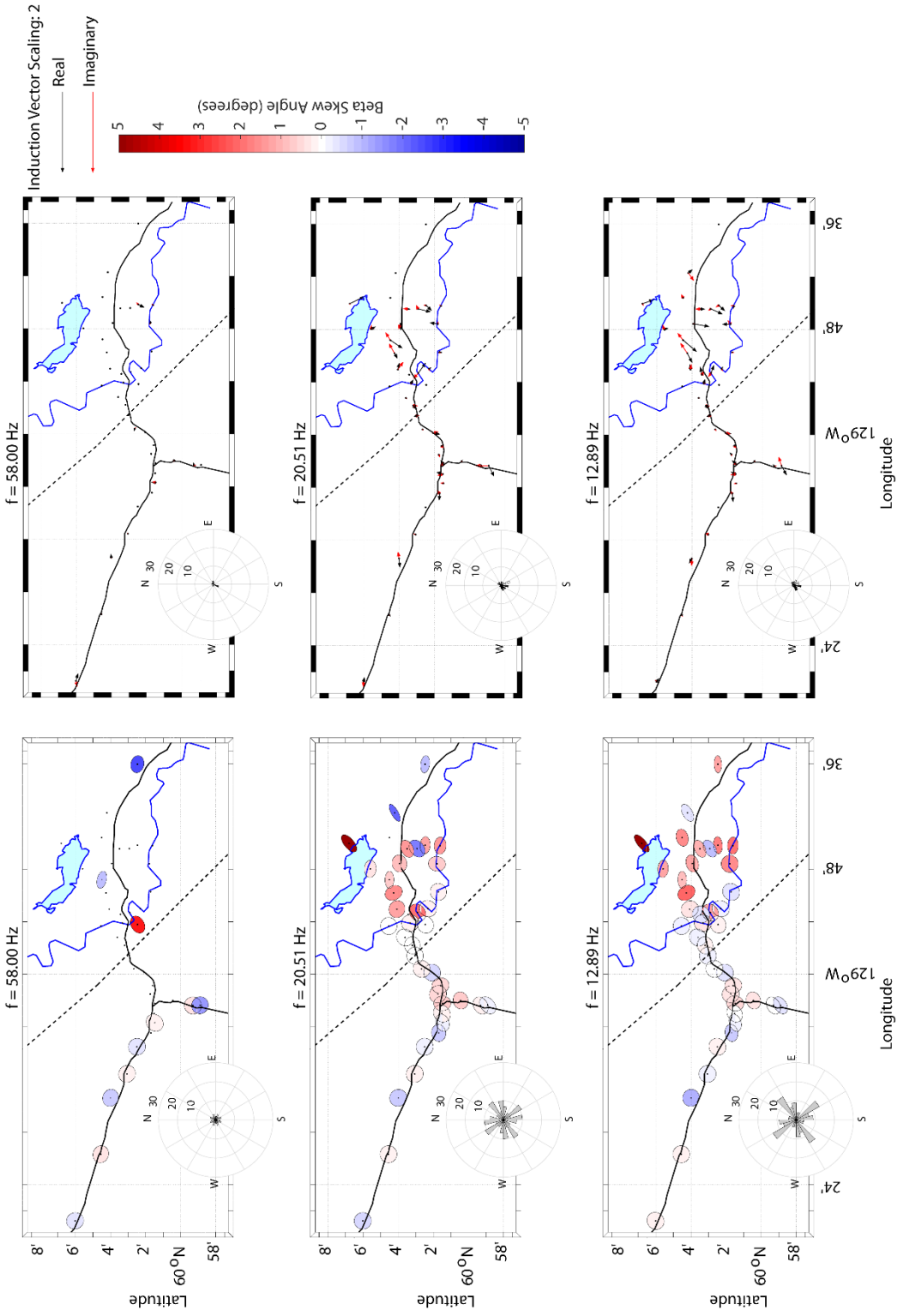

Figure 5.7: Comparison of phase tensor plots and induction vectors for select frequencies between 58 Hz and 12.89 Hz. Induction vectors are plotted using Parkinson convention. Real induction vector components are plotted as black arrows, imaginary components are plotted as red arrows. The dashed line shows the mapped Tintina Fault trace from the map of bedrock geology (Yukon Geological Survey, 2022).

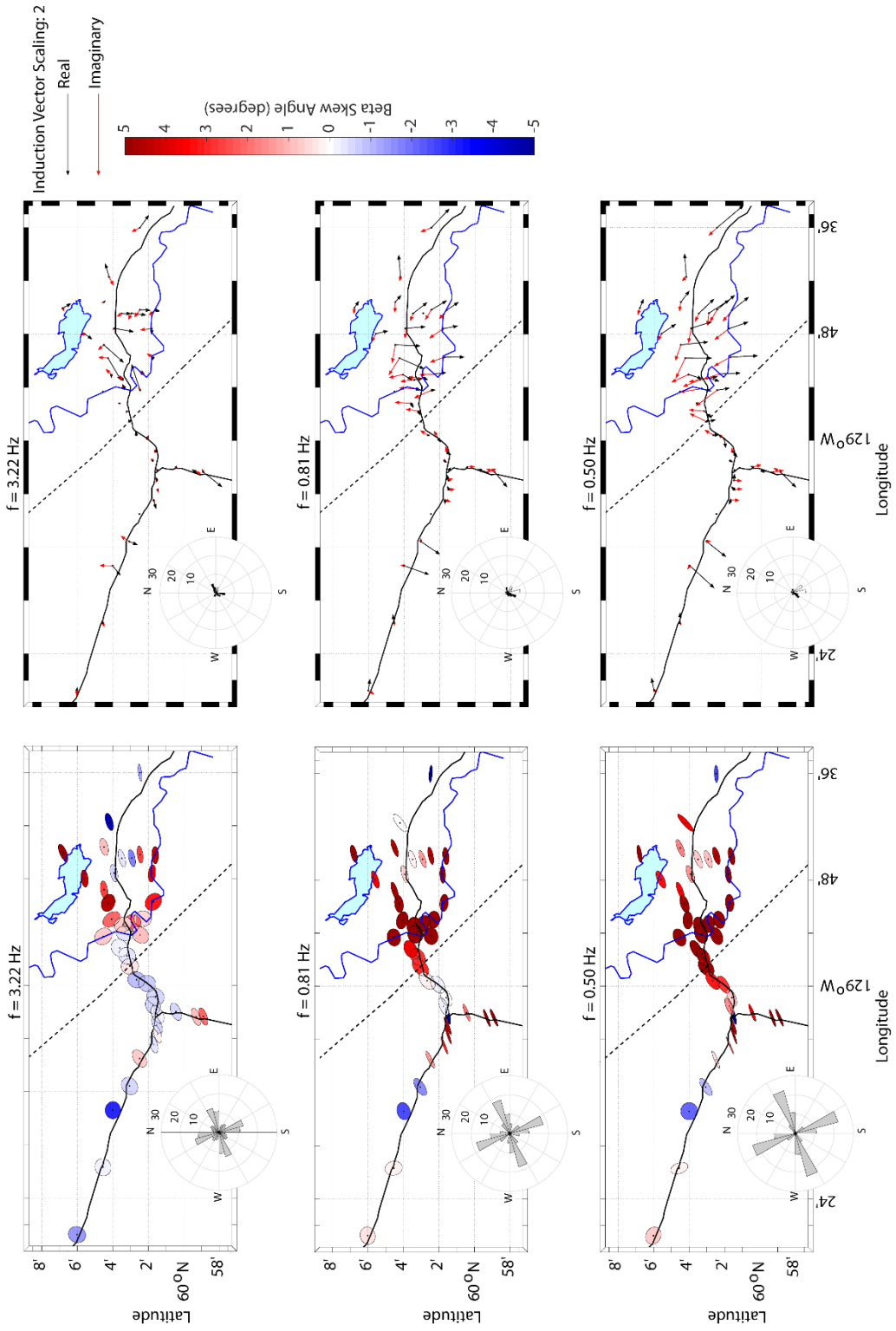

Figure 5.8: Comparison of phase tensor plots and induction vectors for select frequencies between 3.22 Hz and 0.50 Hz. Induction vectors are plotted using Parkinson convention. Real induction vector components are plotted as black arrows, imaginary components are plotted as red arrows. The dashed line shows the mapped Tintina Fault trace from the map of bedrock geology (Yukon Geological Survey, 2022).

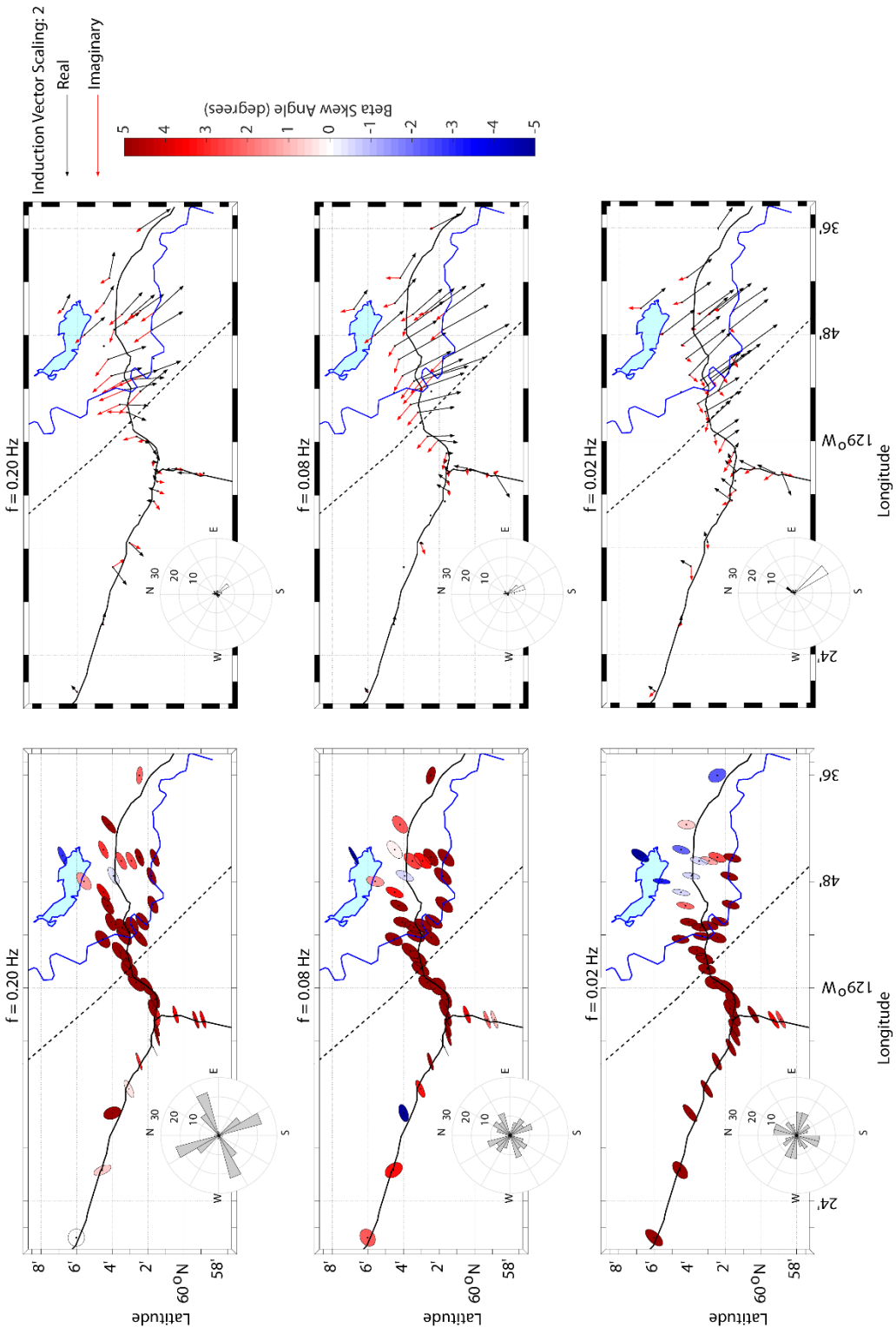

Figure 5.9: Comparison of phase tensor plots and induction vectors for select frequencies between 0.20 Hz and 0.02 Hz. Induction vectors are plotted using Parkinson convention. Real induction vector components are plotted as black arrows, imaginary components are plotted as red arrows. The dashed line shows the mapped Tintina Fault trace from the map of bedrock geology (Yukon Geological Survey, 2022).

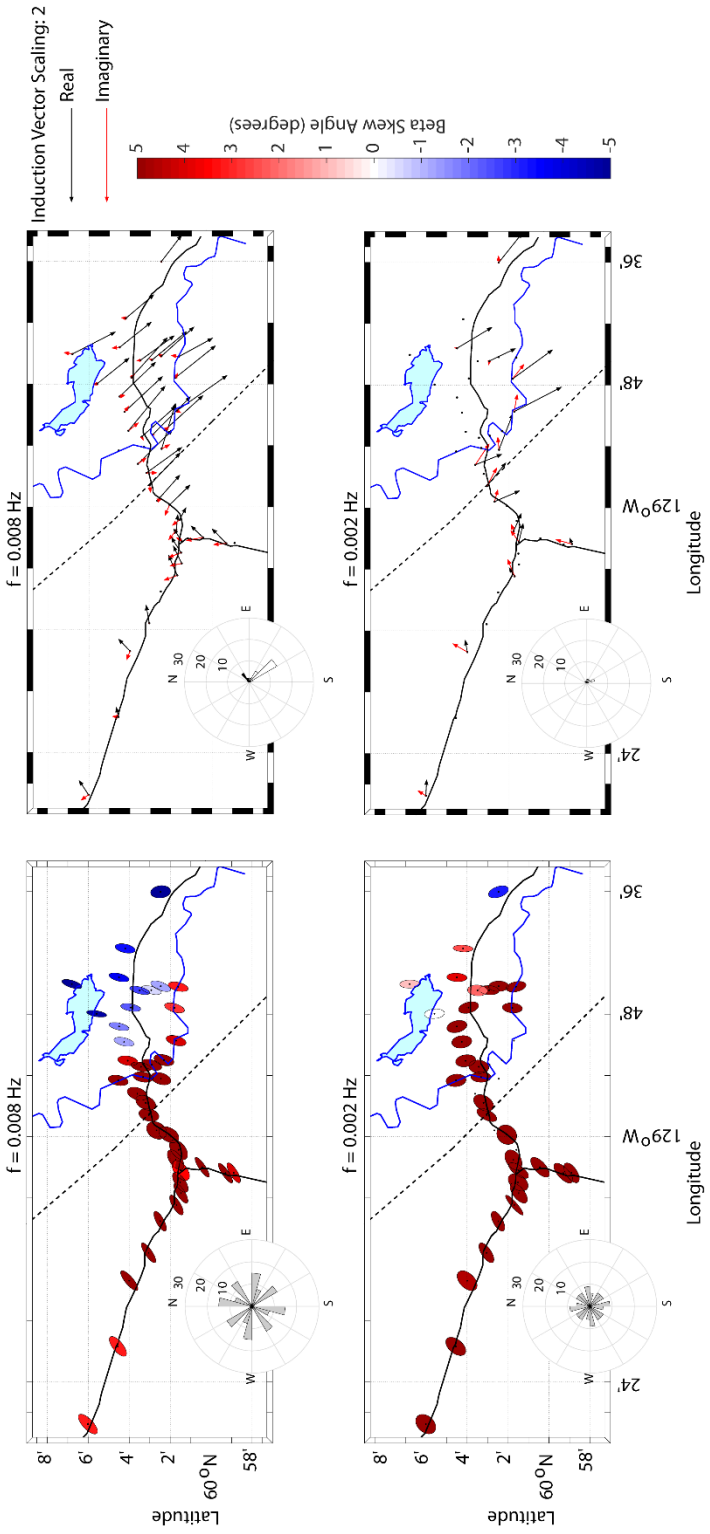

Figure 5.10: Comparison of phase tensor plots and induction vectors for select frequencies between 0.008 Hz and 0.002 Hz. Induction vectors are plotted using Parkinson convention. Real induction vector components are plotted as black arrows, imaginary components are plotted as red arrows. The dashed line shows the mapped Tintina Fault trace from the map of bedrock geology (Yukon Geological Survey, 2022).

5.10 MT Data Presented as Pseudosections

Apparent resistivity and phase pseudosections provide a way to visualize the resistivity data without performing data inversions. Apparent resistivity is plotted as a cross-section along a profile as a function of frequency. Due to the skin effect, lower frequencies travel deeper within the Earth thus plotting the pseudosection with frequency on the vertical axis is analogous to a plot of apparent resistivity with respect to depth. Tipper data can also be plotted as a pseudosection.

In the pseudosections below, all 35 collected MT stations and 5 previously collected MT stations from the SNORCLE transect are projected onto a line running from West to East along the survey area. Note that from the dimensionality analysis of the phase tensor and induction vector data, the data are primarily 3D and thus 2D pseudosections cannot separate the transverse electric (TE) and transverse magnetic (TM) modes unless the profile is parallel to the strike of the fault, ρ_{xy} and ρ_{yx} would then approximate the TE and TM modes respectively. The 2D pseudosections are also unable to correctly represent 3D features as the stations are projected onto a 2D line. The cross sections in Figures 5.11 and 5.12 show evidence of a large conducting body located between the community of Watson Lake and the junction between the Alaska Highway and Highway 37. This can also be seen in the tipper pseudosection in Figure 5.13.

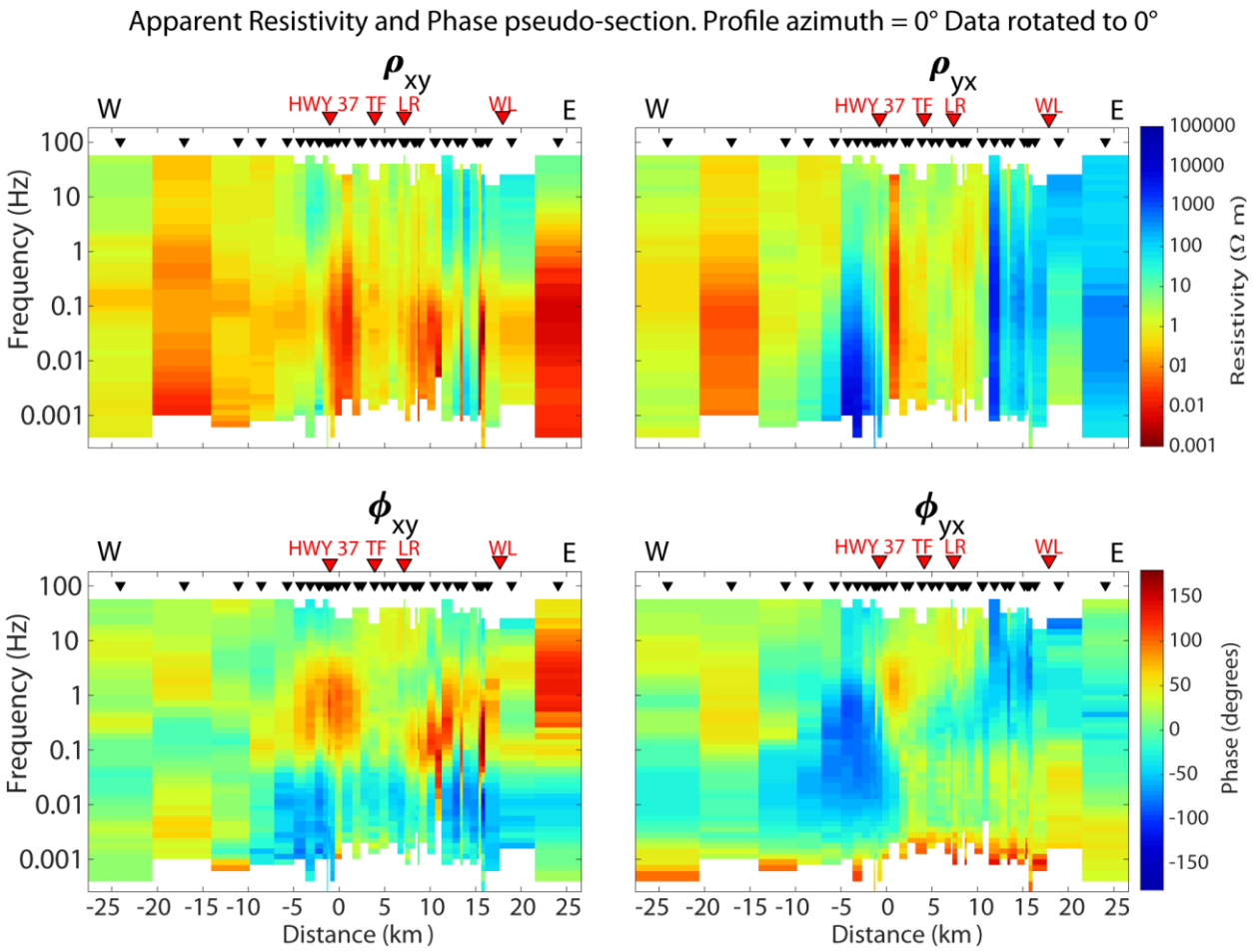

Figure 5.11: Apparent resistivity and Phase pseudosections of off-diagonal values of impedance tensor for all stations projected to a line running West-East through the survey area.

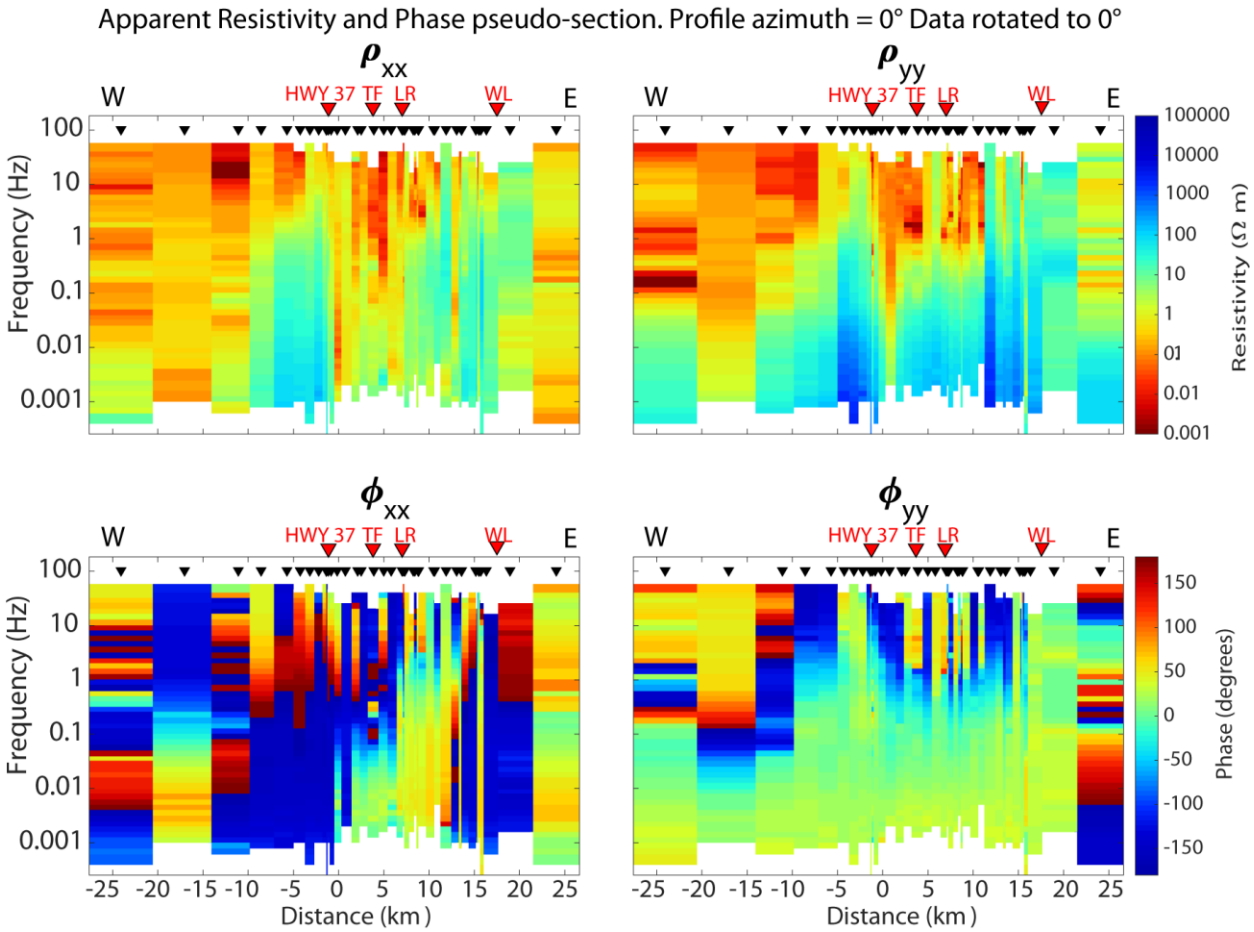

Figure 5.12: Apparent resistivity and Phase pseudosections of diagonal values of impedance tensor for all stations projected to a line running West-East through the survey area.

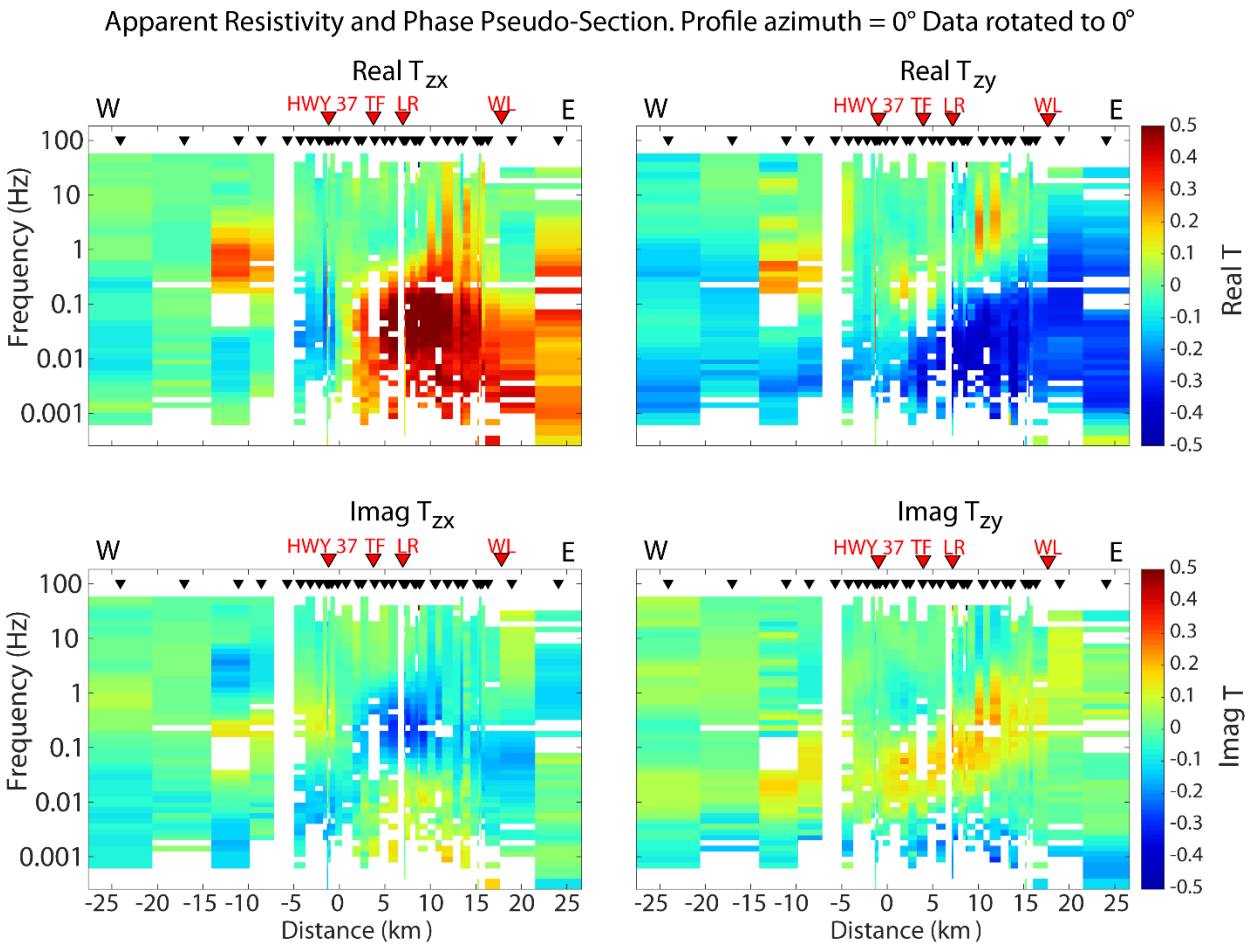

Figure 5.13: Tipper pseudosections for all stations projected to a line running West-East through the survey area.

5.11 Conclusions

The MT grid near Watson Lake was expanded from the broadly spaced SNORCLE transect to a fine-spaced 3D grid of 36 stations. Subsequent time series processing and data analysis suggests that the MT data is primarily 3D at lower frequencies, with the near-surface data displaying some 2D characteristics. Plots of the phase tensor data suggests that a linear feature is present with a strike of between N45°W and N30°W, which is consistent with previous studies of the Tintina Fault. The impedance data obtained from the time series processing can be used for data inversions, which will be used to obtain an inversion model of true resistivity as a function of depth and horizontal location. This inversion model will be crucial in identifying structures of interest for geothermal development such as clay caps or reservoirs.

Chapter 6: Magnetotelluric Data Inversions

6.1 Magnetotelluric Inversion Methods

The time-series processing described in Chapter 5 converts the time series MT data into apparent resistivity, phase, and tipper data in the frequency domain. To be interpreted further, these data need to be converted to true resistivity as a function of depth for the survey area, which requires the use of magnetotelluric inversion algorithms. Geophysical inversion is the process of utilizing observed data to create models of the physical properties of the Earth which explain the origins of those observations. In MT, the observed data is the impedance of the Earth in the measured frequency range. The algorithms use the impedance measurements to determine a model of electrical resistivity that can explain the measured impedance. This means that the magnetotelluric problem is an inverse problem, and there are an infinite number of possible resistivity models that can explain the fit a given set of measured MT data. To address this non-uniqueness, the inversion algorithms used to create the inverse models must therefore select the statistically most-likely model.

There are two main types of inversion methods that are applied to MT data: Deterministic and Stochastic. Deterministic methods rely on a defined model that is iteratively updated until a desired level of data fit is achieved. This type of inversion method usually requires less computing time than stochastic methods, but the final inversion model can be dependant on the starting model which means that the solutions are not global and may change considerably with different starting models. Stochastic methods utilize constrained random-number generation to create many possible resistivity models which find parameters that will fit the data best. Since stochastic methods generate many more models than deterministic methods, they can require much more computer resources for the MT forward calculations. Despite this, stochastic methods have the advantage that they do not rely on a starting model and thus it can be said that the solutions they generate are global rather than local and are not restricted based on the choice of starting model (Chen et al., 2012). For a 3D MT survey, it is best to use deterministic methods as they require far less computational resources.

For the inversion of the Watson Lake data, the ModEM algorithm developed by Kelbert et al., (2014) was used. This is a deterministic inversion that was run using the Cedar cluster provided by the Digital Research Alliance of Canada. The algorithm is given an initial 3D resistivity model and performs a series of iterations to create a new model that has a better fit to the measured MT data. This is done by generating forward responses of the model and comparing the real and generated data via the root mean-squared (RMS) misfit. If the generated model does not satisfy the stopping conditions set by the

control file, then the algorithm uses the generated model to start a new iteration. This repeats until one of the stopping conditions is satisfied. These stopping conditions include the model smoothness, the final RMS misfit, the number of iterations, and the total computing time used by the inversion. Typically, the inversions finished when the RMS misfit could not be improved. If an inversion finished due to reaching the maximum number of iterations set, or if the inversion used all the allotted computing time without meeting any other stopping conditions, it was then restarted from the final iteration until another stopping condition was met. Inversions would usually take approximately three to five days to run on the cluster and almost all inversions were completed before 200 iterations were completed.

6.2 Initial ModEM Inversion of Watson Lake MT Data

6.2.1 Inversion Starting Model

For each inversion, a starting model must be constructed to begin the inversion. For the preferred inversion the initial model consisted of a 100 Ωm halfspace constructed of a mesh of cells. The cells were initially 500 m x 500 m horizontally and increased in size geometrically by a factor of 1.3 further from the centre of the survey area. This created padding cells surrounding the main survey area which serve to reduce edge effects experienced by cells located on the edges of the mesh. This ensures that no resistivity values for cells within the main survey area were influenced by the edge effects. Topography was also included in the inversions, with a vertical air cell size of 50 m, which increased geometrically by a factor of 1.1 for cells below the surface of the Earth. Air cells were assigned very high values of electrical resistivity to ensure they did not affect the rest of the inversion model. The entire model had a size of 72 x 140 x 77 cells. This starting model was selected by testing the minimum required cell size and geometric padding factor needed to minimize edge effects. It is important to have a model mesh large enough to reduce these effects, but not so large that it will affect the computational requirements of the inversion.

6.2.2 Inversion Parameters

The inversion (watson_lake_inv13 in Table 6.1) used impedance data from 24 frequencies in the range of 0.001 – 100 Hz. The frequencies were selected by determining the maximum and minimum frequency range available for all stations and selecting every other frequency. This was done to reduce the number of frequencies used in the MT inversion (effectively reducing computing time), while still retaining

enough data to define the overall data trend for each station. Error floors of 5% for all components of the impedance tensor were also utilized for this inversion. This determines the minimum error of the predicted data points generated by the model, and thus controls how well data generated by the inversion model is expected to agree with the true MT data. Inversions with higher error floors will be easier to fit and thus have lower values of RMS misfit.

The initial RMS misfit of the starting model was 12.62. This improved to a value of 1.89 after 136 iterations of the model had been generated, after which the ModEM algorithm was unable to improve the RMS misfit further and the inversion was completed. This is an acceptable value of RMS misfit, as it is low enough to accurately model the data, but not so low as to overfit noise in the data. The apparent resistivity and phase pseudosections below (Figures 6.1 and 6.2) show that the inversion model fits the data well.

6.2.3 Initial MT Inversion Model Results

The inversion model is displayed in Figures 6.3 and 6.4 below. There are four key areas of interest in the model: two conductive bodies (C1 and C2) and two resistive features (R1 and R2). Conductor C1 has an electrical resistivity ranging between 1 – 10 Ωm. It is located a depth of approximately 500 m below sea level (b.s.l.) and extends to a maximum depth of 3 km b.s.l. It is located between the Liard River and the junction of the Alaska Highway and Highway 37 with a width of approximately 15 km and is bounded on either side by the resistive features R1 to the West and R2 to the East. Conductor C2 is also located at a depth of 500 m b.s.l., but appears to extend much deeper to a depth of approximately 10 km b.s.l. The true extent of its depth is poorly constrained due to the lack of station data near the conductor, limiting the resolution of the model at this point. C2 has a resistivity range of 10 – 30 Ωm, and a width of 3 km. It is separated from C1 by the resistor R2.

Both resistors R1 and R2 have similar resistivity values in the range 300 – 1000 Ωm. R1 has a width of 10 km and a extends to a depth below what can be resolved by the inversion model. The feature appears near vertical with a slight eastward dip. Resistor R2 dips westward, with a width of 6 km. It is possible that the resistive features are both a part of a larger resistive structure within which conductor C1 is embedded, but this cannot be constrained by the inversion model. Further interpretations of the causes of these features are described in Chapter 7.

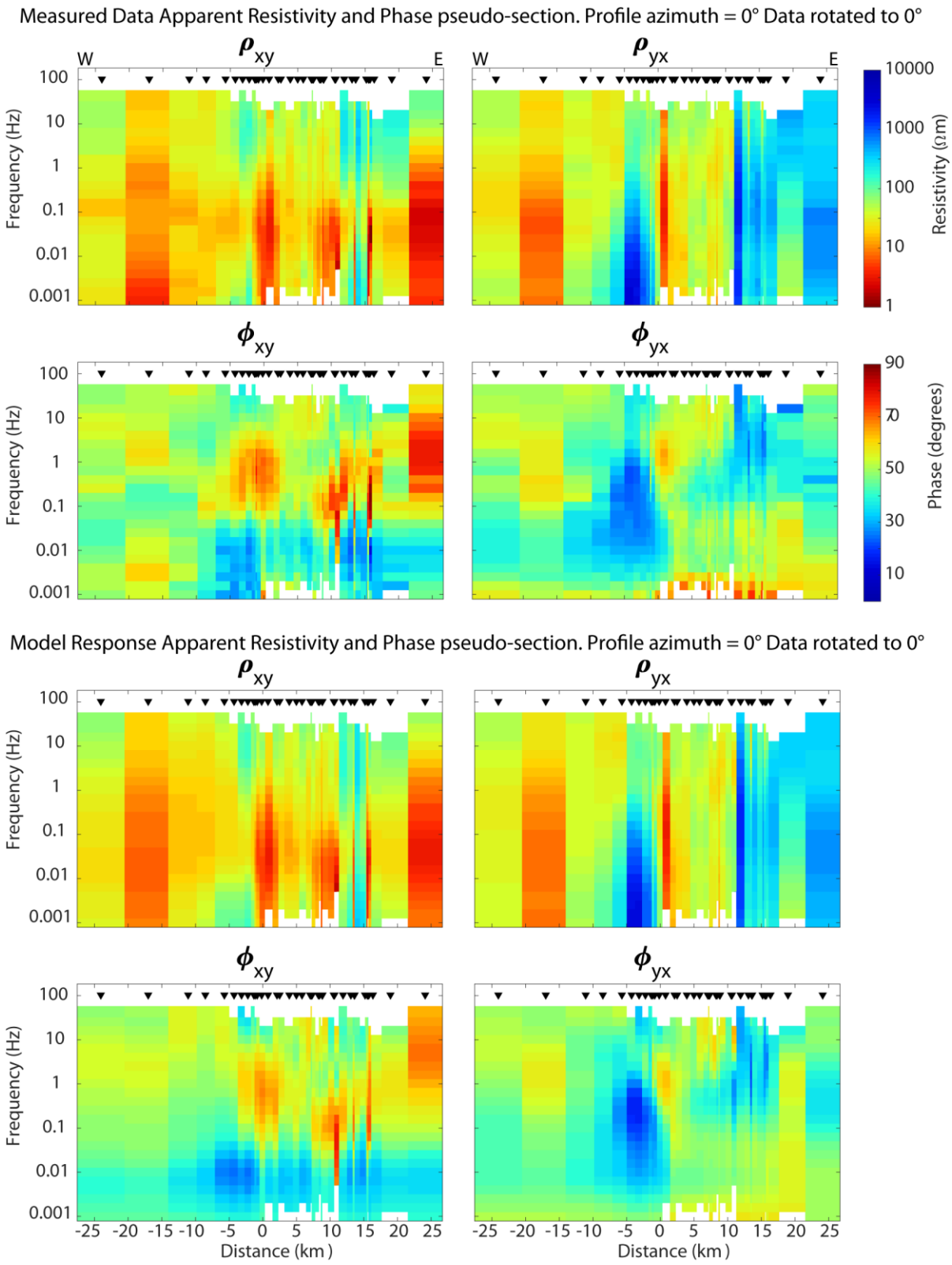

Figure 6.1: Apparent resistivity and phase pseudosections for the off- diagonal components of the impedance tensor comparing the real data (top 4 panels) and the inversion watson_lake_inv13 (bottom 4 panels).

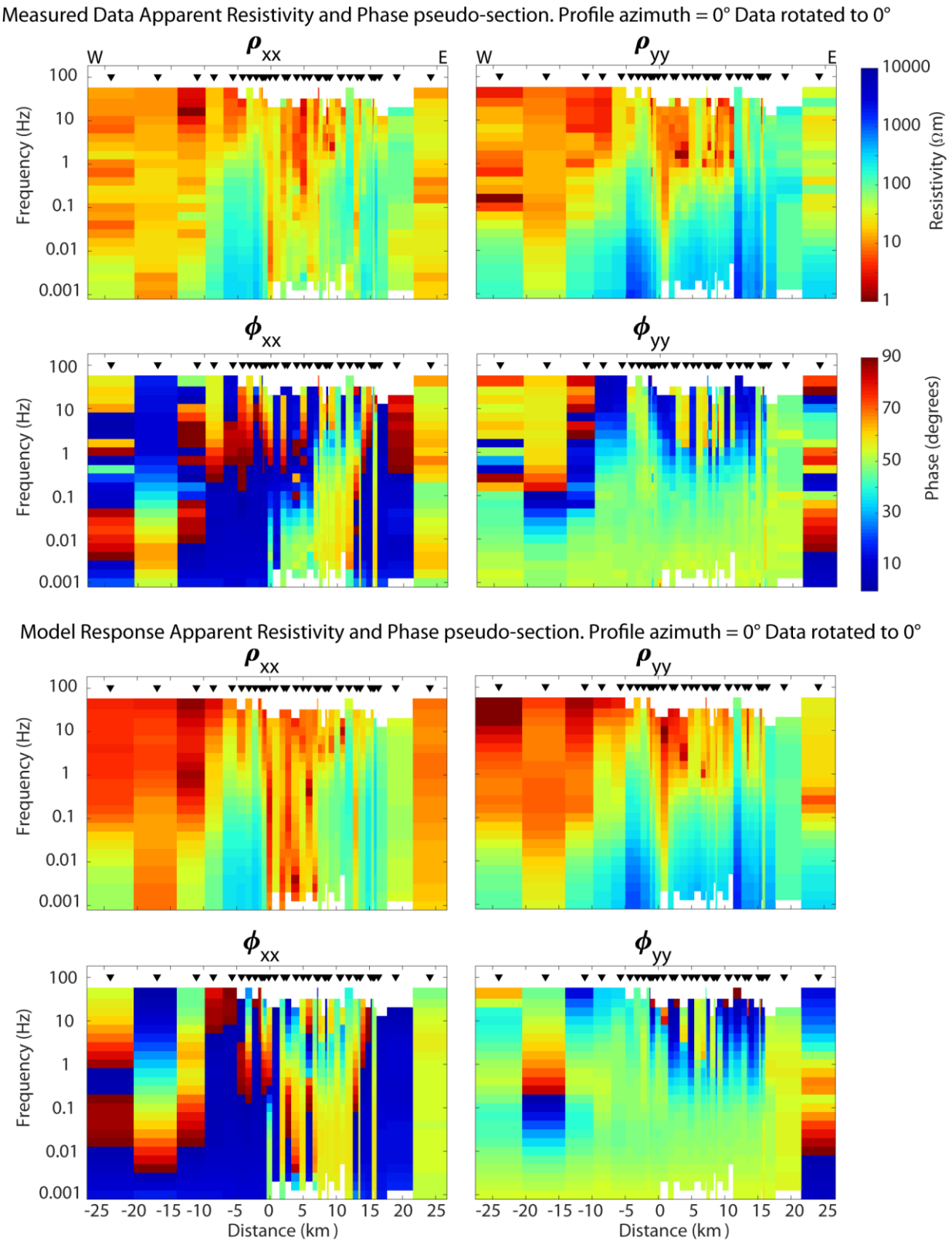

Figure 6.2: Apparent resistivity and phase pseudosections for diagonal components of the impedance tensor comparing the real data (top 4 panels) and the inversion watson_lake_inv13 (bottom 4 panels).

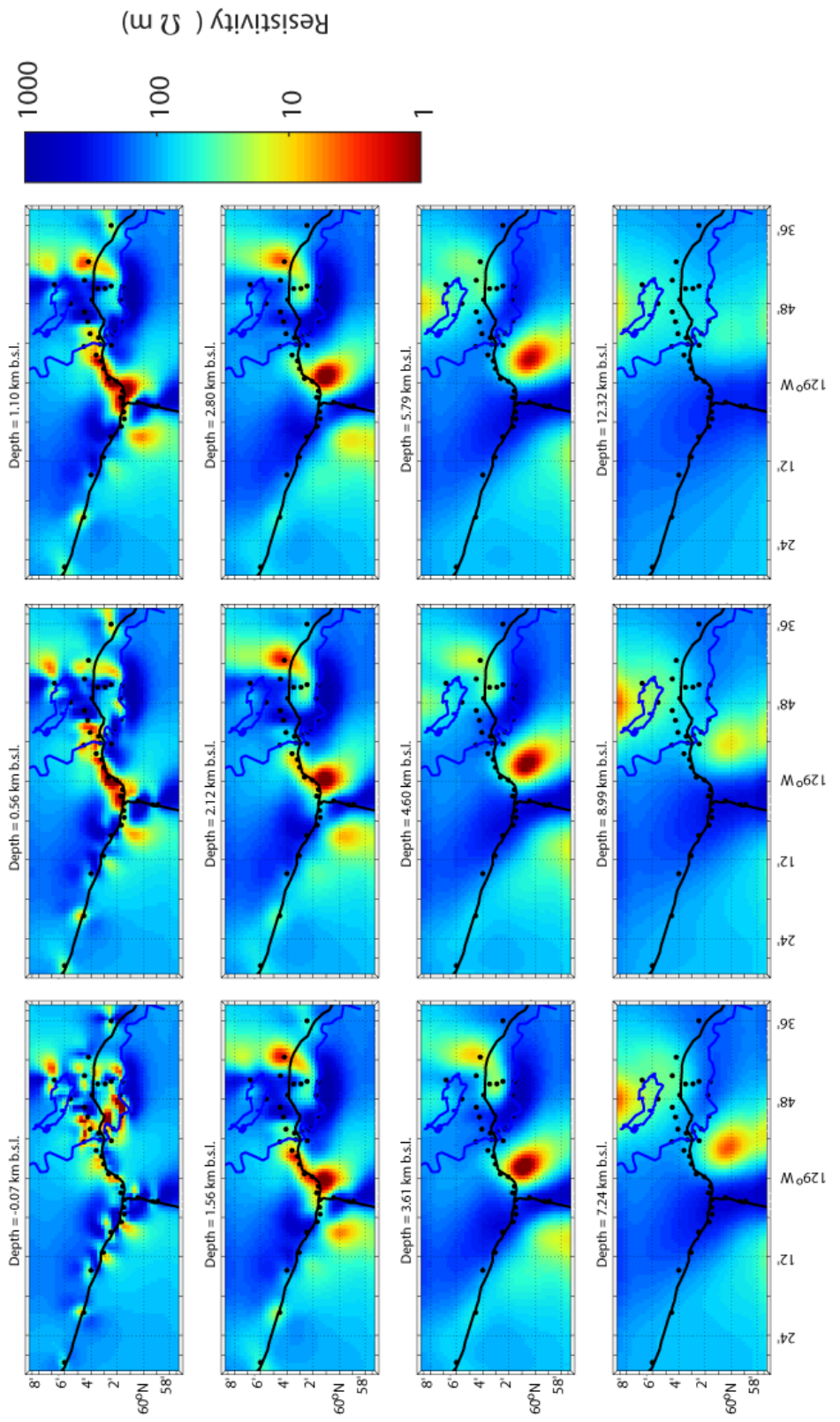

Figure 6.3: Horizontal cross-sections at select depths for the resistivity model results for inversion watson_lake_inv13. The black lines represent highways, and the blue lines outline the Liard River and Watson Lake.

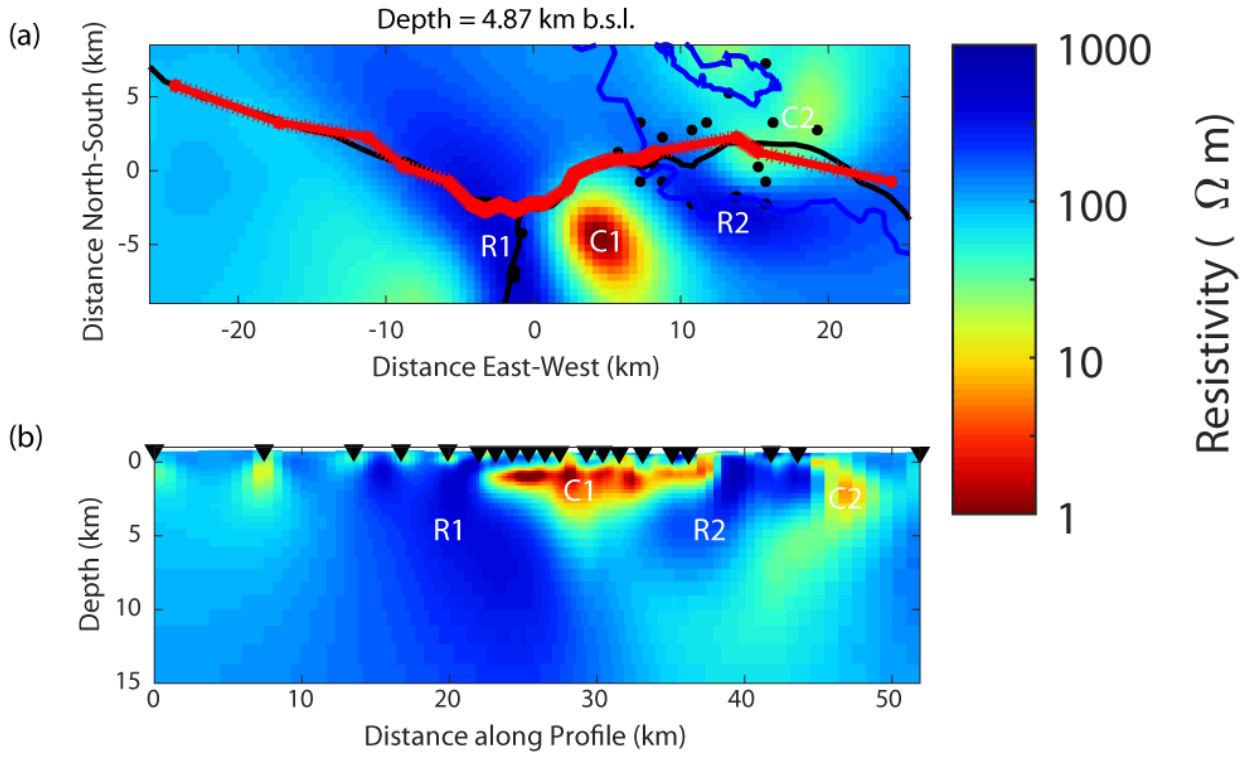

Figure 6.4: (a) horizontal and (b) vertical cross-section of watson_lake_inv13 taken from a profile of stations along the Alaska Highway (red line). The conducting features of the model are labelled as C1 and C2. The resistive features are labelled as R1 and R2

6.3 Range of ModEM Inversions

A variety of ModEM inversions with different starting models, error floors, data types, and data rotations were utilized to better constrain the features identified, and to look for variations between the different inversion models. This is done to address the non-uniqueness of the MT inversions, since if a feature appears in multiple inversion models it is more likely to be necessary to best fit the data. Details of the various inversions are listed in Table 6.1.

Inversion Name	watson_lake_inv1	watson_lake_inv2	watson_lake_inv3	watson_lake_inv6*	watson_lake_inv13	watson_lake_inv21	watson_lake_inv22	watson_lake_inv23	watson_lake_inv24	watson_lake_inv25
Number of Stations	35	35	40	40	40	40	38	40	40	40
Minimum Period (s)	0.01	0.01	0.01	0.01	0.01	0.01	0.01	0.01	0.01	0.01
Maximum Period (s)	1000	1000	1000	1000	1000	1000	1000	1000	1000	1000
Number of Frequencies	24	24	24	24	24	24	24	24	24	24
Error Floor (Z)	10%	10%	10%	10%	5%	5%	n/a	10%	5%	5%
Error Floor (T)	n/a	n/a	n/a	n/a	n/a	0.02	0.02	n/a	n/a	n/a
Rotation Angle (°)	0	0	0	0	0	0	0	-30	0	0
Starting Model Resistivity (Ωm)	100	100	100	100	100	100	100	100	10	30
Data Inverted	Z	Z	Z	Z	Z	Z + T	T	Z	Z	Z
X-Cells	54	54	56	56	72	72	72	72	72	72
Y-Cells	100	100	124	124	140	140	140	140	140	140
Z-Cells	45	85	45	45	77	77	77	77	77	77
Total Cells	243000	459000	312480	312480	776160	776160	776160	776160	776160	776160
RMS Misfit Start	6.50	6.60	6.40	6.36	12.62	11.42	7.94	6.66	10.74	9.92
RMS Misfit End	1.12	3.46	1.17	1.04	1.89	2.19	1.44	1.04	1.60	1.78
Total Iterations	163	70	150	101	136	203	168	108	195	131

*Table 6.1: List of parameters for select ModEM inversions of the Watson Lake MT data. For Data Inverted; Z=impedance, T=tipper. *watson_lake_inv6 was an anisotropic inversion where separate models for ρ_x, ρ_y, and ρ_z were calculated independently.*

Several inversions with different starting models were attempted. These include starting models with resistivities of 10 Ωm and 30 Ωm and models without topography. It was found that changing the resistivity of the halfspace had no discernable effect on the final inversion model. Likewise, inversions without topography had little difference compared to inversions that included topography. This is likely due to the subdued topography of the study area, with station elevations ranging from approximately 598 – 829 m above sea level.

6.3.1 Rotating the Data and Inversion Model

Tietze and Ritter (2013), showed that 2D structures within a 3D resistivity model may not be fully resolved unless the coordinate system used for the data and model are rotated to align with the regional strike of the study area. Based on this, an inversion with a rotation was tested to check for differences in the final inversion model. From the phase tensor analysis (section 5.9.1), it was determined that the regional strike was approximately N30°W, and thus a -30° rotation was applied to the inversion. The inversion utilized the same starting model and parameters as the preferred inversion and utilized error floors of 10%. It ran for 108 total iterations with an initial RMS misfit of 6.66 in the first iteration and final RMS misfit of 1.04. The results shown in Figures 6.5 to 6.8 are very similar to the results of the initial inversion in 6.2. The vertical cross-section in Figure 6.8 is nearly identical to Figure 6.4, the only major difference is the western extent of the conducting region, which does not extend as far in the rotated inversion. The smaller conducting region is also shifted slightly east compared to the previous inversion and does not appear to extend as deep. In the horizontal cross-sections displayed in Figure 6.7, the shape of the conducting bodies at each depth are very similar to the previous inversion but appear slightly shifted in location to the Southwest of the study area. Overall, the rotation of the data and grid does not appear to have resolved any structures or features that were not present in the initial inversion.

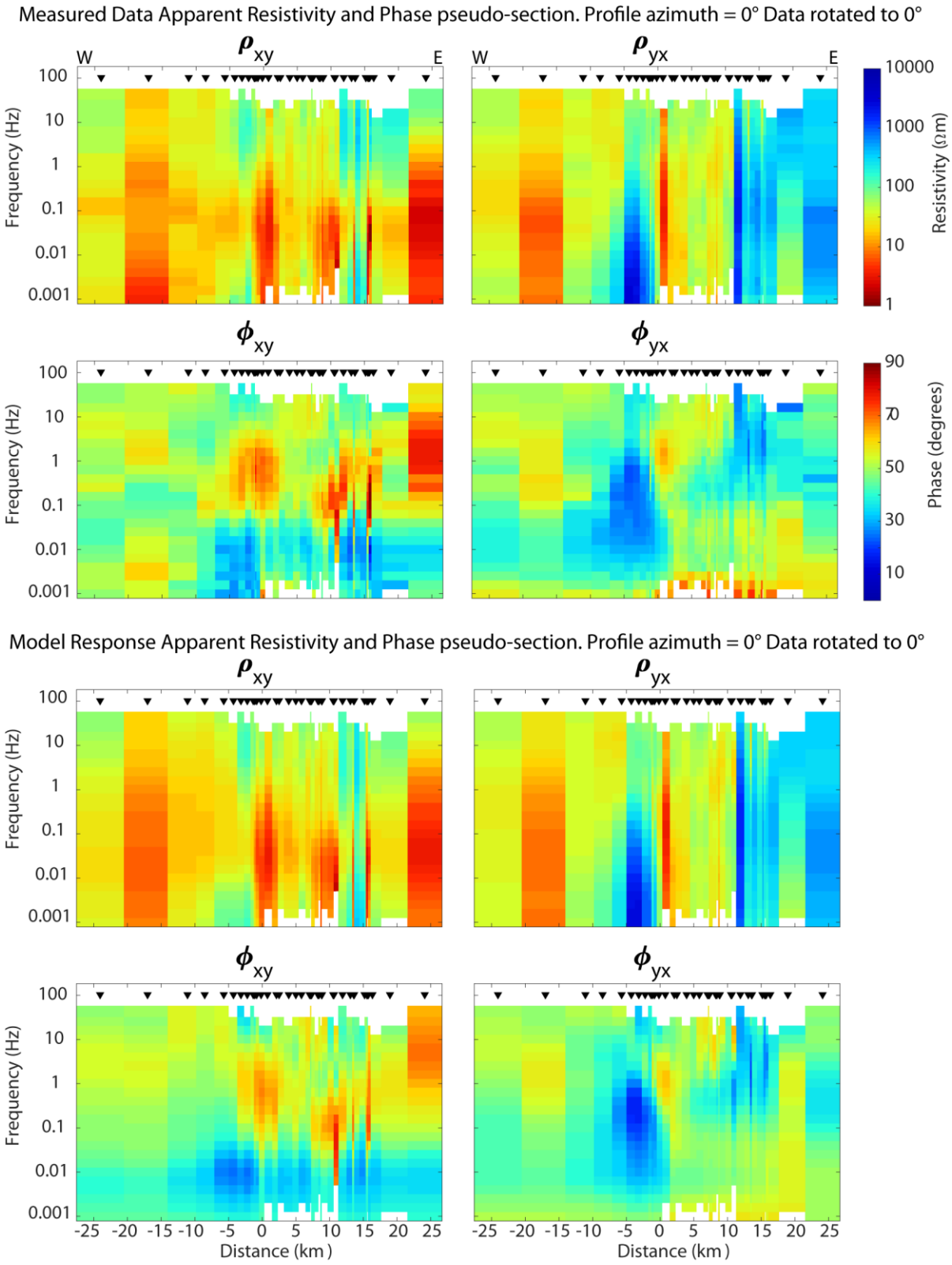

Figure 6.5: Apparent resistivity and phase pseudosections for the off-diagonal components of the impedance tensor comparing the real data (top 4 panels) and the inversion watson_lake_inv23 (bottom 4 panels).

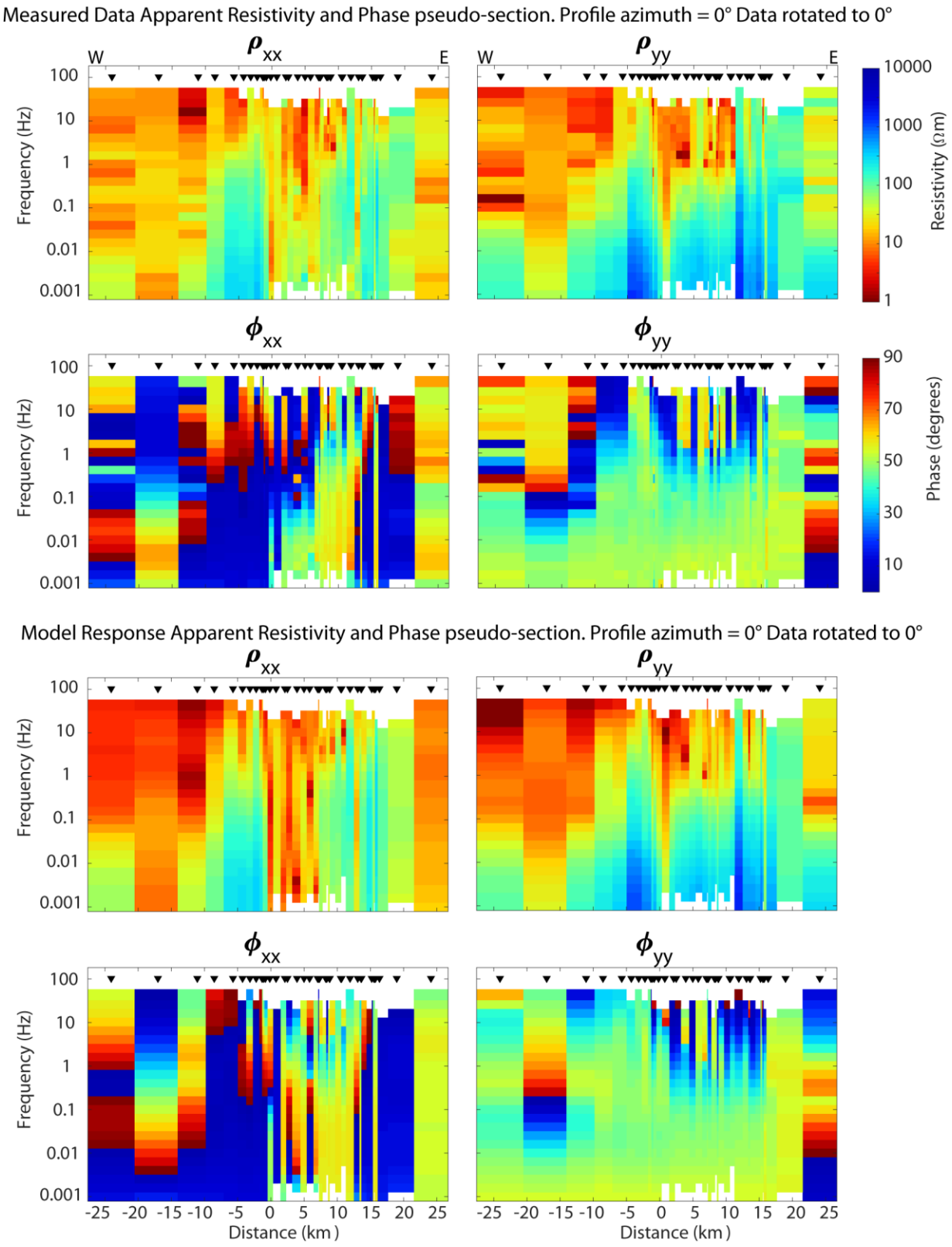

Figure 6.6: Apparent resistivity and phase pseudosections for diagonal components of the impedance tensor comparing the real data (top 4 panels) and the inversion watson_lake_inv23 (bottom 4 panels).

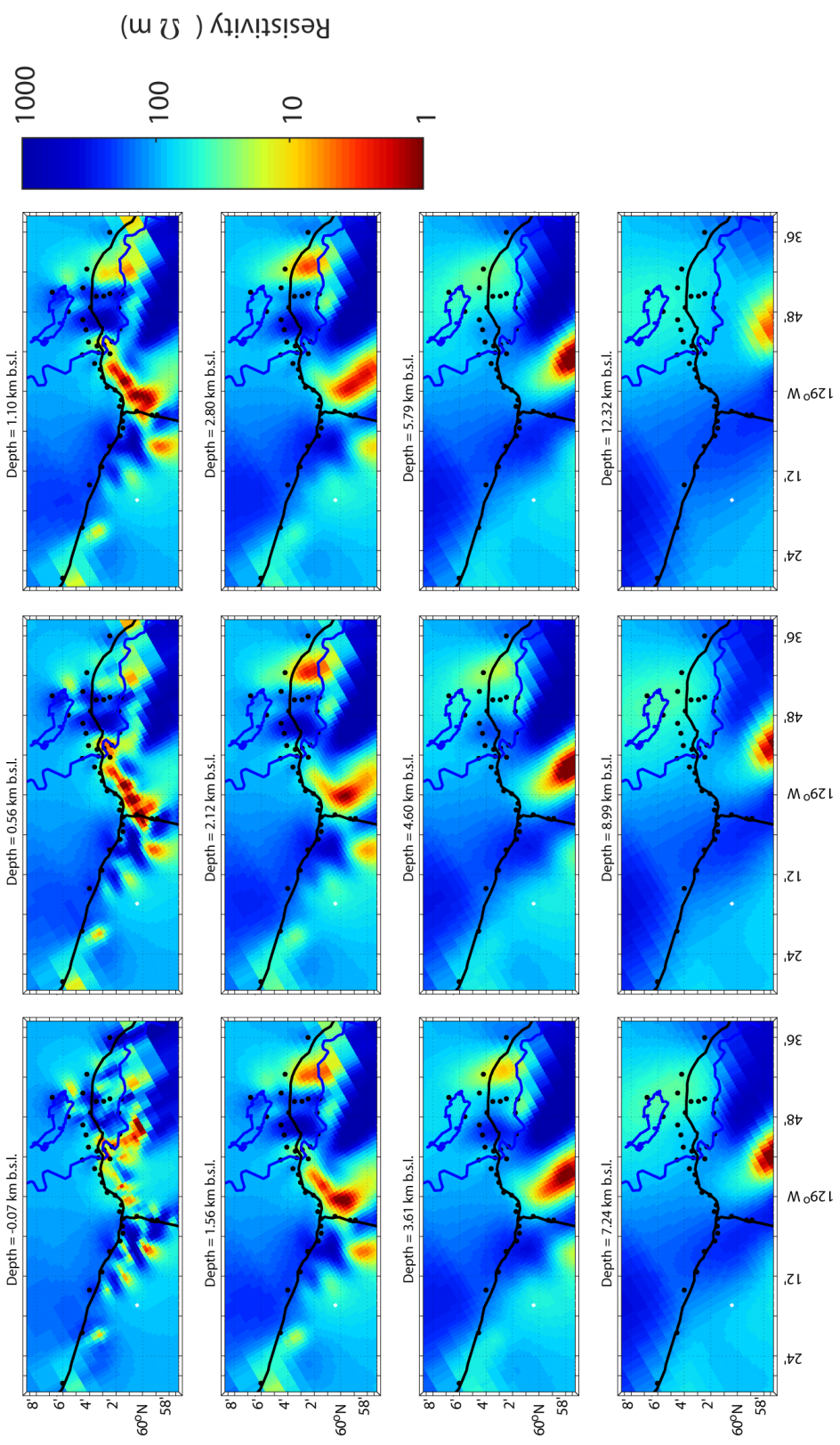

Figure 6.7: Horizontal cross-sections at select depths for the resistivity model results for inversion watson_lake_inv23. The black lines represent highways, and the blue lines outline the Liard River and Watson Lake.

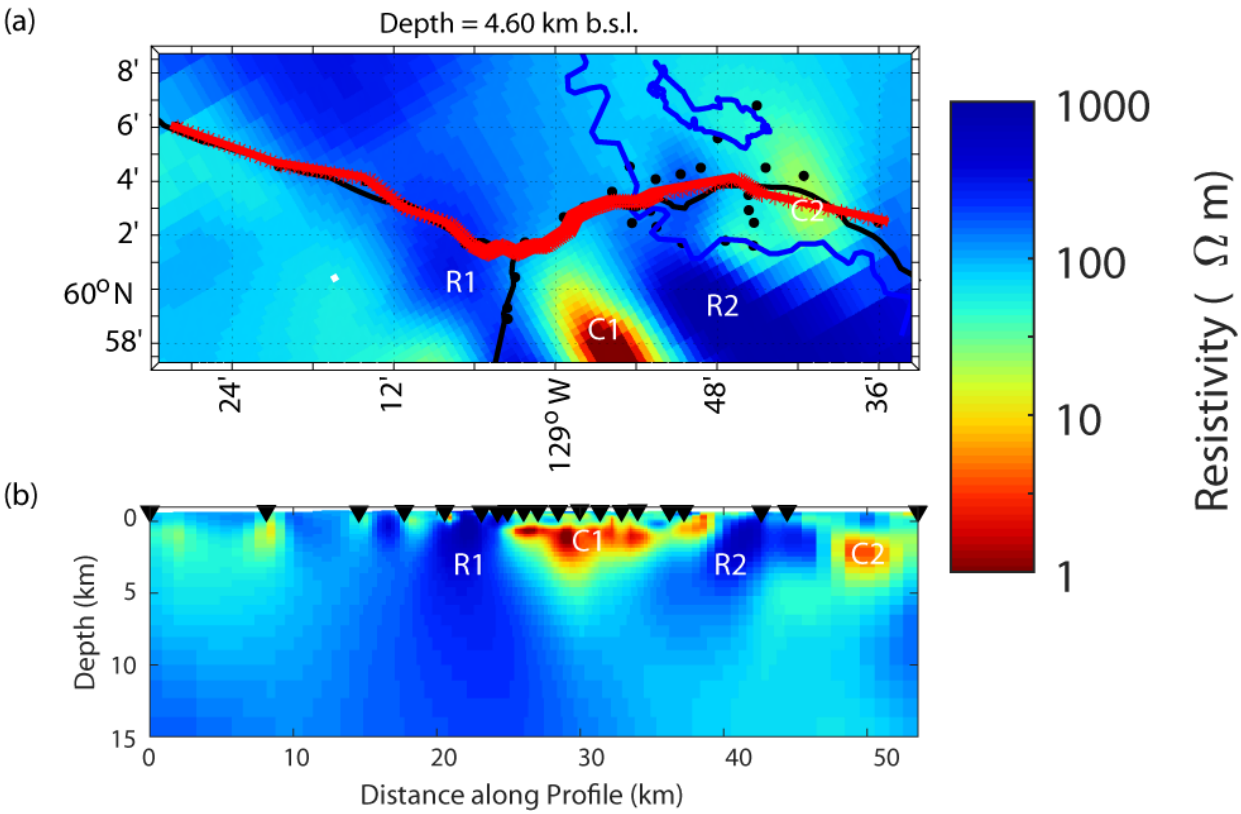

Figure 6.8: (a) horizontal and (b) vertical cross-sections of watson_lake_inv23 taken from a profile of stations along the Alaska Highway (red line). The conducting features of the model are labelled as C1 and C2. The resistive features are labelled as R1 and R2.

6.3.2 Impedance Tensor and Tipper Inversion

The tipper data (Section 4.2.8) can be used in addition to the impedance tensor data for inversions. Since the tipper tends to be sensitive to areas with horizontal variations in resistivity, it can be useful for resolving and constraining potential conducting bodies in the inversion model. An inversion using both the tipper and impedance tensor data was also tested. This inversion utilized the same starting model from 6.2.1, and error floors of 5% for impedance data and 0.02 for the tipper data. The inversion ran for a total of 203 iterations with the RMS misfit improving from an initial 11.42 in the first iteration to 2.19 in the final iteration. The result can be seen in Figures 6.9 to 6.13 below. The vertical cross-section of the final resistivity model in Figure 6.13 shows similar areas of low resistivity as seen in the previous inversions but with the large, central conducting thinning considerably in the Eastern portion. The smaller, eastern conductor now extends much deeper than in the previous inversions and has a lower resistivity range of 1 – 10 Ωm. The horizontal cross-sections (Figure 6.12) still display the large central conductor, however there are also many smaller conductors not seen in the previous inversions. These

are poorly constrained and appear near the edges of the study area where station data was not collected.

6.4 Synthetic Inversions and Sensitivity Tests

Synthetic inversions were also tested in order to determine the resolution of the collected data. In order to perform a synthetic inversion, a 100 Ωm halfspace as constructed with the same geometry as the starting model for the data inversions. This model was then edited in order to insert various different conducting bodies such as conducting layers, prisms, and linear fault-like features. The ModEM algorithm was then used to generate forward responses of the synthetic models. The forward responses then had synthetic noise added and the data were inverted in the same way as the real data inversions using ModEM on the Cedar cluster. These tests provide a way of determining the resolution of the collected data, especially in areas where no stations are present. Table 6.2 lists the parameters for the synthetic inversion.

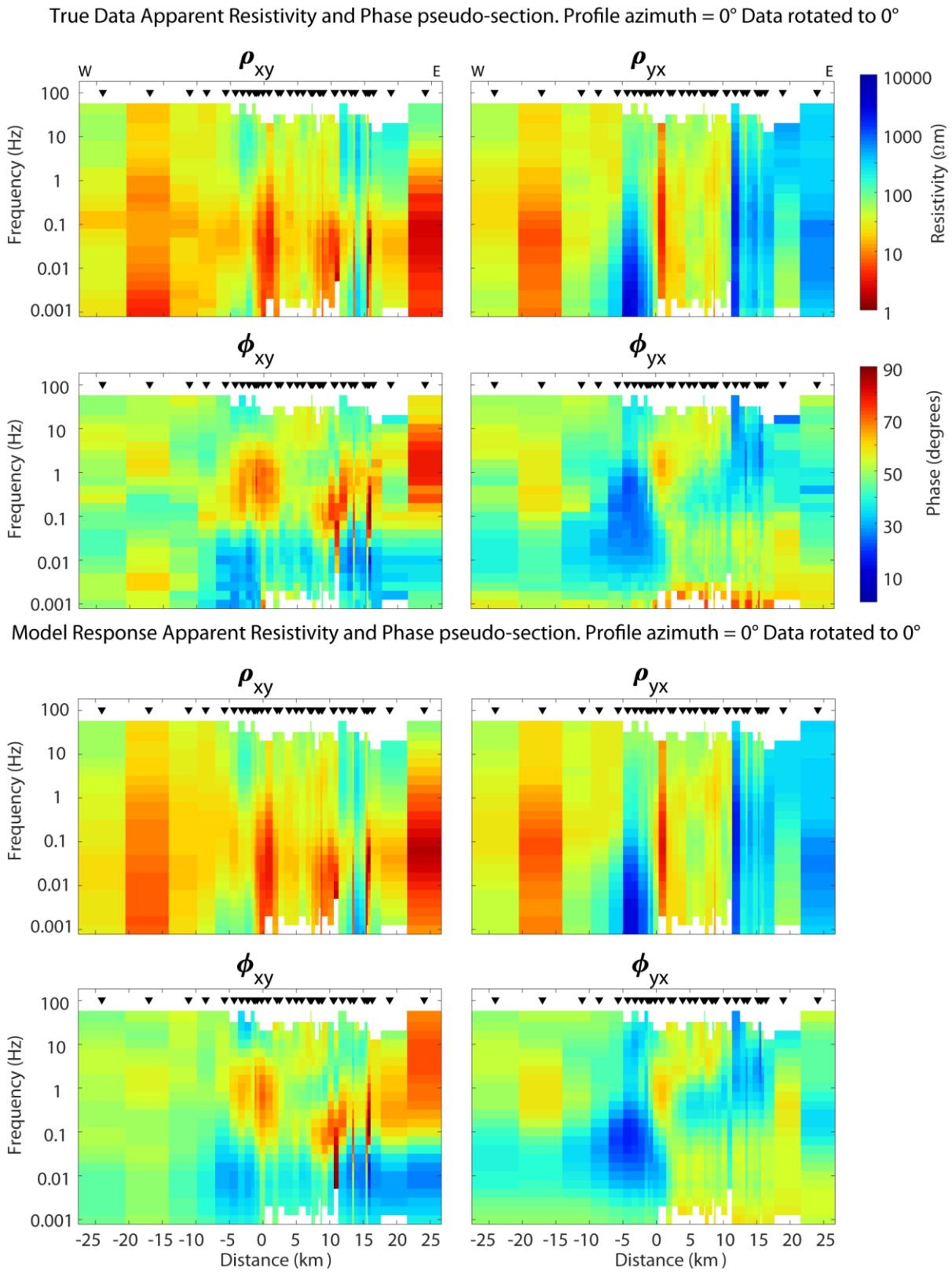

Figure 6.9: Apparent resistivity and phase pseudosections for the off-diagonal components of the impedance tensor comparing the real data (top 4 panels) and the inversion watson_lake_inv21 (bottom 4 panels).

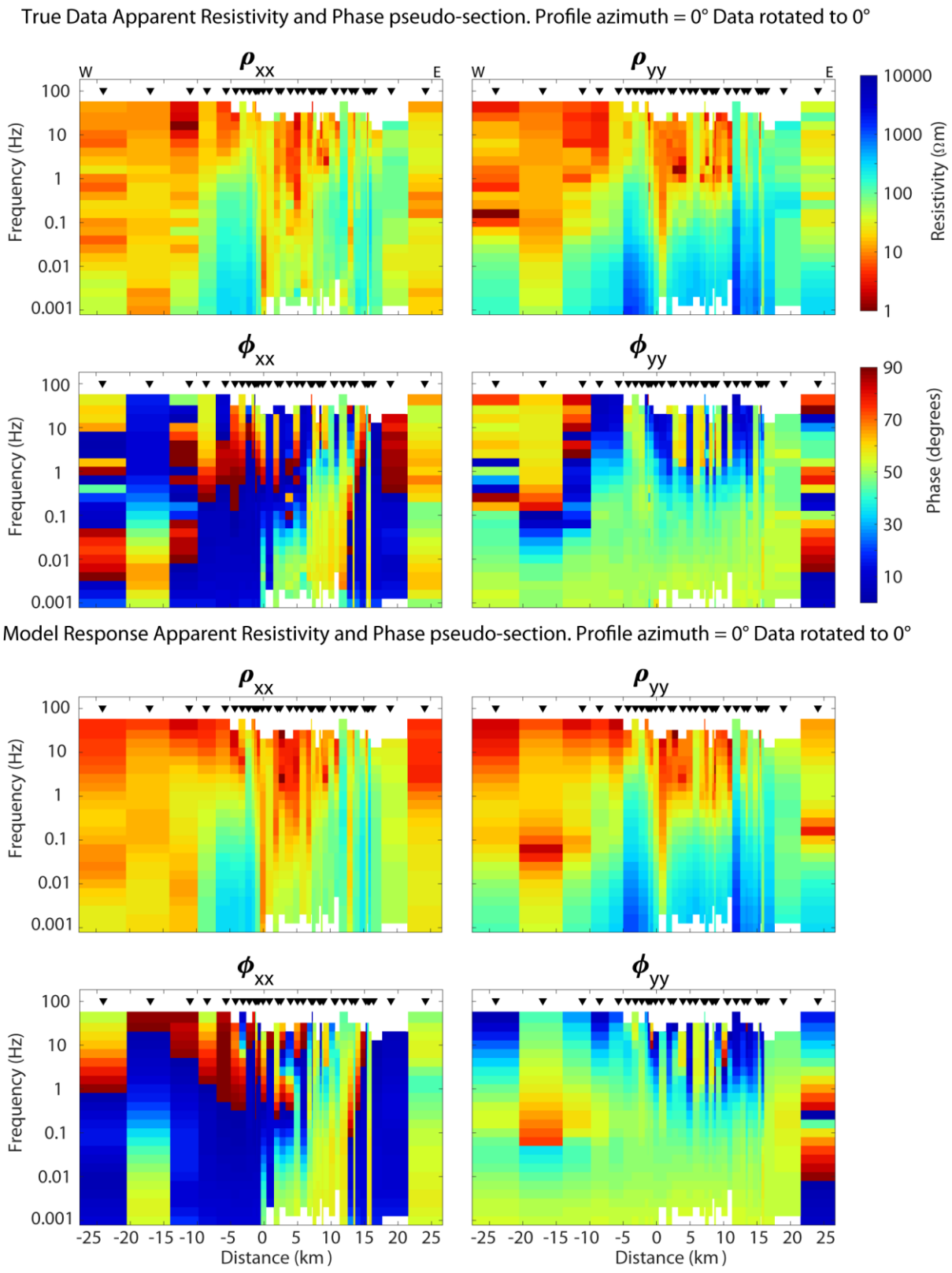

Figure 6.10: Apparent resistivity and phase pseudosections for diagonal components of the impedance tensor comparing the real data (top 4 panels) and the inversion watson_lake_inv21 (bottom 4 panels).

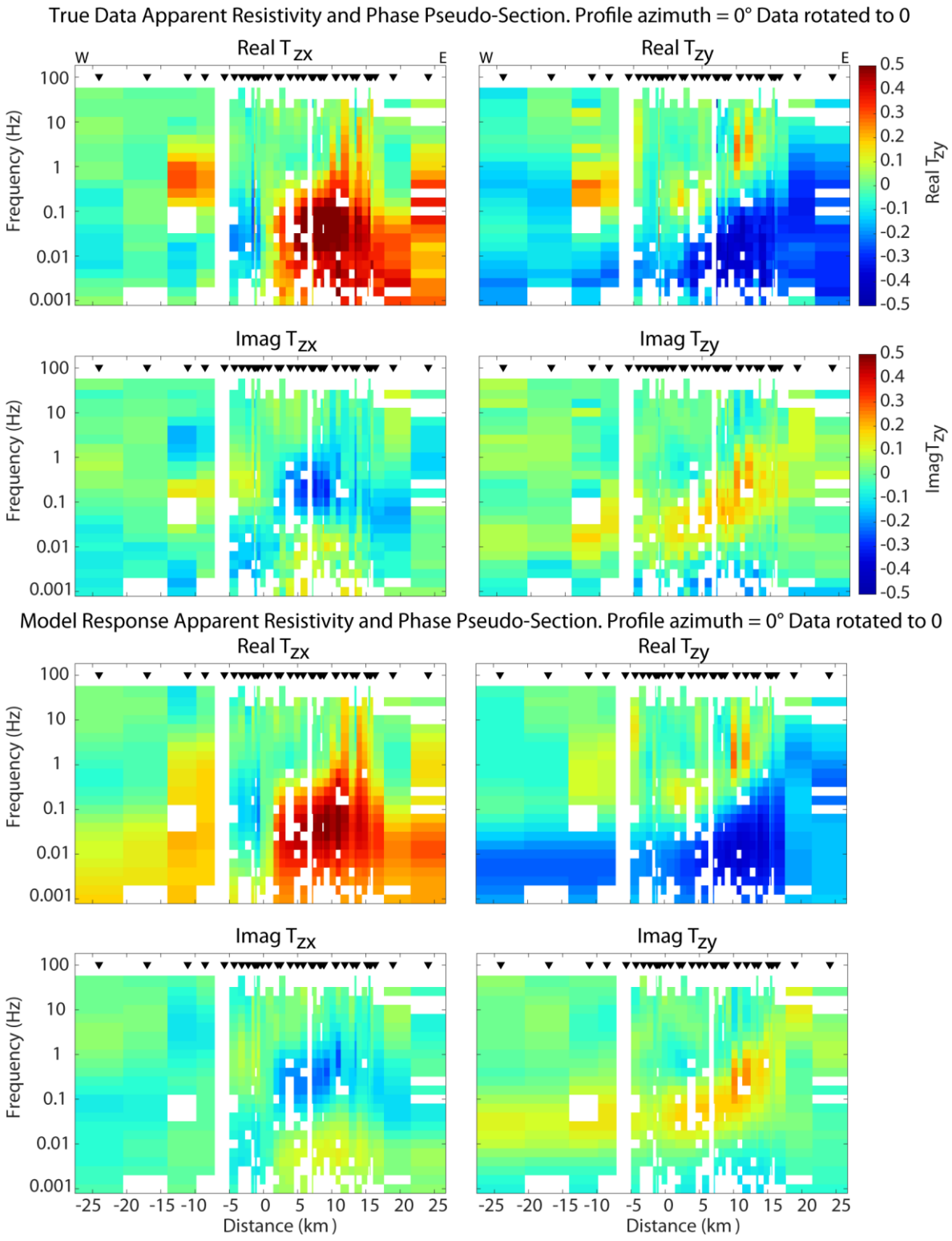

Figure 6.11: Pseudosections of the Real and Imaginary components of the tipper comparing the real data (top 4 panels) and the inversion watson_lake_inv21 (bottom 4 panels).

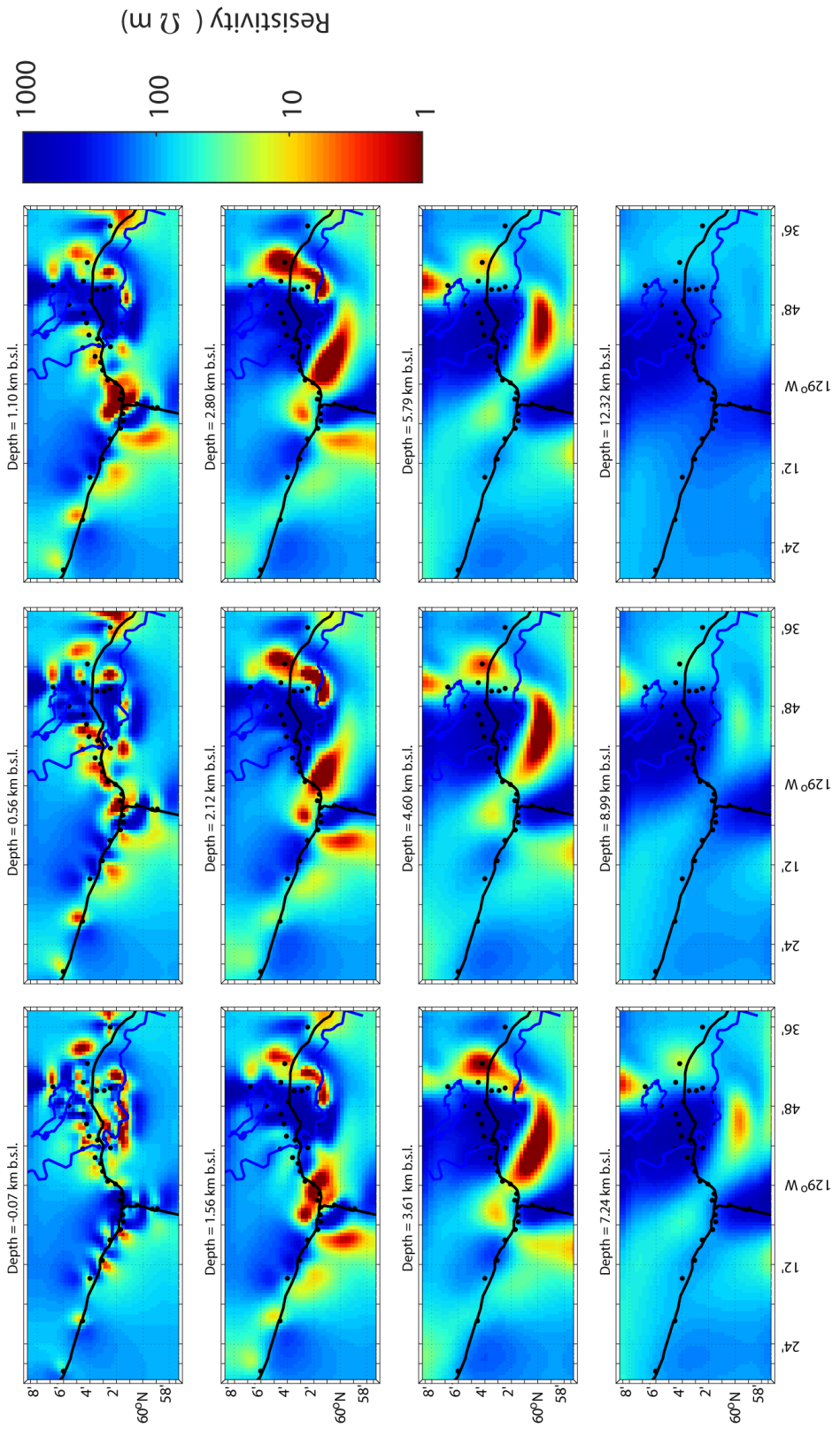

Figure 6.12: Horizontal cross-sections at select depths for the resistivity model results for inversion watson_lake_inv21. The black lines represent highways, and the blue lines outline the Liard River and Watson Lake.

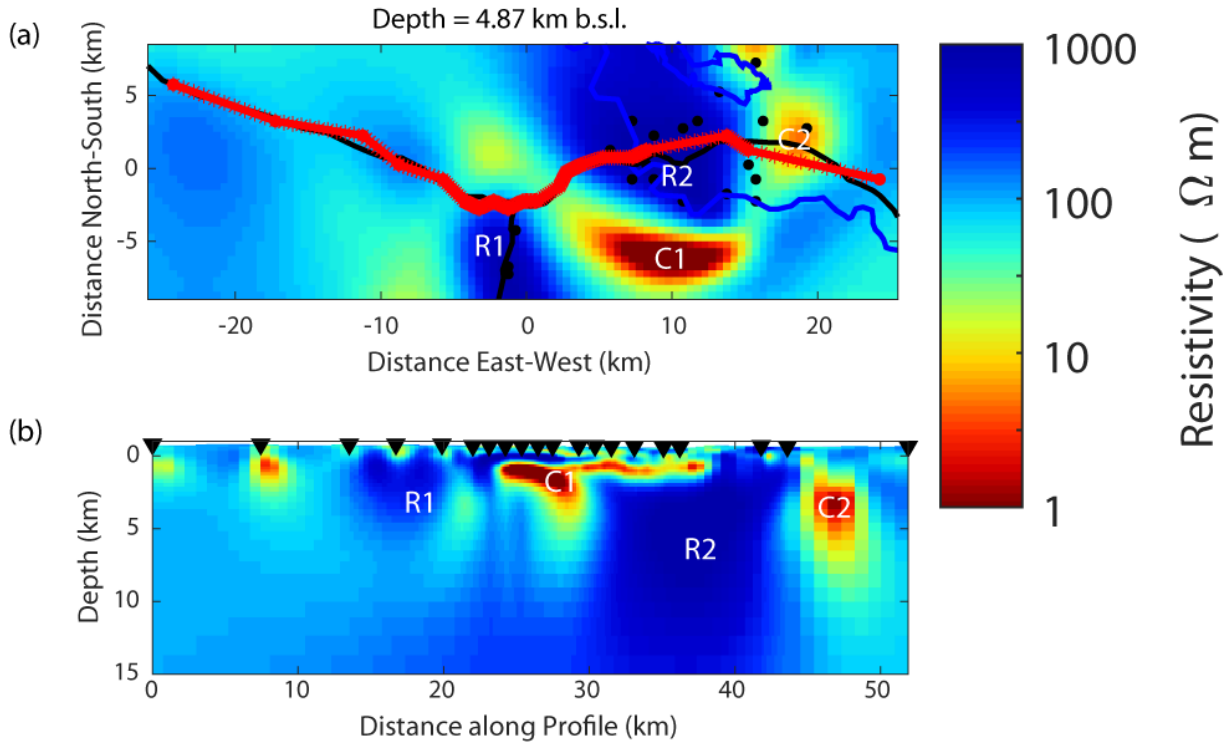

Figure 6.13: (a) horizontal and (b) vertical cross-sections of watson_lake_inv21 taken from a profile of stations along the Alaska Highway (red line). The conducting features of the model are labelled as C1 and C2. The resistive features are labelled as R1 and R2.

Inversion Name	watson_lake_syn1	watson_lake_syn2	watson_lake_syn3	watson_lake_syn4	watson_lake_syn5	watson_lake_syn6
Number of Stations	40	40	40	40	40	40
Minimum Period (s)	0.01	0.01	0.01	0.01	0.01	0.01
Maximum Period (s)	1000	1000	1000	1000	1000	1000
Number of Frequencies	24	24	24	24	24	24
Error Floor (Z)	5%	5%	5%	5%	5%	5%
Starting Model Resistivity (Ωm)	100	100	100	100	100	100
Synthetic Model	3 Ωm Conducting Layer (thick)	3 Ωm Conducting Prism (thick)	3 Ωm Conducting Layer (thin)	3 Ωm Conducting Prism (thin)	3 Ωm Conducting Fault (deep)	3 Ωm Conducting Fault (shallow)
X-Cells	72	72	72	72	72	72
Y-Cells	140	140	140	140	140	140
Z-Cells	77	77	77	77	77	77
Total Cells	776160	776160	776160	776160	776160	776160
RMS Misfit Start	23.18	9.68	19.38	8.93	11.25	7.64
RMS Misfit End	0.97	0.93	1.06	0.97	1.00	0.96
Total Iterations	111	65	109	54	102	81

Table 6.2: List of parameters for select synthetic ModEM inversions for the Watson Lake MT data.

6.4.1 Conducting Layer Synthetic Inversion

Synthetic inversion 3 consisted of a "true" resistivity model with a 3 Ωm conducting layer inserted between 0.5 and 3 km in a 100 Ωm halfspace (Figure 6.14(c)). The forward data generated from ModEM,

which had been edited to include random noise, was inverted using the same model described in 6.2.1 as the starting model. The inversion utilized only the impedance tensor data with error floors of 5% and ran for a total of 109 iterations with a final RMS misfit of 1.06. The results of the inversion (Figures 6.14 - 6.16) show that the conducting layer is well resolved, even in areas without station data, and Figure 6.17 shows good fit between the "true" data from the synthetic model and the inversion model results.

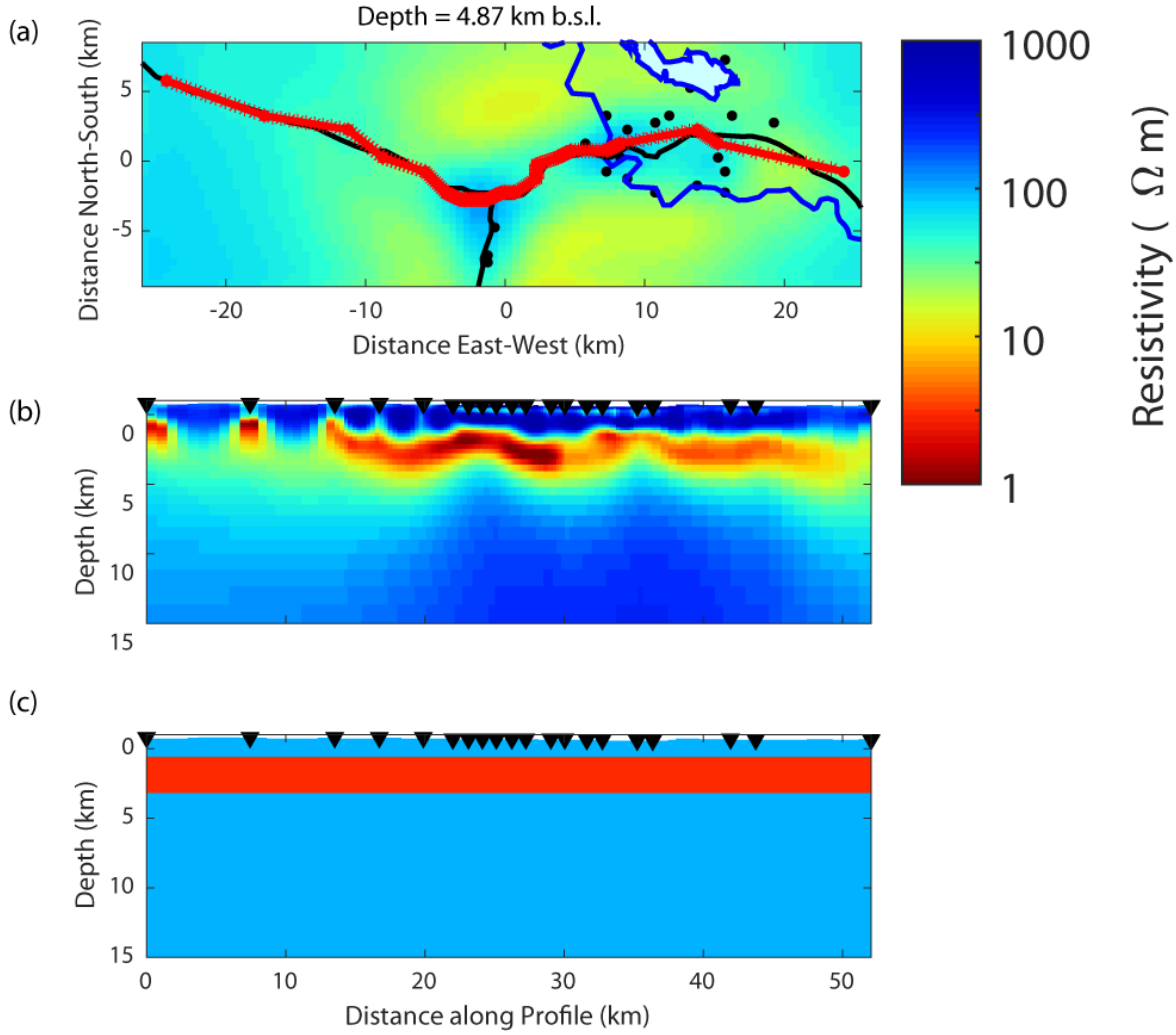

Figure 6.14: (a) horizontal and (b) vertical cross-sections of the conducting layer synthetic inversion model taken from a profile of stations along the Alaska Highway (red line). (c) shows a vertical cross-section taken from the true model used to generate the synthetic data.

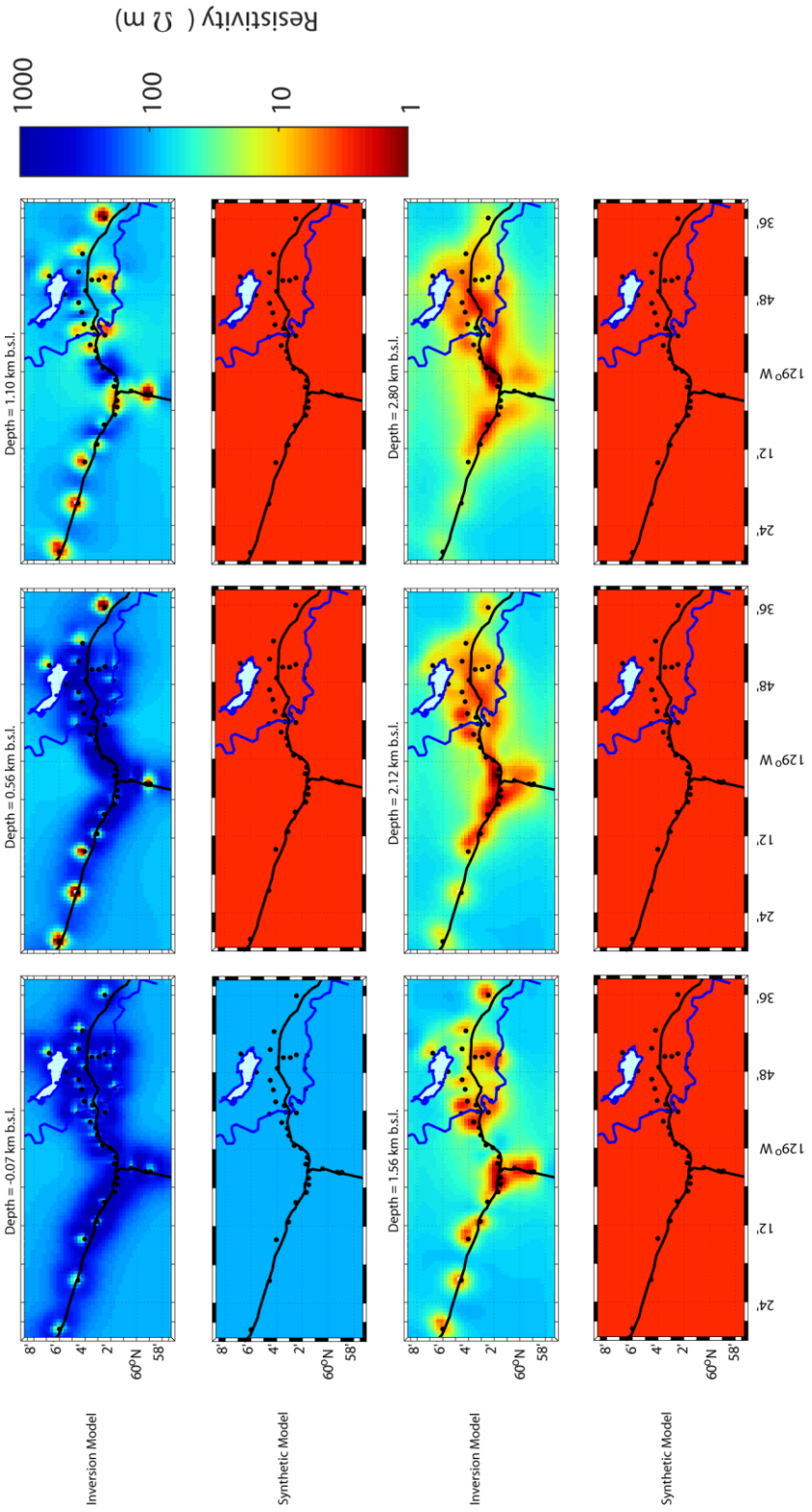

Figure 6.15: Horizontal cross-sections at select depths between -0.07 and 2.80 km b.s.l. for the conducting layer synthetic inversion model. The slices compare the results of the inversion model with the synthetic data used in the inversion The black lines represent highways, and the blue lines outline the Liard River and Watson Lake.

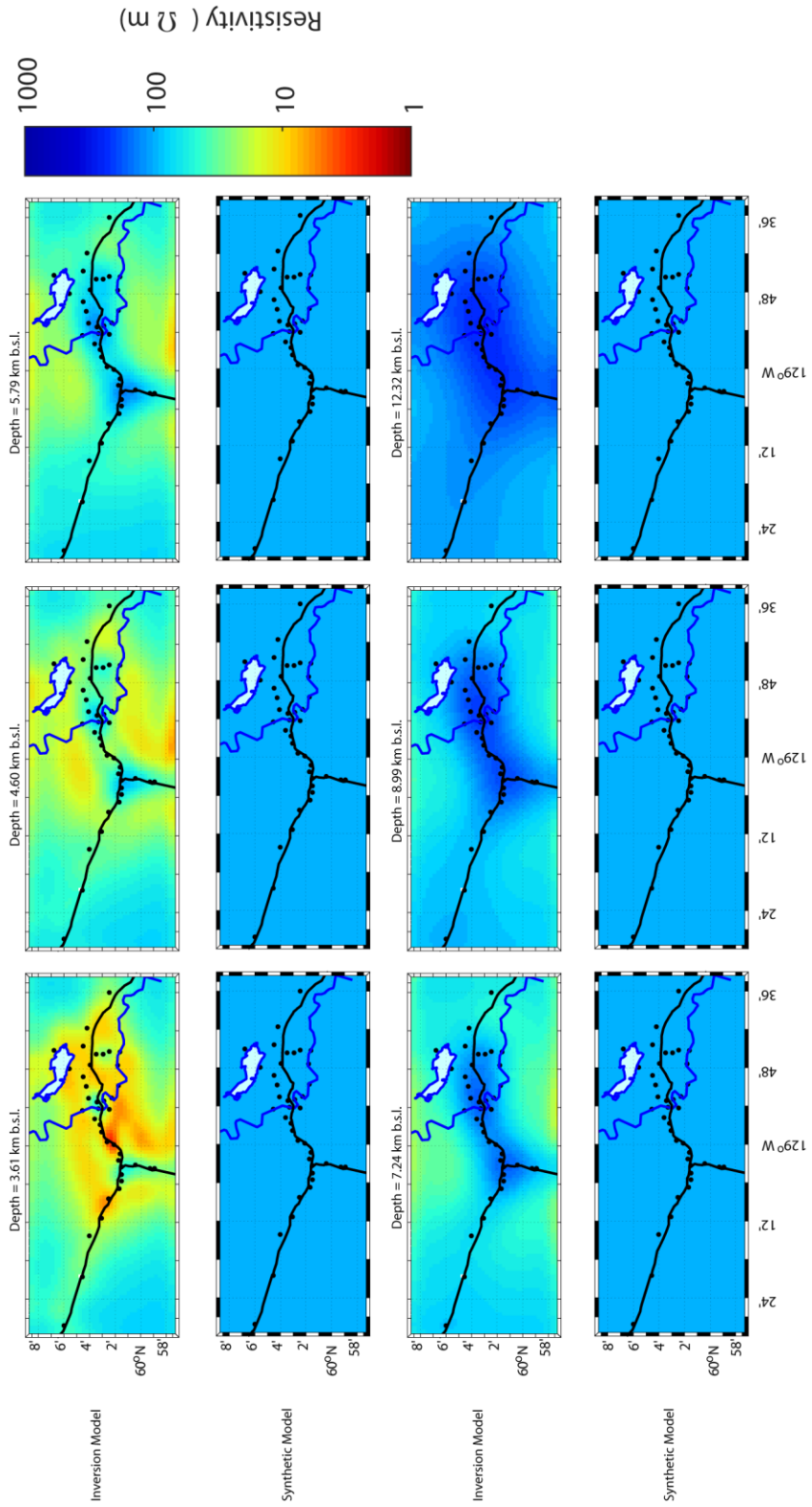

Figure 6.16: Horizontal cross-sections at select depths between 3.61 and 12.32 km b.s.l. for the conducting layer synthetic inversion model. The slices compare the results of the inversion model with the synthetic data used in the inversion The black lines represent highways, and the blue lines outline the Liard River and Watson Lake.

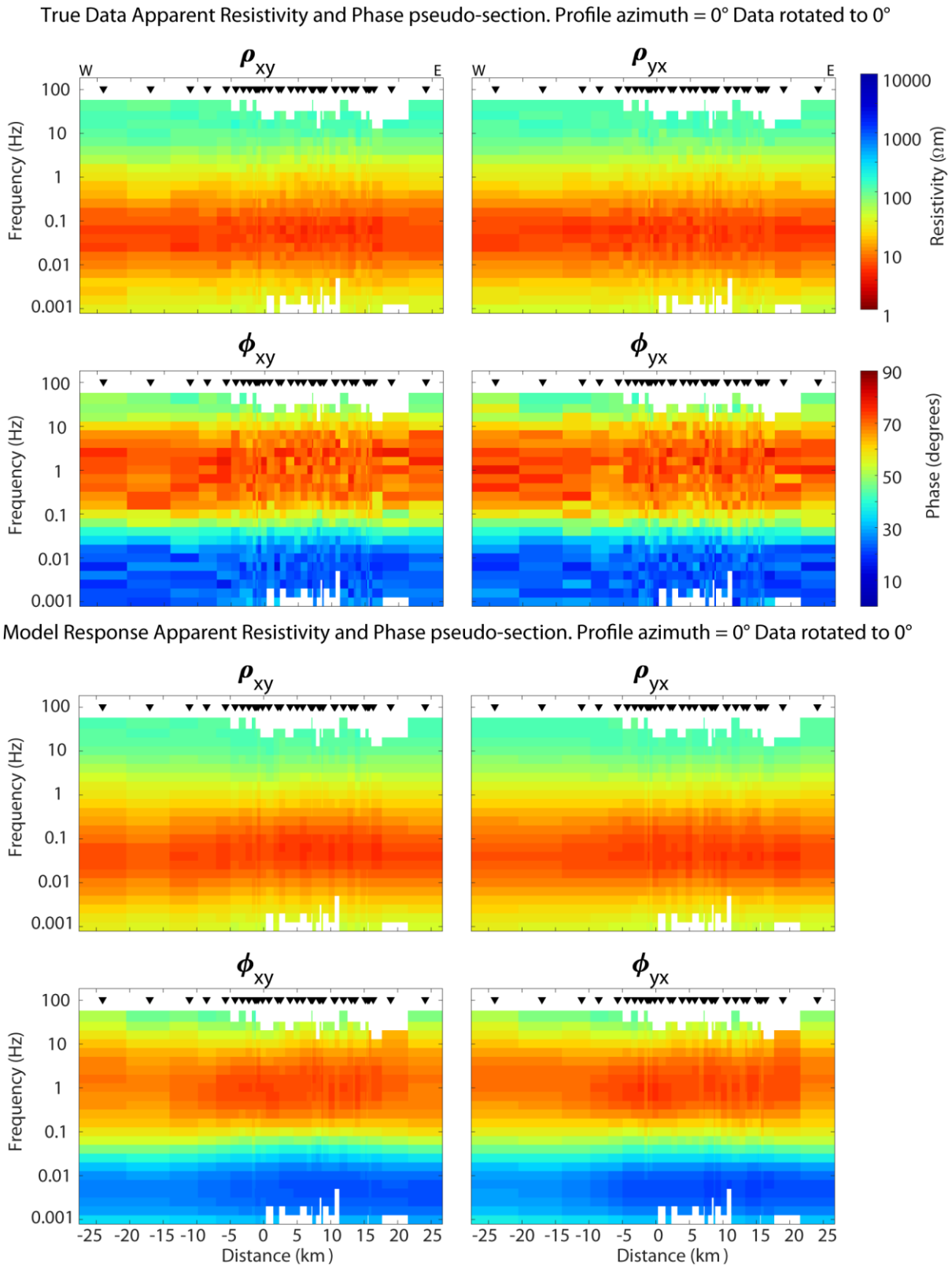

Figure 6.17: Apparent resistivity and phase pseudosections for off-diagonal components of the impedance tensor for the true data (top 4 panels) compared with the conducting layer synthetic inversion (bottom 4 panels).

6.4.2 Conductive Prism Synthetic Inversion

This synthetic inversion (synthetic inversion 4) was conducted using a "true" resistivity model of a 3 Ωm conducting prism inserted in a 100 Ωm halfspace (Figure 6.18(c)). The forward data generated from ModEM, which had been edited to include random noise, was inverted using the same model described in 6.2.1 as the starting model. The inversion utilized only the impedance tensor data with error floors of 5% and ran for a total of 54 iterations with a final RMS misfit of 0.97. The results (Figures 6.18 – 6.21) show that the conducting prism was well resolved and there is good agreement between the synthetic model and the inversion model.

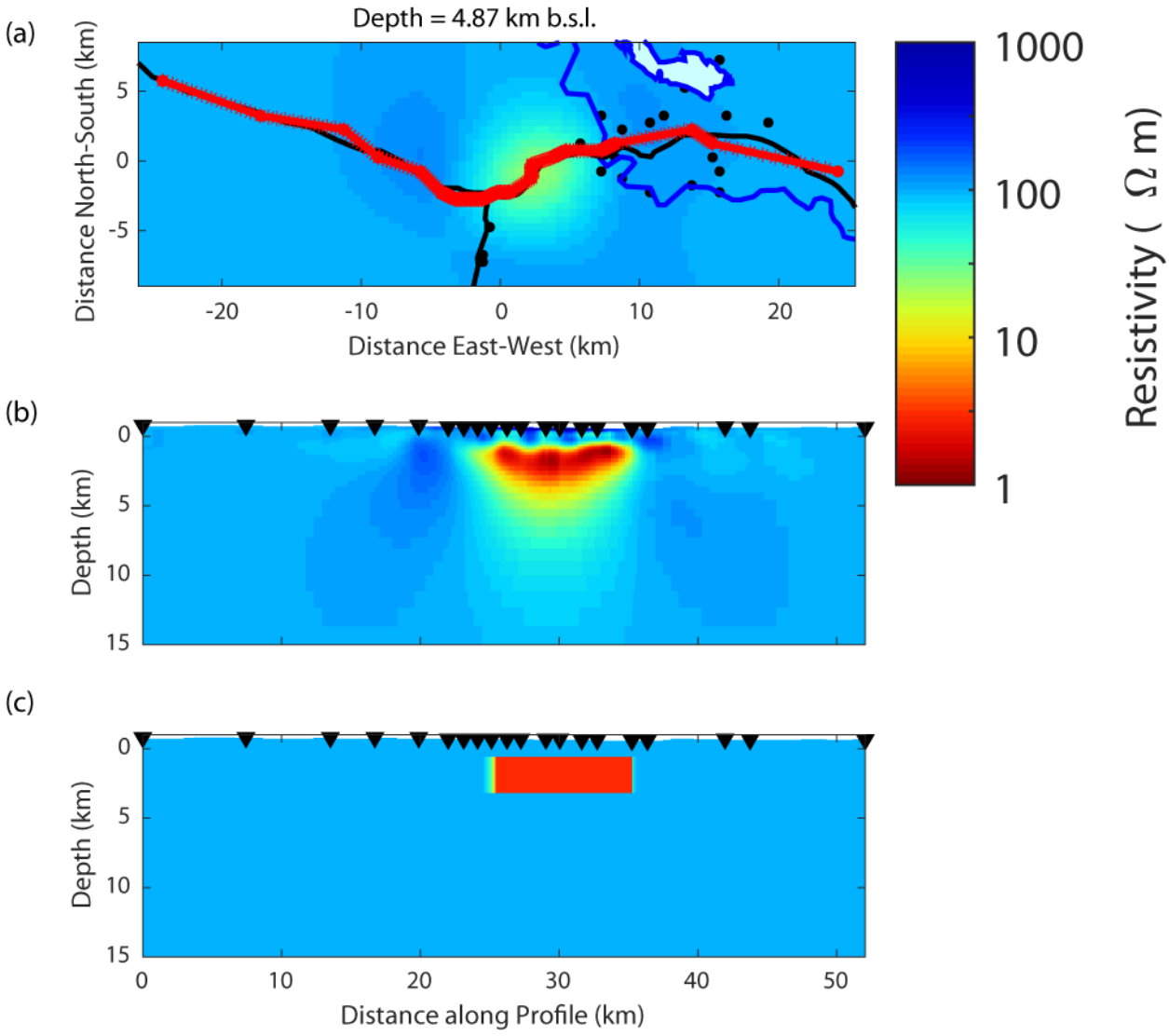

Figure 6.18: (a) horizontal and (b) vertical cross-sections of the conducting prism synthetic inversion model taken from a profile of stations along the Alaska Highway (red line). (c) shows a vertical cross-section taken from the true model used to generate the synthetic data.

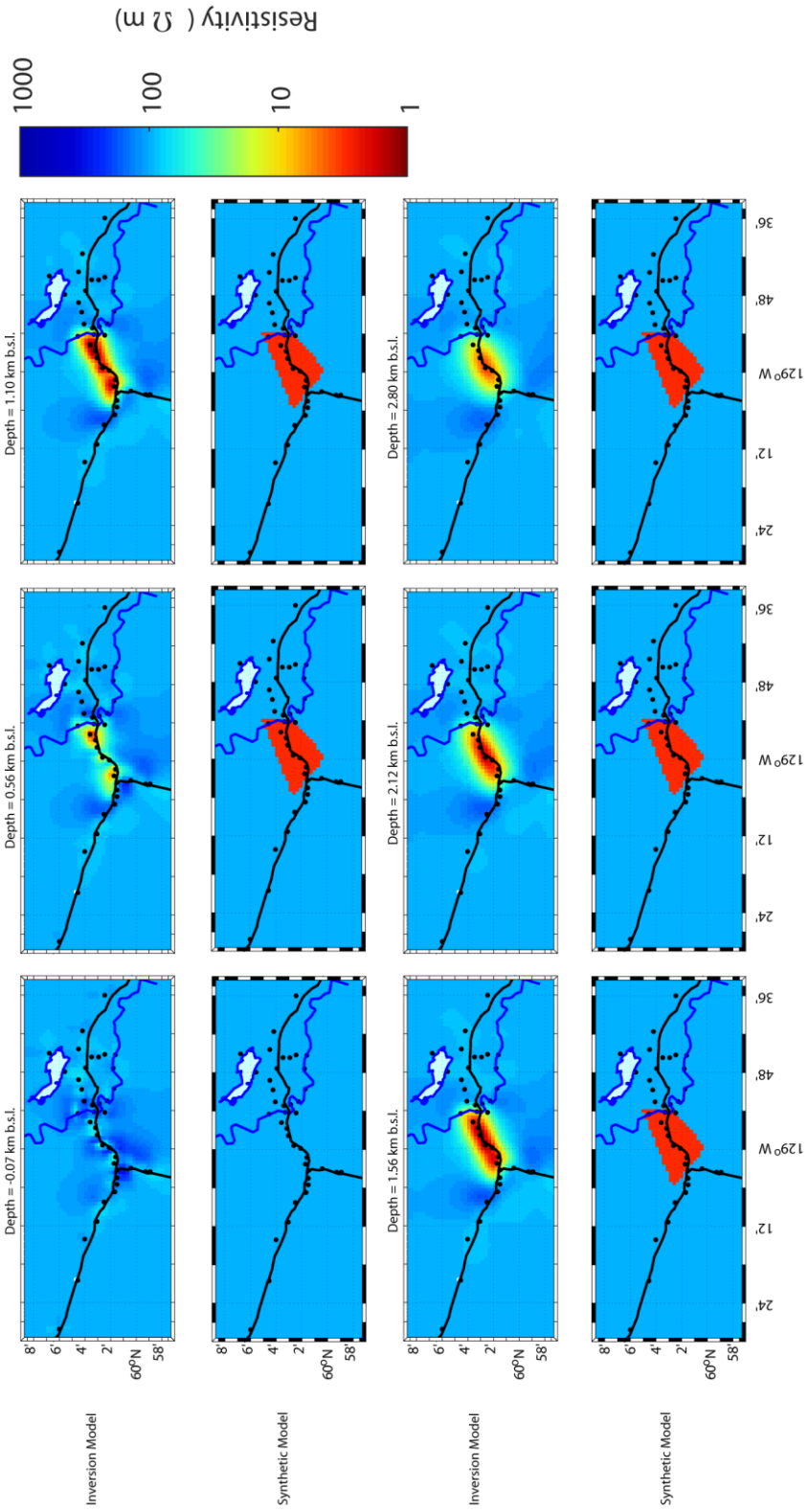

Figure 6.19: Horizontal cross-sections at select depths between -0.07 and 2.80 km b.s.l. for the conducting prism synthetic inversion model. The slices compare the results of the inversion model with the synthetic data used in the inversion The black lines represent highways, and the blue lines outline the Liard River and Watson Lake.

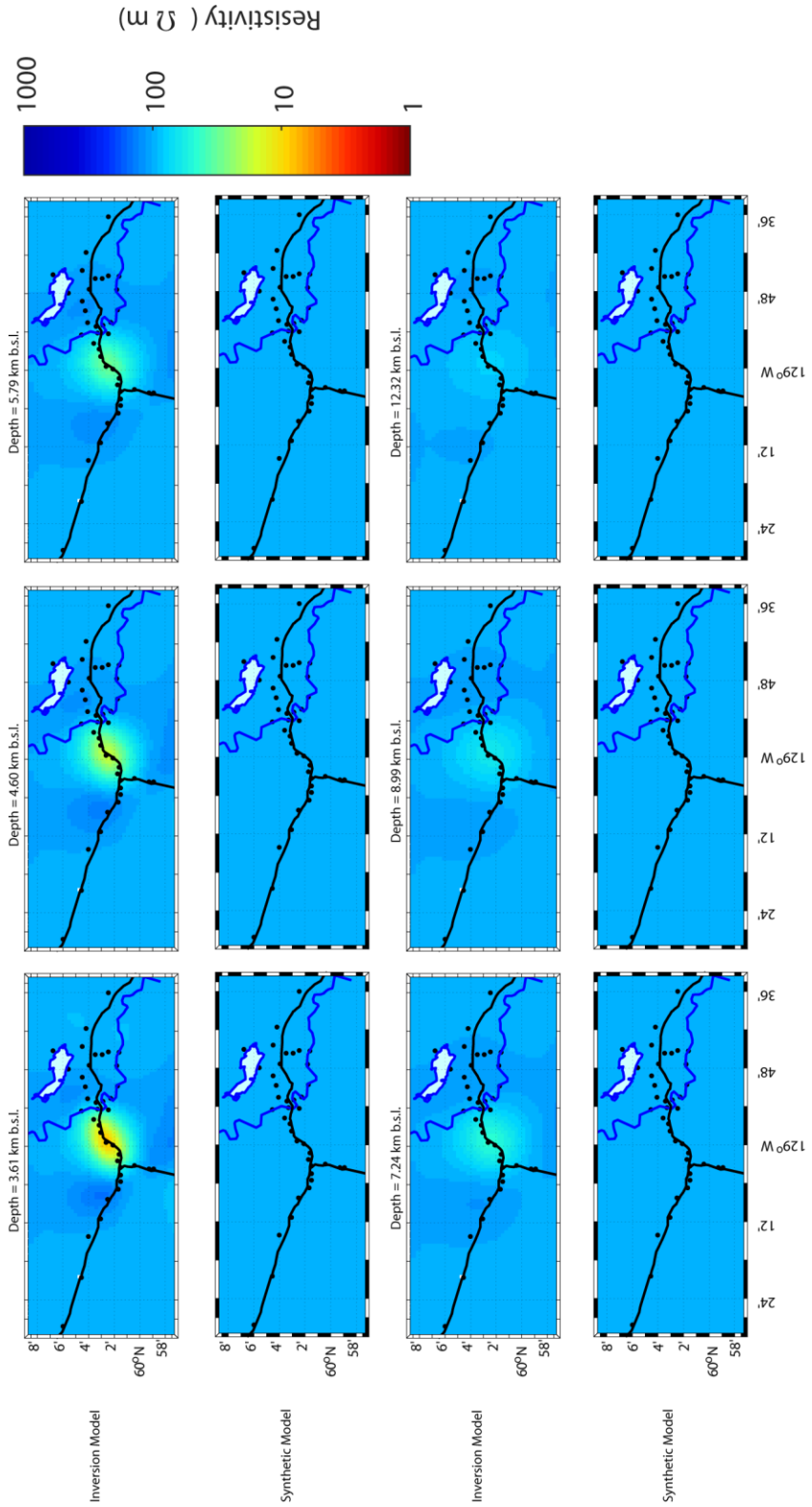

Figure 6.20: Horizontal cross-sections at select depths between 3.61 and 12.32 km b.s.l. for the conducting prism synthetic inversion model. The slices compare the results of the inversion model with the synthetic data used in the inversion The black lines represent highways, and the blue lines outline the Liard River and Watson Lake.

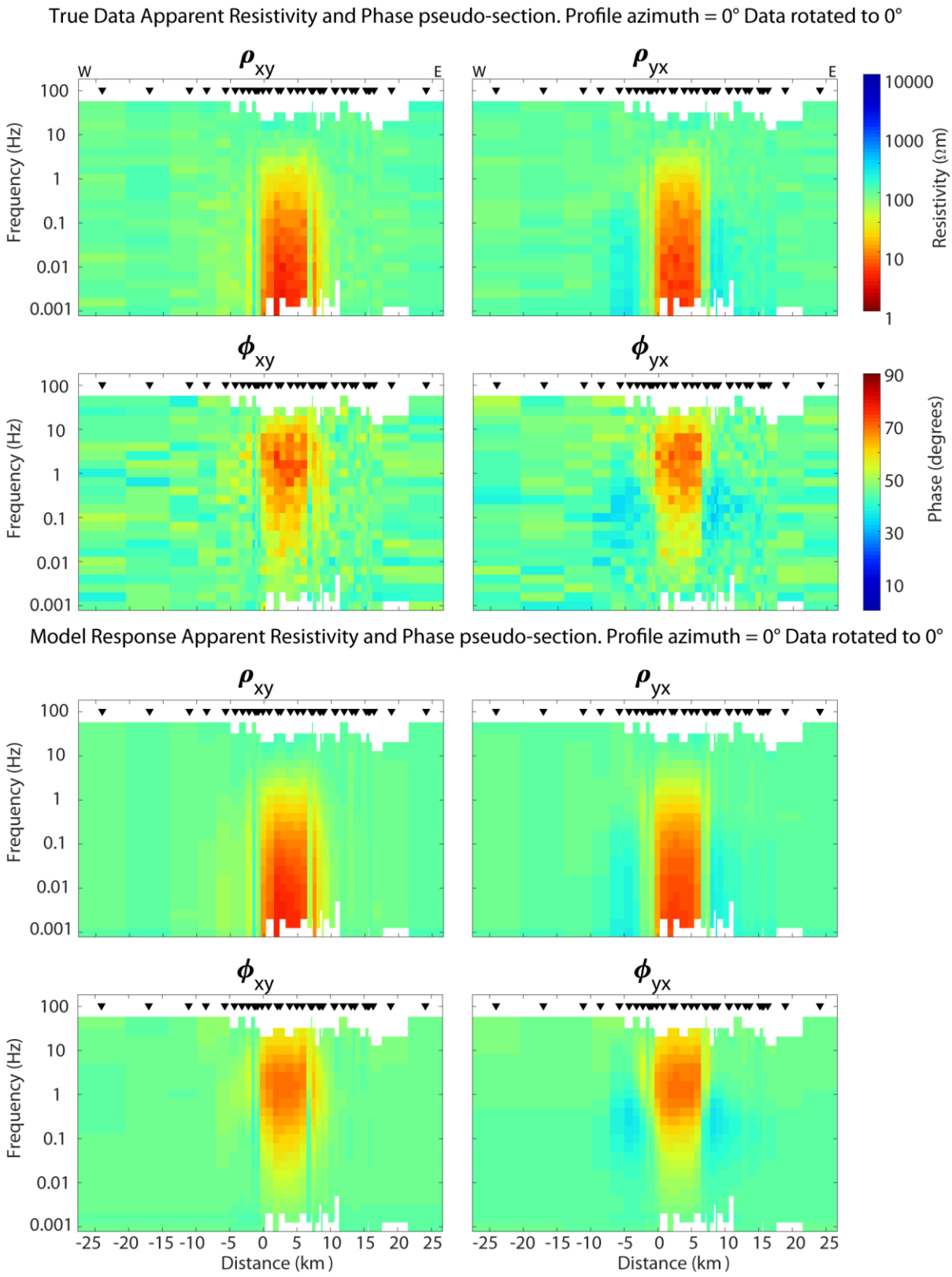

Figure 6.21: Apparent resistivity and phase pseudosections for off-diagonal components of the impedance tensor comparing the true data (top 4 panels) with the conducting prism synthetic inversion (bottom 4 panels).

6.4.3 Deep Conducting Fault Synthetic Inversion

The “true’ resistivity model for synthetic inversion 5 used a 3 Ωm conducting fault inserted into a 100 Ωm halfspace. The fault extended from a depth of 0.5 km to 30 km below sea level and was oriented at -30° to approximately align with the strike of the Tintina Fault. The ModEM inversion was run using only the impedance tensor data and error floors of 5%, it ran for a total of 102 iterations with a final RMS misfit of 1.00. The features of the fault are well resolved, the top and sides of the fault are well constrained, however the depth of the fault is not due to limitations of the magnetotelluric method.

6.4.4 Shallow Conducting Fault Synthetic Inversion

Synthetic inversion 6 used a nearly identical “true” resistivity model as synthetic inversion 5, except with the depth of the fault now extending from 0.5 km to 3 km below sea level (Figure 6.22(c)). This inversion was also an impedance tensor-only inversion with error floors of 5%. It ran for a total of 81 iterations with a final RMS misfit of 0.96. Figures 6.22 – 6.25 below show that the fault was well resolved in the inversion model.

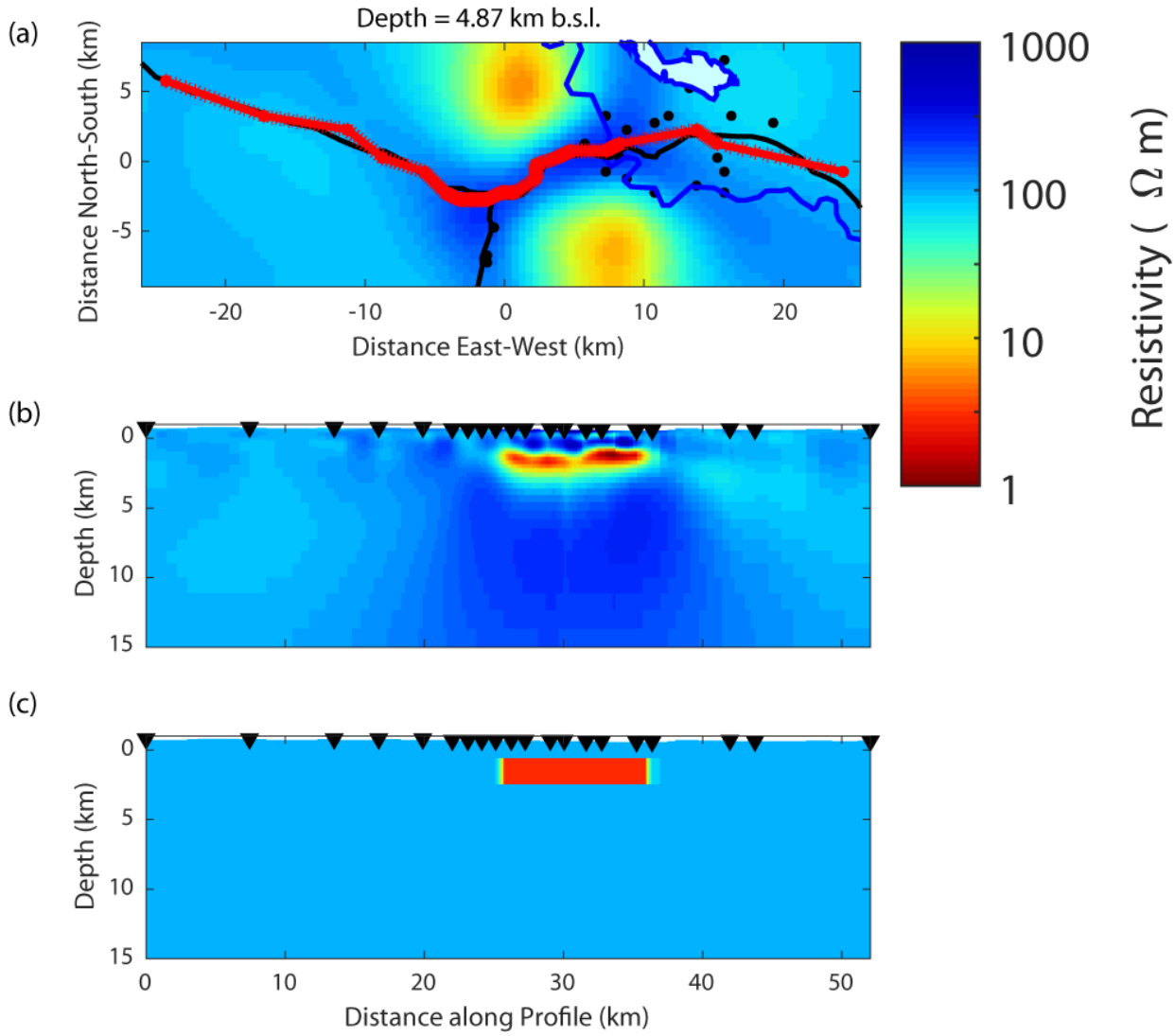

Figure 6.22: (a) horizontal and (b) vertical cross-sections of the shallow conducting fault synthetic inversion model taken from a profile of stations along the Alaska Highway (red line). (c) shows a vertical cross-section taken from the true model used to generate the synthetic data.

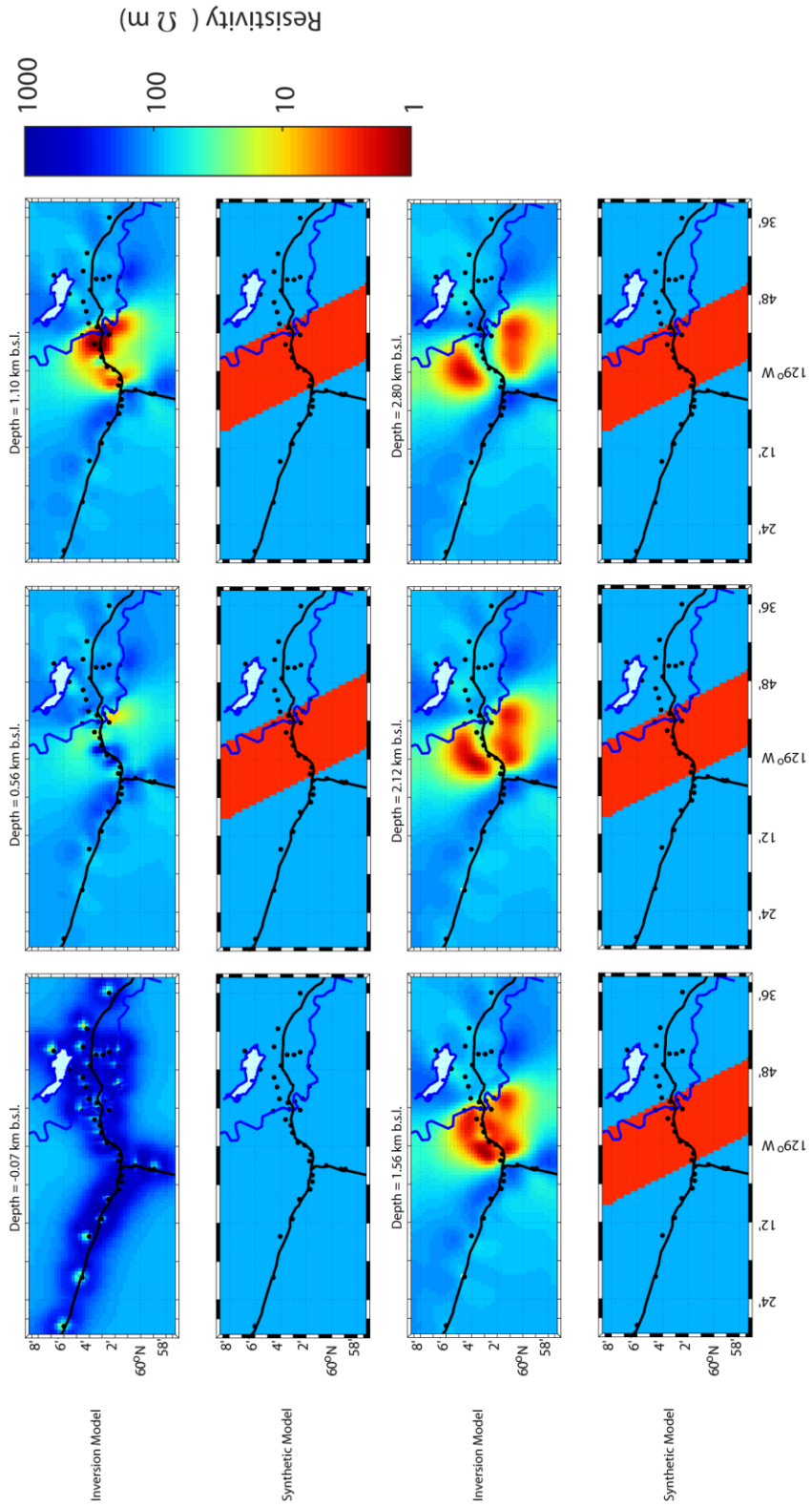

Figure 6.23: Horizontal cross-sections at select depths between -0.07 and 2.80 km b.s.l. for the shallow conducting fault synthetic inversion model. The slices compare the results of the inversion model with the synthetic data used in the inversion. The black lines represent highways, and the blue lines outline the Liard River and Watson Lake.

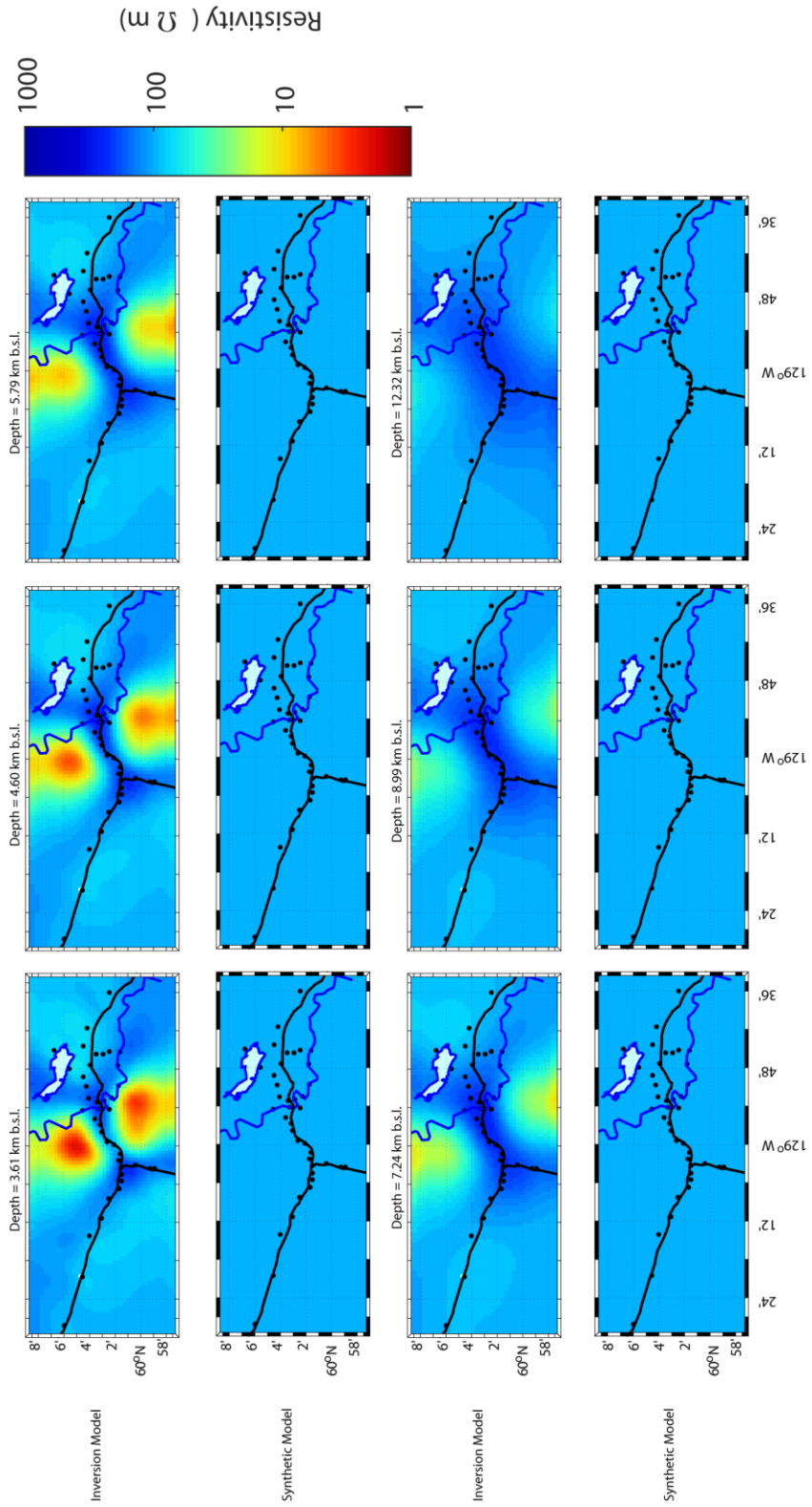

Figure 6.24: Horizontal cross-sections at select depths between 3.61 and 12.32 km b.s.l. for the shallow conducting fault synthetic inversion model. The slices compare the results of the inversion model with the synthetic data used in the inversion. The black lines represent highways, and the blue lines outline the Liard River and Watson Lake.

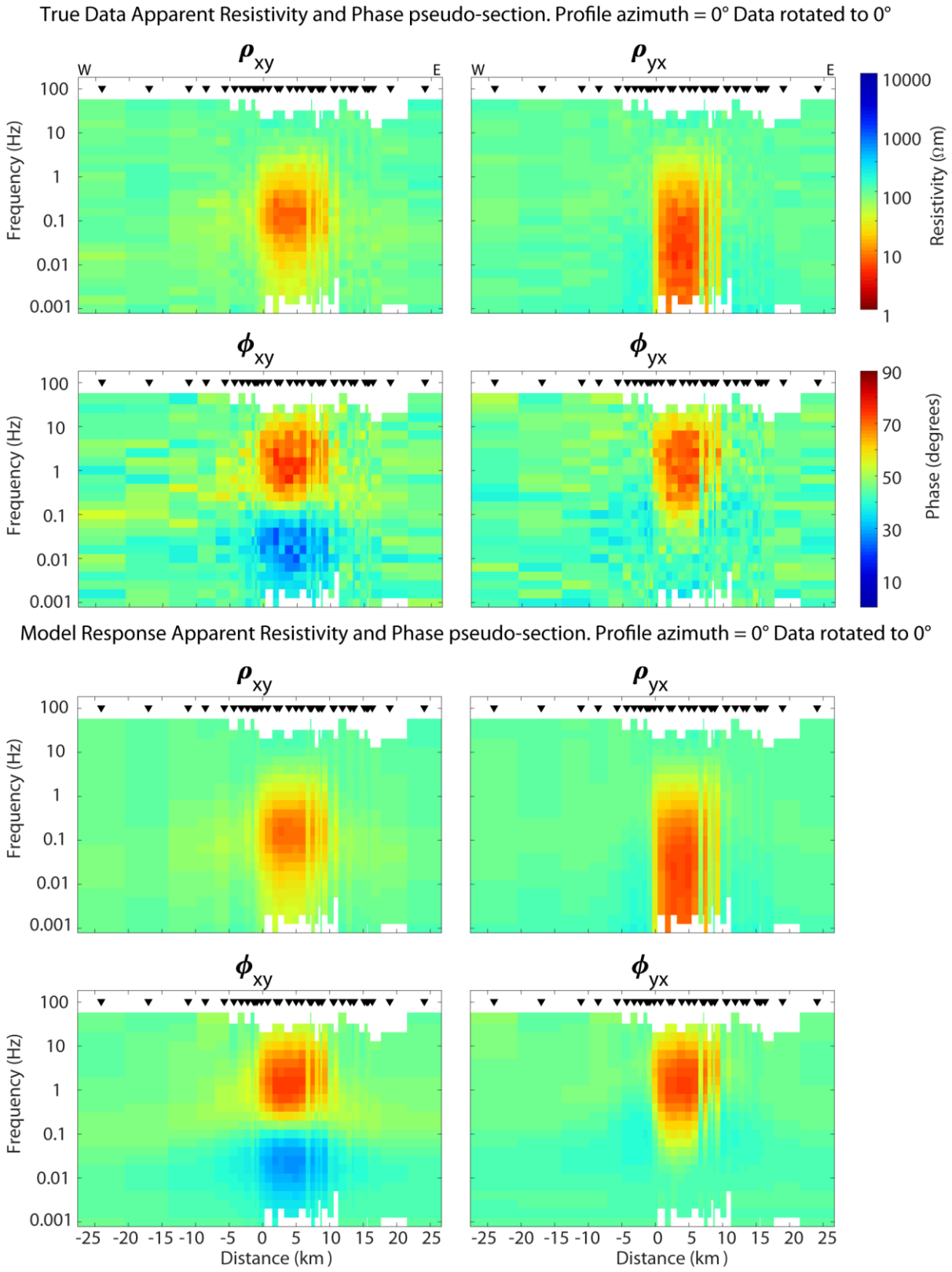

Figure 6.25: Apparent resistivity and phase pseudosections for off-diagonal components of the impedance tensor comparing the true data (top 4 panels) with the shallow conducting fault synthetic inversion (bottom 4 panels).

6.4.5 Sensitivity Tests

Sensitivity tests are a way of determining which features in the inversion model are required by the MT data to maintain an acceptable RMS misfit. Two different kinds of sensitivity tests were used to constrain features of the preferred inversion model.

First, the central conductor C1 was edited, and replaced with a uniform area with a resistivity of 100 Ωm. Forward modelling was then used to generate new MT data responses to compare with the inversion model data. The RMS misfit was compared for each station, and for the total RMS misfit of the models. The results of this test showed an increase in total RMS misfit from 1.89 in the original inversion model to a value of 7.69 for the model without C1. This shows that the conductor is necessary for the model to fit the original data. Similarly, if C2 is edited and replaced with a 100 Ωm area, the RMS misfit increases to 3.50. This shows that C2 is also required for an acceptable RMS misfit.

The second type of sensitivity test determined the depth of investigation for the MT survey. The model was edited such that the resistivity values below a certain depth were a uniform 100 Ωm. Forward modelling was used to generate responses to compare the resulting RMS misfit with the original model. This was repeated for increasing values of depth until the edited model's RMS misfit did not improve. Results are detailed in Table 6.3. From these tests it was seen that as the top of the inserted halfspace increased in depth, the RMS misfit of the edited model decreased until a depth of approximately 50 km. When a halfspace was inserted below this depth, little improvement to the RMS misfit was seen. This shows that the near-surface features of the inversion model are necessary for an acceptable RMS misfit, and that the survey had an overall depth of investigation of approximately 50 km.

Depth to 100 Ωm Halfspace (km)	New RMS Misfit
10	3.07
15	2.48
20	2.28
30	2.10
40	2.00
50	1.97

Table 6.3: New values of RMS misfit resulting from inserting a 100 Ωm halfspace into the inversion model at specified depths.

6.5 Summary of Inversions

The models summarized in sections 6.3.1 – 6.3.3 all display similar resistivity features to the initial inversion in section 6.2. The central conductor C1 is present in all 3 resistivity models with the same resistivity ranges between 1 – 10 Ωm, however the overall shape of the conductor varies. For example, the conductor from inversion 13 extends further to the West than in the other two inversion models and the conductor in inversion 21 appears much thinner in eastern portion than it does in the other two models. The model from inversion 21 also displays a much larger conductive feature C2 than in the other models. In this model, C2 has lower values for resistivity in the range of 1 – 10 Ωm compared to the range of 10 – 30 Ωm seen in inversions 13 and 23. C2 also extends deeper, below 10 km b.s.l. In the inversion 23 model, C2 is shallower than the other models, only extending to a depth of 5 km b.s.l. The sensitivity tests displayed that both conductors are required for the model to have an acceptable RMS misfit as the misfit increases greatly when these features are removed from the model.

The resistive structures R1 and R2 are also present in all three inversions, with well constrained locations. In inversion 21, R1 does not extend deeper than 5 km b.s.l., while R2 extends further West than in the other models and appears nearly vertical. The models from inversions 13 and 23 show R2 with a westward dip.

The synthetic inversions demonstrate that the resolution of the inversion models is well constrained for data located below stations. In all of the synthetic examples, the inversions were able to accurately resolve the conducting features of the synthetic models, indicating that any features resolved below the station grid in the real data inversions are well constrained in those locations as well, while features outside of the grid of stations may not be as well constrained. For example, in the horizontal cross-sections of the initial inversion model (Figure 6.3), C1 appears to dip towards the Southeast. However, the due to the lack of station data in this area the exact location and geometry of C1 is poorly constrained.

From the results of the inversions, the locations of the conductive features C1 and C2, and the resistors R1 and R2 are well constrained across all models, but there is some variation in their lateral and vertical extent as well as their resistivity ranges. Possible geological explanations for these features will be investigated in the next chapter.

Chapter 7: Interpretation of 3D Resistivity Model at Watson Lake

7.1 Introduction

In the previous chapter, the collection and analysis of the MT dataset collected at Watson Lake was described. The 3D ModEM inversion algorithm (Kelbert et al., 2014) produced a resistivity model with several distinct resistivity features. After sensitivity and resolution tests, it was determined that these features were required for the model to fit the measured data with an acceptable value of RMS misfit. The model is shown in Figure 7.1 and has four main areas of interest: two conductors labeled C1 and C2, and two resistors labeled R1 and R2. In this chapter, I will attempt to:

(a) Explain the potential geologic cause for the conductive and resistive regions of the model.
(b) Use this interpretation to determine the feasibility of continuing geothermal energy development at Watson Lake.

To aid in our interpretation, our results are compared with other geologic and geophysical data that have been collected in the area to constrain the features of the model and reduce the level of non-uniqueness which is a consequence of using only one geophysical method.

7.2 Gravity data

In addition to the MT data collected during summer 2021, gravity data were separately collected by Aurora Geoscience as a part of the geothermal study. These gravity data were then analyzed by Jeff Witter from Innovate Geothermal Ltd and published in Witter (2022). Gravity data can be used to create models of subsurface density and can be used to determine the thickness of sedimentary layers. At Watson Lake, the final Bouguer gravity anomaly was found to range between -112 and -82 mGal. The density model obtained from the gravity data inversions suggest that the survey area contains an approximately 1 km thick sedimentary basin extending to a depth of 500m below sea level, bounded on either side by near-vertical faults. The basin is situated above the main conductor “C1” from the MT inversion model, while it appears that the conductors lie in the basement rock below the basin. The basin is bounded on either side by faults coinciding with the locations of the resistive features R1 and R2 (Witter 2022). A plot of the Bouguer gravity anomaly can be seen in Figure 7.2 which shows a negative anomaly interpreted to be caused by the basin and the density model created by Witter (2022) is shown in Figure 7.3.

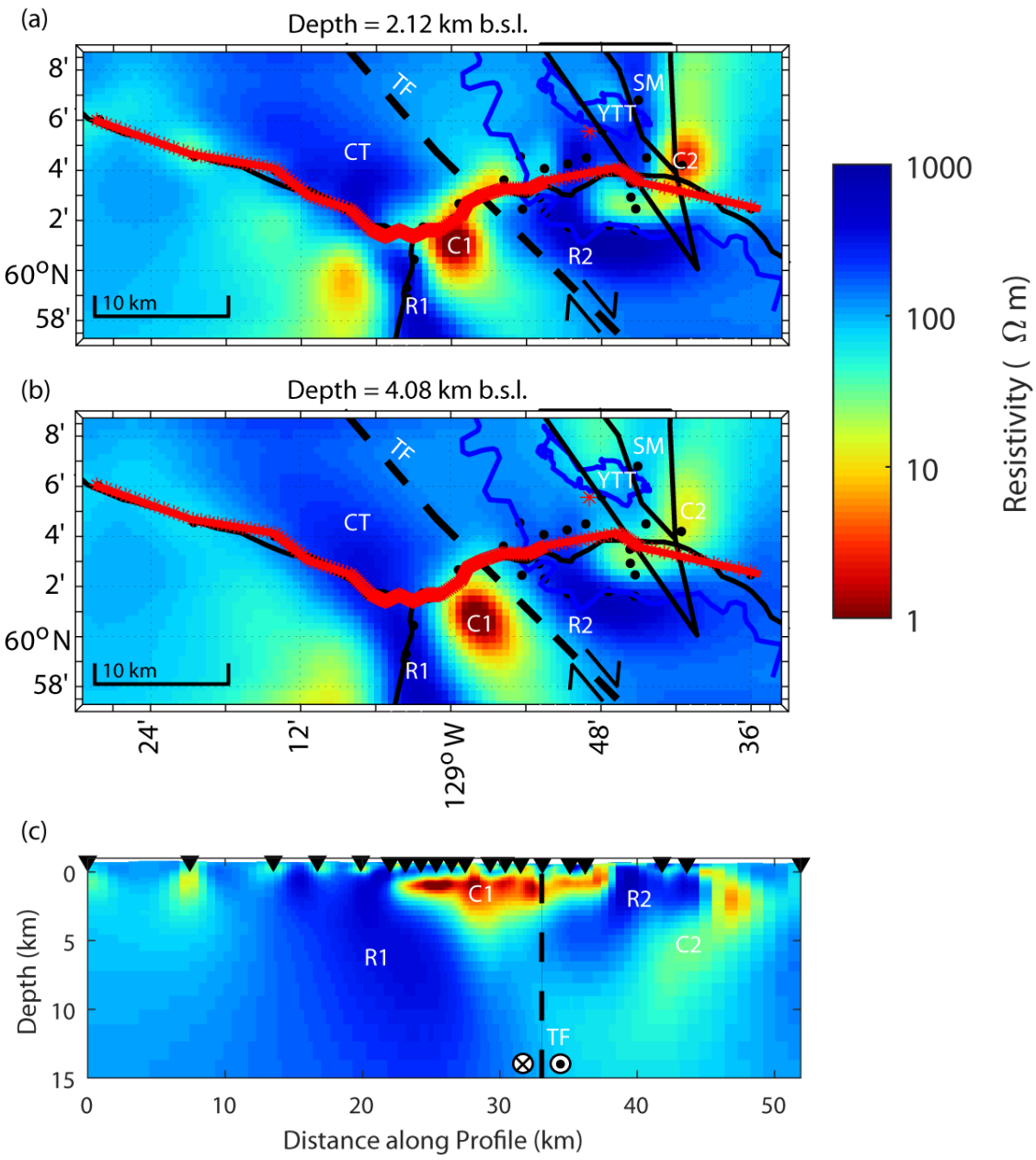

Figure 7.1: Results of the preferred inversion model. (a) and (b) display horizontal cross-sections at depths of 2.12 km b.s.l. and 4.08 km b.s.l. respectively. (c) displays a vertical cross-section taken from below a profile of stations along the Alaska highway (outlined in red on (a) and (b)). The red star in (a) and (b) represents the location of groundwater well YOWN 1512. Conductors are labelled as C1 and C2, resistors are labelled as R1 and R2. Plotted terrane boundaries (Yukon Geological Survey, 2020): CT = Cassiar Terrane, YTT = Yukon-Tanana Terrane, SMT = Slide Mountain Terrane. TF = Tintina Fault (Yukon Geological Survey, 2022).

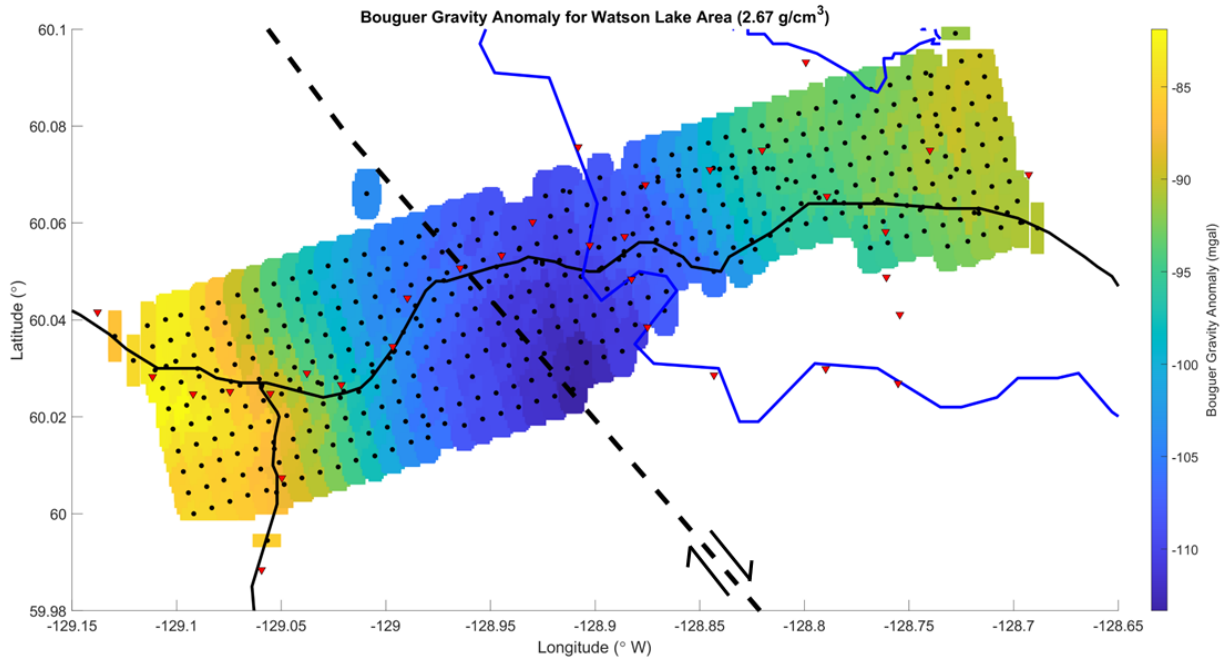

Figure 7.2: Plot of the Bouguer gravity anomaly for the Watson Lake area. Gravity stations are plotted as black circles, MT stations are plotted as red triangles. The location of the Tintina Fault from the Map of Bedrock Geology (Yukon Geological Survey, 2022), highways, (black lines) and bodies of water (blue lines) are also plotted. A full analysis of the gravity report can be found in Witter (2022).

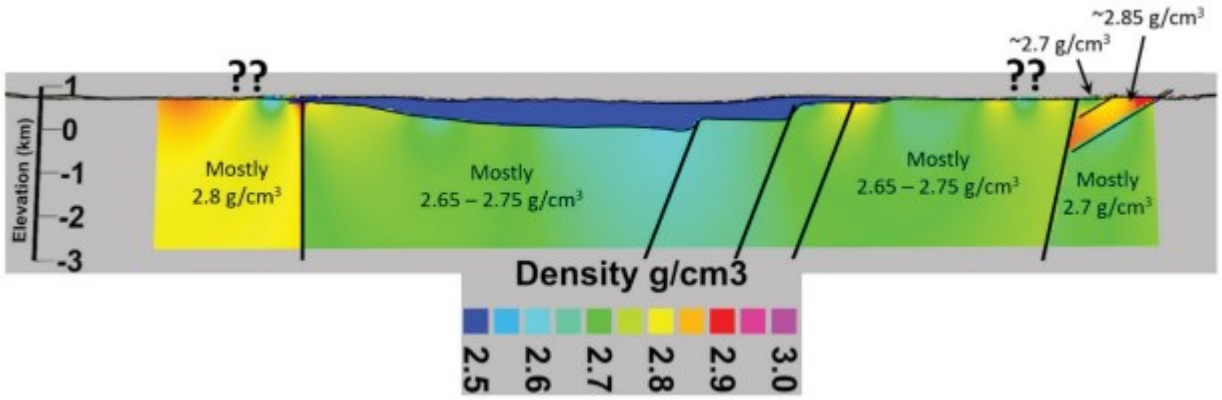

Figure 7.3: Density model obtained from the inversion of the Watson Lake Gravity data. (Modified from Witter, 2022, © Government of Yukon 2023).

7.3 Regional Geology

The geology of the Watson Lake area was described in detail in Chapter 2. The main geologic feature of the Watson Lake area is the Tintina Fault zone, a dextral strike-slip fault system with a northwest strike. The Tintina Fault zone is the boundary between two terranes in the area, the Cassiar terrane is West of the fault and is composed primarily of carbonates, siliclastic rock types, and shales ranging from Neoproterozoic to Triassic in age. East of the fault is the Yukon-Tanana terrane, composed of Late Devonian to Late Permian metasedimentary rock (Yukon Geological Survey, 2020). During the Eocene, a portion of the Yukon-Tanana terrane West of the Tintina Fault was shifted approximately 430 km Northwest due to movement along the fault (Gabrielse et al., 2006). The Slide Mountain terrane is east of the Yukon-Tanana terrane and primarily contains igneous rocks as well as cherts and argillites (Yukon Geological Survey, 2020). It is expected that the area surrounding the fault zone would possibly contain other fault strands and fractured rock, which would allow for the circulation of pore fluid that may be a possible explanation for the conducting features seen in the inversion model (Figure 7.1). The Map of Bedrock Geology for the Watson Lake area (Yukon Geological Survey, 2022) displays some basalt rocks in the area which could indicate past volcanic activity that could be a source of previous hydrothermal alteration.

7.4 Possible Explanations for Conductors C1 and C2

From the inversion results discussed in Chapter 6, the study area appears to contain two larger conducting bodies characterized by resistivity values below 100 Ωm (Figure 7.1). These are the large, central conductor (C1) and the smaller conductor, east of the survey area (C2). There are several possible explanations for the low resistivity of these features. Determining the cause of the conducting features has important implications for the future of geothermal development at Watson Lake, as they may be related to the hot pore fluid and permeable, fractured rock required for geothermal energy production.

7.4.1 Pore Fluids Within a Layer of Sedimentary Rock

The first possibility is that the low resistivity is due to pore fluid located in the host rock. Many rocks are composed of a mixture of (1) high resistivity mineral grains with cement holding the grains together and (2) pore space between the grains that may contain fluids. If the pore fluid is water containing dissolved

minerals, then it will have a low resistivity (Nesbitt, 1993). The overall resistivity is then calculated as an average of the two phases using a mixing law such as Archie's Law. The presence of low resistivity fluids would lower the overall resistivity of the host rock making it appear as a conductor (zone of low resistivity) in the inversion model. The bulk resistivity of the fluid bearing rock will depend on several factors: the resistivity of the grains, the porosity, the saturation of the pore space, the resistivity of the pore fluid, and the cementation factor of the pores (the shape of the pores). Rock types with lower valued cementation factors will have less consolidated grains resulting in ellipsoidal shaped pores which will tend to be more interconnected than spherical pores and thus will require lower values of porosity to explain the same measured resistivities. There are a variety of mixing laws proposed to calculate the resistivity of a two-phase system composed of grains and fluids, here Archie's Law is used, which ignores grain resistivity, as detailed in Section 4.7 (Archie, 1942):

$$\rho = \rho_w a S^{-n} \phi^{-m} \qquad (6.1)$$

Fluid resistivity was calculated using the empirical equation from Block (2001) which they derived using 17611 data points:

$$\rho_w = 4.5 * TDS^{-0.85} \qquad (6.2)$$

where TDS is measured in g/litre.

The conductor "C1" in the inversion model has a resistivity ranging between 1 and 10 Ωm. Using Archie's Law a range of potential values for the porosity can be calculated. Limited water well data lists the TDS of sampled groundwater near Watson Lake as 350 mg/litre (Government of Yukon, 2019). From equations 6.1 and 6.2, the fluid resistivity would be approximately 11 Ωm, and the porosity range would be between 110% and 1100% in order to appear as an area of resistivity between 1-10 Ωm using a cementation factor of 1 and a tortuosity of 1. These are unrealistic values of porosity. Furthermore, the sample well YOWN1512 (Red star in Figure 7.1) is a significant distance from C1 and was sampled at an unknown depth. Thus, a range of other values for TDS were also tested.

Using TDS values of 0.1, 1, and 10 g/L, and assuming a tortuosity of 1, three plots were made using cementation factors of 1, 1.5, and 2 (Figure 7.4) to better determine a range of possible porosity values.

From Figure 7.4, in order to have a resistivity of between 1 and 10 Ωm, a rock with a cementation factor of 1 (ellipsoidal pores) and pore fluid TDS of 10 g/L would require a porosity between 0.07 and 0.5. The lower end of the porosity range is reasonable, but it would require a high value of pore fluid TDS

(greater than 10 g/L). Meanwhile a pore fluid TDS of 1 g/L would require a porosity greater than 0.5, which is unrealistic for fractured rock. For rock types with higher values of cementation factors, the required porosity is even higher and thus even less realistic.

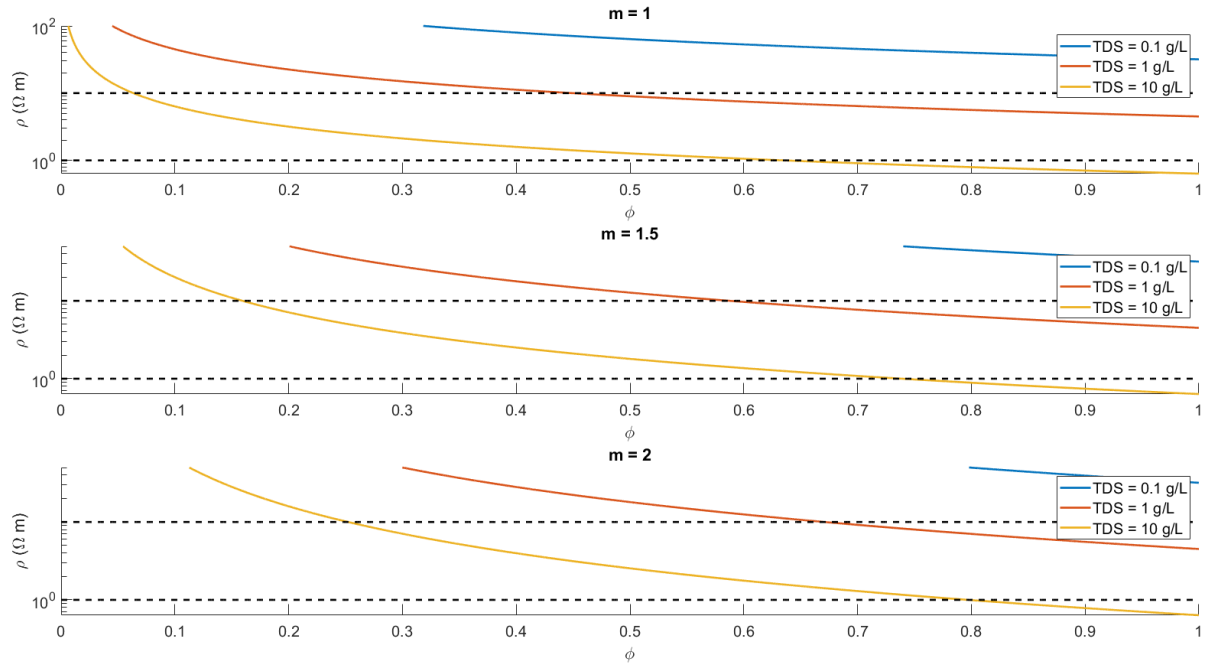

Figure 7.4: Plot of resistivity as a function of porosity following Archie's Law for rock types with a cementation factor of 1, 1.5, or 2 and a pore fluid TDS of 0.1, 1, and 10 g/L.

Ussher et al., (2000) list pore fluid resistivities for known geothermal fields to range from approximately 0.03 – 3 Ωm, and tortuosity values to range from 0.6 – 1.6. Using these values in Archie's Law would give a necessary rock porosity of at least 0.0018 for a cementation factor of 1 and a porosity of at least 0.042 for a cementation factor of 2. These are more realistic values for the porosity of the rock than the previous calculations that used greater pore fluid resistivity values.

Cementation factors greater than 1 would require pore spaces that are less ellipsoidal and more spherical. This would not be likely in fractured rock but could be possible in a sedimentary basin such as the basin modeled by the gravity data. However, the density model from Witter (2022) suggests that the basin lies directly on top of C1 and thus it is unlikely that there is conducting pore fluid within the pore space of the basin. In addition, circulation of pore fluid within a fault zone is indicative of an active tectonic setting. This is seen in areas such as the San Andreas fault where electrically conductive structures associated with fluid circulation have been previously imaged using MT (Unsworth et al.,

1999; Bedrosian et al., 2002). The Tintina Fault is known to have very limited tectonic activity, with only an estimated 0.5 mm/yr current rate of slip (Leonard et al., 2008). The low activity would limit the amount of pore fluid circulation and restrict the likeliness of this explanation for the cause of the conductive structures imaged in the MT inversion models.

Thus saline pore fluids may be a possible explanation for the conductor, provided the salinity of the fluid is sufficiently high and there is enough activity along this area of the fault zone to allow for fluid circulation. In addition, a lack of pore fluids does not completely discount the possibility of further geothermal production. As outlined in Section 3.4, an engineered geothermal system may be a viable option so long as sufficient heat is present.

7.4.2 Graphite Films

The second possibility is that the conducting body is the result of a conducting phase, such as graphite films, that have been deposited in the rocks of C1. The graphite would have lower resistivity values than the surrounding rock, thus appearing as a conductor in the inversion model. This would be similar to the conclusion of Ledo et al., (2002), in their previous MT study of the Tintina Fault. Graphite deposits can be smeared due to motion along the fault resulting in a zone of interconnected graphite films which greatly lowers the measured resistivity of the rock (Ritter et al., 1999).

Archie's Law can also be utilized to estimate the amount of graphite needed to explain the low resistivity areas. To explain the low resistivity area, graphite deposits would need to be composed of an interconnected film of deposits. Thus, the cementation factor required in Archie's Law must equal 1 to account for the distribution of the graphite films. From Palacky (1988), it can be seen that graphite has an electrical resistivity range of 0.1-10 Ωm, and the conductor C1 has a resistivity range of 1-10 Ωm. Using these values, the volume fraction of graphite films is estimated to be in the range of 0.01 – 0.1 (Figure 7.5). These values of graphite concentration are reasonable for the expected host rock, making graphite films a potential candidate to explain the conducting features.

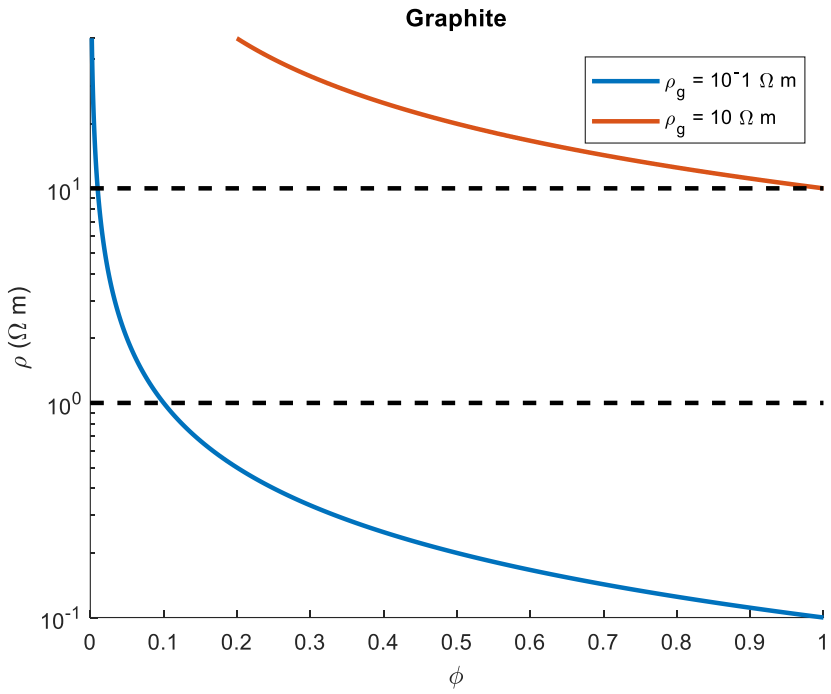

Figure 7.5: Plot of resistivity as a function of porosity following Archie's Law for host rock containing interconnected graphite films.

7.4.3 Sulphide Minerals

Deposits containing economically significant concentrations of sulphide minerals have been identified further north-west along the Tintina Fault at Faro. It is possible that rocks containing sulphide mineral deposits have been transported by fault movement south-east to the Watson Lake area. These rock units would be characterized by low values of electrical resistivity, making them identifiable in the inversion model. A study by Nelson and Van Voorhis (1983) details the relationship between the measured electrical resistivity and weight percent concentration of sulphide minerals. Using the results of their study, in order to explain the modelled resistivity of 1-10 Ωm of conductor C1, the percent concentration of sulphides would need to be in excess of 10% (Figure 7.6). Due to the density contrast between sulphides and the host rock, a deposit of this size would be easily imaged by gravity data.

Massive sulphide minerals can range in density from 4 g/cm^3 (Sphalerite) to 7.5 g/cm^3 (Galena) (Morgan, 2012), thus a rock consisting of 10% sulphides by weight would have a density ranging from 2.76 g/cm^3 to 2.85 g/cm^3 (assuming an average crustal density of 2.67 g/m^3) which for a 1km thick layer of sulphides would produce a Bouguer gravity correction ranging from 0.116 – 0.119 mGal, which would produce a

positive Bouguer gravity anomaly. The gravity model of the study area from Witter (2022) does not display any density anomalies that would be consistent with concentrations of sulphide minerals in this range and the density modelled for the area where the conductor is located ranges from 2.65 – 2.75 g/cm^3, which is below the required range for the sulphide mineral explanation. Thus, it is unlikely that the conductors can be readily explained by the presence of sulphide minerals.

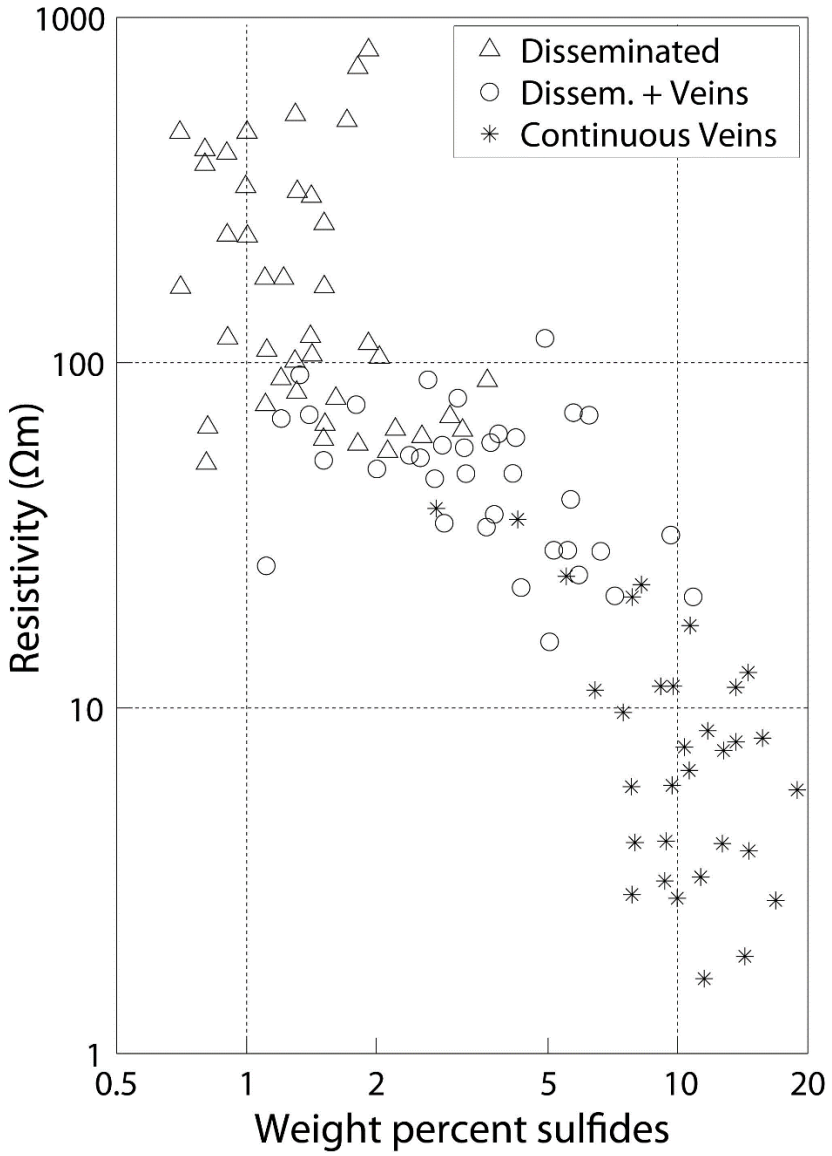

Figure 7.6: Plot of resistivity as a function of weight percent sulphide concentration (Modified from Nelson and Van Voorhis, 1983).

7.4.4 Hydrothermal Clay Alteration

The fourth explanation is a zone of clay alteration caused by local hydrothermal activity. Hydrothermal alteration will cause a clay cap composed of illite and smectite to form above a layer of hot pore fluid (Ussher et al. 2000) (Figure 7.7). Hydrothermal clay alteration occurs when hot circulating fluid, typically heated from volcanic sources, interacts with the host rock to form clay minerals. The clay minerals form a clay cap composed mainly of conducting clays such as smectite and illite. These clays have very low values of electrical resistivity, making the clay cap easily detectable with the MT method. Typically, smectites will form at shallower depths with reservoir temperatures less than 200°C, temperature ranges from approximately 200 – 300 °C will mainly contain illite, and a zone of interlayered smectite and illite will typically be found in between these two zones at reservoir temperatures between 100 – 200°C (Ussher et al., 2000). The measured resistivity values of conductor C1 are consistent with typical values of smectite, making a clay cap formed by hydrothermal processes a possible candidate. A limiting factor for this explanation is the requirement of volcanism or active tectonism in the area to drive the hydrothermal alteration. There is no current active volcanism in the study area and research indicates that the Tintina Fault is currently inactive and experiencing very little movement (Leonard et al., 2008), which would limit this as a possibility. It is possible that a clay cap could have been formed as the result of upward fluid flow within the Tintina Fault when it was previously active, similar to fluid movement seen along the San Andreas and Sumatra faults (Hochstein and Sudarman, 1993; Unsworth et al., 1999; Bedrosian et al., 2002; Muraoka et al., 2010). In these systems, the fault movement allows for more circulation of pore fluids as it ensures that fractures within the rock remain open. In an inactive setting, the fractures may close, inhibiting the flow of fluids. It is possible that fluid flow from when the Tintina Fault was previously active resulted in the creation of a clay cap which remained in place after the fault activity subsided. In this case the presence of a clay cap does not necessarily indicate the presence of trapped fluids beneath the clay. It has been shown that the low resistivity clay layer prevents the MT method from properly imaging the reservoir below (Pellerin et al., 1996). This means that it is possible that the fluid responsible for forming the clay cap may no longer be situated in a reservoir below.

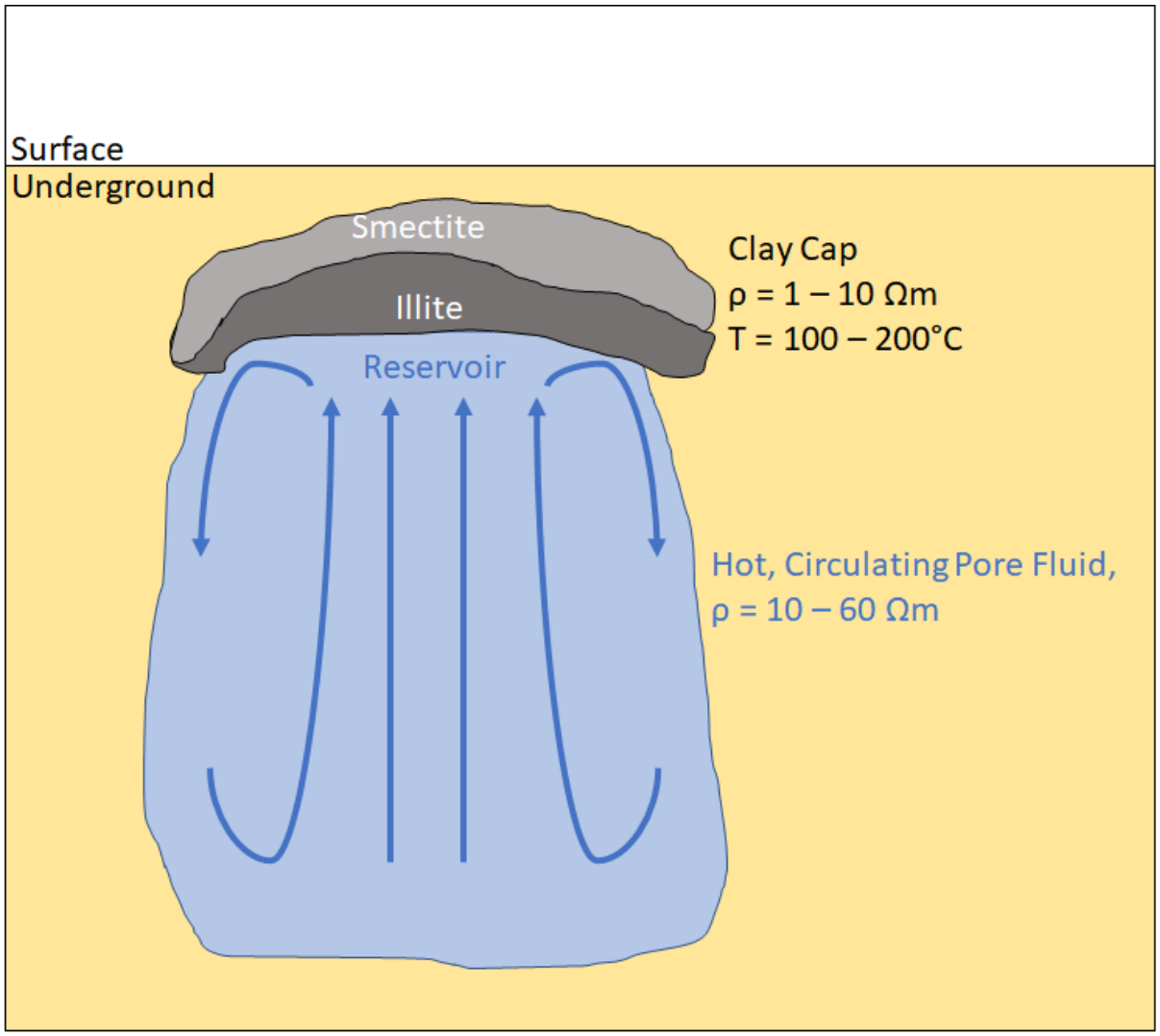

Figure 7.7: Diagram showing the Smectite – Illite clay cap formed by hydrothermal alteration in a geothermal system (Modified from Pellerin et al., 1996)

7.4.5 Preferred Explanation of the Conductor

From the possible explanations above, the most likely explanations for the conducting feature C1 are saline pore fluids or graphite films located within the fault zone. Saline pore fluids with sufficiently high values of TDS would greatly reduce the electrical resistivity of the rock. This explanation is limited by the results of the gravity data analysis, which suggests the conducting body must lie below the modelled sedimentary basin, as well as the reduced activity of the Tintina Fault zone. The Tintina Fault is known have low values of annual movement (Leonard et al., 2008), which would limit fluid circulation. The low resistivities of graphite films are also consistent with the modelled conducting feature, and the low

porosity values required make this explanation reasonable. The hydrothermal clay cap is also a potential explanation but is limited by the lack of volcanism and active fault movement in the area. It may have been formed while the fault was active by fluids flowing upward along the fault, which may continue in the present. However, as discussed previously, fluid flow is uncommon along inactive faults such as the Tintina Fault. Sulphides are the least likely explanation for the conductors. The gravity data limits the possibility of sulphides being responsible for the low resistivity of the feature, as the concentration of sulphide minerals necessary to explain the low resistivity would appear as a positive Bouguer anomaly, which is not seen in the gravity model.

7.5 Constraining the Location of the Tintina Fault Zone

The location and orientation of the Tintina Fault zone in the study area is poorly constrained due to glacial overburden. The fault location is important for geothermal exploration as it would provide the fractured, permeable rock necessary for the development of a conventional geothermal plant to be feasible. Previous studies (Ledo et al., 2002) along the fault, north of the study area have determined that the strike direction of the fault is between N45°W and N50°W. From the results of the data analysis and inversion models, a better estimate for the location and orientation of the Tintina Fault zone at Watson Lake has been obtained.

From the results of the MT data inversions, resistors R1 and R2 are likely to be associated with strands of the fault zone. This would place the Tintina Fault further West of Watson Lake than it is shown in some maps (Yukon Geological Survey, 2022; Mortensen and Murphy, 2005). The location can also be better determined from the phase tensor plots in section 5.9.1. In the phase tensor plots (Figures 5.7, 5.8, 5.9, and 5.10), it is seen that below a frequency of 0.08 Hz the phase tensors plotted East of 129°W begin to change their preferred orientation. This change in strike is indicative of crossing a boundary of changing resistivity which is interpreted as the boundary of the fault zone. This location coincides with the location of the resistors R1 and R2. Furthermore, the phase tensor data also indicates a preferred strike orientation of between N45°W and N30°W in this area. In the horizontal cross-sections of the inversion model (Figure 7.1), R1 and R2 appear to extend in this direction as well. Northwest of the main survey area, the model is less constrained due to a lack of stations in the area, but the resistors can be extrapolated to extend to the Northwest. From this, it is proposed that the Tintina Fault zone is located further West of the community of Watson Lake, with a strike of between N45°W and N30°W. Figure 7.8 provides a comparison between the currently accepted fault trace (TF Old) from the map of bedrock

geology (Yukon Geological Survey, 2022) and two boundary fault strands extrapolated from the locations of resistors R1 and R2 (TF1 and TF2). The new proposed location for the fault trace is also consistent with that proposed by the gravity data (Witter, 2022).

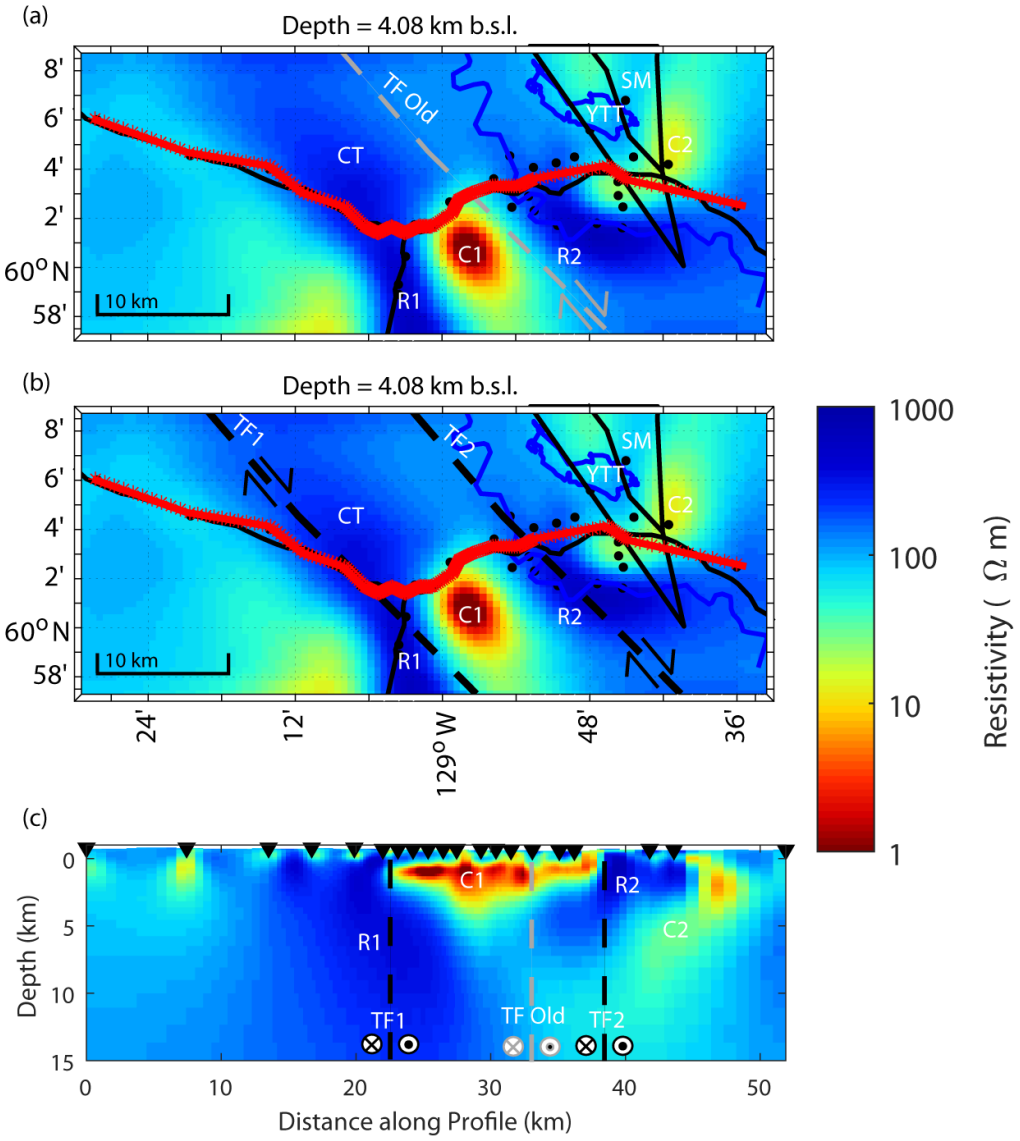

Figure 7.8: Comparison of the current Tintina Fault trace and proposed boundaries of the fault zone. (a) displays the current location of the Tintina Fault trace (TF Old) superimposed on the inversion model at a depth of 4.08 km b.s.l. (Yukon Geological Survey, 2022). (b) displays proposed boundaries for the Tintina Fault zone interpreted from the MT inversion model (TF1 and TF2) at a depth of 4.08 km b.s.l. (c) shows a vertical slice of the MT inversion model with the locations of the aforementioned fault traces plotted.

7.6 Conclusions

The conducting features C1 and C2 imaged in the inversion model are best explained as either saline pore fluids or interconnected graphite films within the fractures of rock units present within the fault zone. The low resistivity of the pore fluids or graphite would lower the overall resistivity of the host rock, resulting in the conducting features. The resistors R1 and R2 appear to be fault strands within the fault zone. These strands lie further west than the currently accepted trace of the Tintina Fault and have a strike of between N45°W and N30W°.

Chapter 8: Conclusions

8.1 Introduction

Geothermal energy has the potential to replace diesel and other fossil fuel burning power plants as the primary source of electricity and heat for many communities in northern Canada. This form of energy generation produces minimal carbon emissions and does not require specific weather conditions to operate as in the case of wind and solar power. This would be an ideal form of electricity production for remote, northern Canadian communities which presently rely on fuel shipments from the southern parts of the country to generate electricity and heat.

The community of Watson Lake may be a potential site for the development of geothermal energy, either for direct use of the heat or for electricity production. To be feasible for geothermal energy development, an area must have (1) sufficiently high subsurface temperatures, (2) fluids to extract the heat, and (3) the host rock must be sufficiently permeable allow fluid flow and to enable fluid extraction. A previous study by Majorowicz and Grasby (2014) showed that the Watson Lake area has a relatively high geothermal gradient with heat flow values of approximately 100 – 110 mW/m^2 and estimated temperatures of approximately 80 – 90°C at a depth of 2 km, increasing to approximately 200 – 240°C at 6 km below the surface. If suitable fluids were present and the host rock had sufficient permeability, then additional geothermal exploration and development could be considered. To determine if these conditions are met for Watson Lake, further geological and geophysical studies such as those discussed in this thesis are required. The community is located in the vicinity of the Tintina Fault, which may provide a source of fractured, permeable rock suitable for pore fluid circulation. Due to glacial till coverage, the exact location of the southern extent of the Tintina Fault is poorly constrained. The new MT data collected during the summer 2021 survey was utilized to create a 3D resistivity model of the area, which was used to identify targets for geothermal development. The main results of the 3D model are outlined below, along with potential suggestions for future work.

8.2 Summary of 2021 MT Data and Inversion Model

Broadband MT data was collected at 36 stations in the frequency range of 0.001 – 100 Hz. From skin depth calculations, this gives an approximate depth of penetration of 160 km (assuming a uniform 100 Ωm Earth).

The phase tensor data showed that the collected MT data were primarily 3D and the orientation of the phase tensor data in the frequency range of 0.08-12 Hz shows a strong preferential strike direction between N45°W and N30°W. A change in alignment of the phase tensor data below a frequency of 0.08 Hz for stations on the portion of the survey grid east of 129°W of Longitude indicates that this represents a boundary of a conducting body. From this observation, the Tintina Fault is interpreted to lie at approximately 129°W with a strike direction of between N45°W and N30°W.

The 3D inversion model is characterized by a large conducting region (C1) with resistivity in the range of 1 – 10 Ωm. This feature extends from a depth of 500 m to a depth of 3 km and has a width of approximately 15 km. It is bounded on either side by resistors R1 and R2, which have resistivity ranges of 300 – 1000 Ωm and widths of 10 km and 6 km respectively. R2 separates C1 and the second conductor C2, which has a resistivity range of 10 – 30 Ωm, width of 3 km, and is situated between 500 m to 10 km below sea level.

8.3 Model Interpretation

The preferred inversion model displays four main features of interest: two conductive bodies (C1 and C2), and two resistive bodies (R1 and R2). After analysis of the electrical resistivity of the features and considering the geological context of the area, the identities of these features are interpreted as follows: Conductors C1 and C2 are most likely caused by either saline pore fluids, or the presence of interconnected graphite films within fractures in the host rock. Saline pore fluids with electrical resistivities ranging from 0.03 – 3 Ωm would require rock porosities of at least 0.18%, making this a very reasonable explanation. For the graphite film explanation to be valid, the rock must contain 1 – 10% graphite by volume. The graphite films would be the result of past fault movement causing previously deposited graphite units to smear, and form interconnected films with characteristically low electrical resistivity.

Resistors R1 and R2 are interpreted as strands of the Tintina Fault zone. The location and orientation of R1 and R2 are consistent with the location and orientation of the fault in some studies and maps (Mortensen and Murphy, 2005; Witter, 2022; Yukon Geological Survey, 2022), and with the location and orientation of the fault as interpreted from the phase tensor data.

8.4 Implications for Geothermal Exploration and Development at Watson Lake

As stated above, the analysis of the MT inversion model suggests that the conducting bodies in the cross-section are most readily explained as being due to either a layer of saline pore fluids or a block of rock containing previously deposited interconnected graphite films. However, this does not entirely discount the possibility of other potential explanations such as a clay cap formed through hydrothermal alteration. The presence of a layer of saline pore fluids would be significant for further geothermal development as they would provide a way to extract the subsurface heat necessary for electricity and heat production. The presence of graphite instead of a reservoir of saline pore fluid would limit the potential for the development of a traditional geothermal system, however this does not necessarily mean that a geothermal project is unfeasible. If the fractured rock along the fault zone has sufficient permeability, and if the geothermal gradient was acceptable for electricity production, then a form of enhanced geothermal system or closed loop system may be viable alternatives to a traditional geothermal generating plant. If an enhanced geothermal system is commissioned for the area, seismic monitoring will need to be utilized to detect any earthquakes that may be induced from fluid injection along the fault zone.

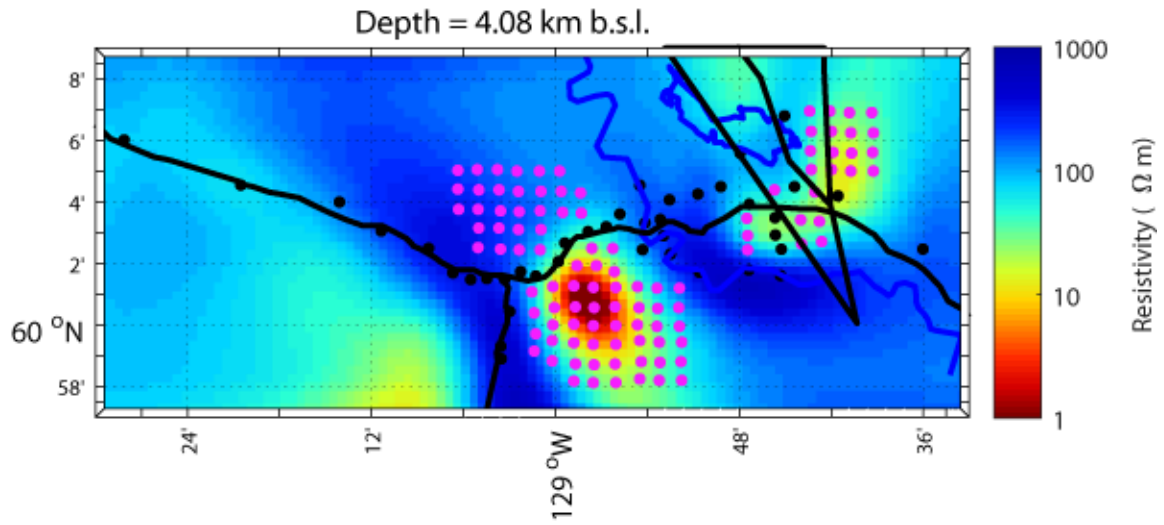

Figure 8.1: Horizontal slice from the inversion model at a depth of 4.08 km b.s.l. displaying locations of current stations (black circles) and proposed future stations (purple circles) (Note this is an ideal proposal and that some of the proposed stations may be in inaccessible locations)..

8.5 Future Work

To improve the resolution of the subsurface resistivity structure, the MT survey grid could be extended to better constrain the location of the Tintina Fault zone and the conducting features imaged in the

inversion. This would require additional MT stations that would be deployed in a second survey. The current grid of MT stations could be expanded to include more stations North and South of the current grid. Specifically, more stations between the Liard River and Junction 37 would help to determine the lateral extent of the conductor C1. Additional stations North-West of the survey grid would better constrain the fault zone location. Figure 8.1 provides an optimistic proposal for a future grid of MT stations, however many of the proposed site locations would be difficult to access, making the deployment difficult and potentially expensive. Even so, the collection of some of the proposed stations would greatly constrain the conductor locations and geometry. This would help to better identify a potential site to drill a test well where temperature gradient could be measured. It is possible that the conductor could be a crustal block bounded by strands of the Tintina Fault. If this is the case, it would help to constrain potential drill targets for future test wells. For example, a test well could be drilled near the junction of Highway 37 and the Alaska Highway. The conductor in this area is well constrained by the station data and thus a test well drilled at this location would allow for a more detailed interpretation of the results of the MT and gravity data analysis.

According to the phases of geothermal exploration outlined by Hickson and Yehia (2014), the next phase in the project after target identification would be to evaluate the prospective resource at Watson Lake. This would involve more detailed studies of heat flow and rock permeability in the area. Test wells would also need to be utilized to sample and test pore fluid (if any is present), as well as to measure the thermal gradient before further determining the feasibility of developing a geothermal plant in the area.

References

Archie, G.E. (1942). The electrical resistivity log as an aid in determining some reservoir characteristics. *Transactions of the AIME, 146*(01), 54-62. https://doi.org/10.2118/942054-G

Barbier, E. (2002). Geothermal energy technology and current status: an overview. *Renewable and sustainable energy reviews 6.1-2*: 3-65. https://doi.org/10.1016/S1364-0321(02)00002-3

Becken, M. & Ritter, O., (2012). Magnetotelluric studies at the San Andreas Fault Zone: implications for the role of fluids. *Surveys in Geophysics*, *33*, 65-105. https://doi.org/10.1007/s10712-011-9144-0

Bedrosian, P.A., Unsworth, M.J., Egbert, G. (2002). Magnetotelluric imaging of the creeping segment of the San Andreas Fault near Hollister. *Geophysical Research Letters 29*(11), 1-1-1-4. https://doi.org/10.1029/2001GL014119

Block, D. (2001). Water resistivity atlas of western Canada. *Canadian Society of Petroleum Geologists, Rock the Foundation Convention Paper*. 88: 359-369

Booker, J.R. (2014). The magnetotelluric phase tensor: a critical review. *Surveys in Geophysics, 35*, 7-40. https://doi.org/10.1007/s10712-013-9234-2

Brown, D.W. (2000). A hot dry rock geothermal energy concept utilizing supercritical CO2 instead of water. *Proceedings of the twenty-fifth workshop on geothermal reservoir engineering, Stanford University*. https://pangea.stanford.edu/ERE/pdf/IGAstandard/SGW/2000/Brown.pdf

Cagniard, L. (1953). Basic Theory of the Magneto-telluric Method of Geophysical Prospecting. *Geophysics. 18:* 605-635. https://doi.org/10.1190/1.1437915

Caldwell, T.G., Bibby, H.M., Brown, C. (2004). The Magnetotelluric Phase Tensor. *Geophys. J. Int*. 158: 457-469. https://doi.org/10.1111/j.1365-246X.2004.02281.x

Canada Energy Regulator. (2023, March 03). Provincial and territorial energy profiles-Canada. https://www.cer-rec.gc.ca/en/data-analysis/energy-markets/provincial-territorial-energy-profiles/provincial-territorial-energy-profiles-canada.html#:~:text=More%20than%20half%20of%20the,and%20petroleum%20(Figure%202)

Chen, J., Hoversten, G.M., Key, K., Nordquist, G. and Cumming, W., (2012). Stochastic inversion of magnetotelluric data using a sharp boundary parameterization and application to a geothermal site. *Geophysics*, *77*(4), E265-E279. https://doi.org/10.1190/geo2011-0430.1

Colpron, M., Gladwin, K., Johnston, S.T., Mortensen, J.K., Gehrels, G.E. (2005). Geology and juxtaposition history of the Yukon– Tanana, Slide Mountain, and Cassiar terranes in the Glenlyon area of central Yukon. *Canadian Journal of Earth Sciences; 42 (8),* 1431–1448. https://doi.org/10.1139/e05-046

Cook, F.A., Clowes, R.M., Snyder, D.B., van der Velden, A.J., Hall, K.W., Erdmer, P., & Evenchick, C.A. (2004). Precambrian crust beneath the Mesozoic northern Canadian Cordillera discovered by Lithoprobe seismic reflection profiling. *Tectonics, 23*(2). https://doi.org/10.1029/2002TC001412

Dickinson, W.R. (2004). Evolution of the North American cordillera. *Annu. Rev. Earth Planet. Sci. 32:* 13-45. https://doi.org/10.1146/annurev.earth.32.101802.120257

Duchane, D. & Brown, D. (2002). Hot dry rock (HDR) geothermal energy research and development at Fenton Hill, New Mexico. *Geo-Heat Centre Quarterly Bulletin*, *23*. https://citeseerx.ist.psu.edu/document?repid=rep1&type=pdf&doi=1f928da4da5165a9c02c81f5c2e0caaabadcfe9f

Eavor Technologies Inc. (2023a). Eavor-Lite. Calgary (AB): Eavor Technologies Inc. Retrieved February 13, 2023, from https://www.eavor.com/eavor-lite/

Eavor Technologies Inc. (2023b). Eavor-Deep. Calgary (AB): Eavor Technologies Inc. Retrieved February 13, 2023, from https://www.eavor.com/eavor-deep/

Egbert, G.D. (1997). Robust multiple-station magnetotelluric data processing. *Geophysical Journal International*, 130(2), 475-496. https://doi.org/10.1111/j.1365-246X.1997.tb05663.x

Ellsworth, W.L., Giardini, D., Townend, J., Ge, S., Shimamoto, T. (2019). Triggering of the Pohang, Korea, Earthquake (M_w 5.5) by Enhanced Geothermal System Stimulation. *Seismological Research Letters 90(5),* 1844-1858. https://doi.org/10.1785/0220190102

Finley, T.D., Johnston, S.T., Unsworth, M.J., Banks, J., Pana, D.I. (2022). Modern dextral strain controls active hydrothermal systems in the southeastern Canadian Cordillera. *Geological Society of America Bulletin*. https://doi.org/10.1130/B36500.1

Fridleifsson, I.B. (2001). Geothermal energy for the benefit of the people. *Renewable and sustainable energy reviews 5(3),* 299-312. https://doi.org/10.1016/S1364-0321(01)00002-8

Gabrielse, H., Murphy, D.C., Mortensen, J.K. (2006). Cretaceous and Cenozoic dextral orogen-parallel displacements, magmatism, and paleogeography, north-central Canadian Cordillera. *Paleogeography of the North American Cordillera: Evidence For and Against Large-Scale Displacements: Geological Association of Canada Special Paper 46*: 255-276. https://www.researchgate.net/profile/James-Mortensen/publication/285873017_Cretaceous_and_Cenozoic_dextral_orogen-parallel_displacements_magmatism_and_paleogeography_north-central_Canadian_Cordillera/links/5864609208ae8fce490b7526/Cretaceous-and-Cenozoic-dextral-orogen-parallel-displacements-magmatism-and-paleogeography-north-central-Canadian-Cordillera.pdf

Gamble, T.D., Goubau, W.M., Clarke, J. (1979). Magnetotellurics with a remote magnetic reference. *Geophysics, 44(1)*, 53-68. https://doi.org/10.1190/1.1440923

Government of Yukon. (2018). *Yukon's energy context*. https://yukon.ca/sites/yukon.ca/files/emr/emr-yukon-energy-context.pdf

Government of Yukon. (2019). *Yukon Observation Well Network 2017 Report*. https://yukon.ca/sites/yukon.ca/files/env/env-yukon-observation-well-network-2017-report.pdf

Government of Yukon. (2022). *Population Report First Quarter, 2022*. https://yukon.ca/sites/yukon.ca/files/ybs/fin-population-report-q1-2022.pdf

Grasby, S.E., Allen, D.M., Bell, S., Chen, Z., Ferguson, G., Jessop, A., Kelman, M., Ko, M., Majorowicz, J., Moore, M., et al. (2012) Geothermal energy resource potential of Canada, *Geological survey of Canada, Open file 6914 (revised),* 322p. https://doi.org/10.4095/291488

Hickson, C.J., Yehia, R. (2014). The geothermal exploration and development process: graphical representation path to optimal decision making. *Geothermal Resources Council, Transactions 38*: 377-380. https://publications.mygeoenergynow.org/grc/1033563.pdf

Hochstein, M.P. and Sudarman, S., (1993). Geothermal resources of Sumatra. *Geothermics*, *22*(3), 181-200. https://doi.org/10.1016/0375-6505(93)90042-L

Johnston, S. T. (2008). The cordilleran ribbon continent of North America. *Annu. Rev. Earth Planet. Sci., 36,* 495-530. https://doi.org/10.1146/annurev.earth.36.031207.124331

Jones, A. G., & Spratt, J. (2002). A simple method for deriving the uniform field MT responses in auroral zones. *Earth, Planets and Space, 54(5),* 443-450. https://www.researchgate.net/profile/Alan-Jones-13/publication/229010346_A_simple_method_for_deriving_the_uniform_field_MT_responses_in_auroral_zones/links/5523d2a40cf24f1609437ca4/A-simple-method-for-deriving-the-uniform-field-MT-responses-in-auroral-zones.pdf

Kelbert, A., Meqbel, N., Egbert, G.D., Tandon, K. (2014). ModEM: A modular system for inversion of electromagnetic geophysical data. *Computers & Geosciences*, *66*: 40-53. https://doi.org/10.1016/j.cageo.2014.01.010

Kraft T., Mai P.M., Wiemer S., Deichmann N., Ripperger J., Kästli P., Bachmann C., Fäh D., Wössner J., Giardini D. (2009). Enhanced Geothermal Systems: Mitigating Risk in Urban Areas. *Eos, Transactions America Geophysical Union, 90(32)*, 273-274. https://doi.org/10.1029/2009EO320001

Ledo J., Jones A.G., Ferguson I.J. (2002). Electromagnetic images of a strike-slip fault: The Tintina Fault-Northern Canadian. *Geophysical Research Letters*. *29(8)*, 66-1 – 66-4. https://doi.org/10.1029/2001GL013408

Ledo J., Jones A.G., Ferguson I.J., and Wolynec L. (2004). Lithospheric structure of the Yukon, northern Canadian Cordillera, obtained from magnetotelluric data, *J. Geophys. Res., 109*, B04410. https://doi.org/10.1029/2003JB002516

Leonard, L.J., Mazzotti, S., and Hyndman, R.D. (2008). Deformation rates estimated from earthquakes in the northern Cordillera of Canada and eastern Alaska. *Journal of Geophysical Research: Solid Earth, 113*(B8). https://doi.org/10.1029/2007JB005456

Lund, J. W., Freeston, D. H., & Boyd, T. L. (2005). Direct application of geothermal energy: 2005 worldwide review. *Geothermics*, 34(6), 691-727. https://doi.org/10.1016/j.geothermics.2005.09.003

Majorowicz, J. & Grasby, S.E. (2014). Geothermal energy for northern Canada: is it economical?. *Natural resources research.* 23(1), 159-173. https://doi.org/10.1007/s11053-013-9199-3

Mazzotti, S. & Hyndman, R.D. (2002). Yakutat collision and strain transfer across the northern Canadian Cordillera. *Geology*, *30*(6), 495-498. https://doi.org/10.1130/0091-7613(2002)030<0495:YCASTA>2.0.CO;2

Monger, J. W. H. (1989). Overview of Cordilleran geology. In *Western Canada Sedimentary Basin: A Case History* (pp. 9-32). Canadian Society of Petroleum Geologists. https://archives.datapages.com/data/cspg_sp/data/CSPG-SP-011/011001/9_cspgsp110009.htm

Monger, J. & Price, R. (2002). The Canadian Cordillera: geology and tectonic evolution. *CSEG Recorder* 27(2), 17-36. https://www.researchgate.net/profile/Raymond-Price-5/publication/305775923_The_Canadian_Cordillera_Geology_and_Tectonic_Evolution/links/57a0f78108aeb1604832b78b/The-Canadian-Cordillera-Geology-and-Tectonic-Evolution.pdf

Monger, J.W.H. and Irving, E. (1980). Northward displacement of north-central British Columbia. *Nature*, *285*(5763), 289-294. https://doi.org/10.1038/285289a0

Morgan, L.A. (2012). Geophysical characteristics of volcanogenic massive sulfide deposits. *USGS, 7,* 115-131. https://www.researchgate.net/profile/L-Morgan-2/publication/272830514_Geophysical_Characteristics_of_Volcanogenic_Massive_Sulfide_Deposits/links/54f0eaaa0cf24eb87941629d/Geophysical-Characteristics-of-Volcanogenic-Massive-Sulfide-Deposits.pdf

Mortensen, J.K. and Murphy, D.C. (compilers). (2005). Bedrock geological map of part of Watson Lake area (all or part of NTS 105A/2, 3, 5, 6, 7, 10, 11, 12, 13, 14), southeastern Yukon. *Yukon Geological Survey, Open File 2005-10*, scale 1:50000. https://data.geology.gov.yk.ca/Reference/42771#InfoTab

Munoz, G. (2014). Exploring for geothermal resources with electromagnetic methods. *Surveys in geophysics, 35*, 101-122. https://doi.org/10.1007/s10712-013-9236-0

Muraoka, H., Takahashi, M., Sundhoro, H., Dwipa, S., Soeda, Y., Momita, M. and Shimada, K. (2010, April). Geothermal systems constrained by the Sumatran fault and its pull-apart basins in Sumatra, western Indonesia. In *Proceedings World Geothermal Congress* (pp. 1-9). https://www.geothermal-energy.org/pdf/IGAstandard/WGC/2010/1248.pdf

Natural Resources Canada. (2022). *Heating equipment for residential use*. Retrieved 2022 Oct. 18 from https://www.nrcan.gc.ca/energy-efficiency/products/heating-equipment-for-residential-use/13740

Nelson, P.H. & Van Voorhis, G.D. (1983). Estimation of sulfide content from induced polarization data. *Geophysics*. *48(1),* 62-75. https://doi.org/10.1190/1.1441408

Nesbitt, B. E. (1993). Electrical resistivities of crustal fluids. *Journal of Geophysical Research: Solid Earth, 98(B3)*, 4301-4310. https://doi.org/10.1029/92JB02576

Olasolo, P., Juárez M.C., Morales M.P., D'Amico S., Liarte I.A. (2016). Enhanced geothermal systems (EGS): A review. *Renewable and Sustainable Energy Reviews* 56, 133-144. https://doi.org/10.1016/j.rser.2015.11.031

Palacky, G.J. (1988). Resistivity characteristics of geologic targets. *Electromagnetic methods in applied geophysics*, *1*, 52-129.

Parker, R.L. (1980). The inverse problem of electromagnetic induction: Existence and construction of solutions based on incomplete data, *J. Geophys. Res., 85(B8),* 4421– 4428. https://doi.org/10.1029/JB085iB08p04421

Pellerin, L., Johnston, J.M., Hohmann, G.W. (1996). A numerical evaluation of electromagnetic methods in geothermal exploration. *Geophysics*. *61(1*), 121-130. https://doi.org/10.1190/1.1443931

Richter, A. (2022, Jan 10). ThinkGeoEnergy's Top 10 Geothermal Countries 2021 – installed power geration capacity (Mwe). ThinkGeoEnergy. https://www.thinkgeoenergy.com/thinkgeoenergys-top-10-geothermal-countries-2021-installed-power-generation-capacity-mwe/#:~:text=Here%20the%20Top%2010%20geothermal,98%20MW%20Rantau%20Dedap%20plants.

Ritter, O., Haak, V., Rath, V., Stein, E., and Stiller, M. (1999). Very high electrical conductivity beneath the Münchberg Gneiss area in Southern Germany: implications for horizontal transport along shear planes. *Geophysical Journal International, 139*(1), 161-170. https://doi.org/10.1046/j.1365-246X.1999.00937.x

Rodi, W., Mackie, R.L. (2001). Nonlinear conjugate gradients algorithm for 2-D magnetotelluric inversion. *Geophysics 66(1):* 174-187. https://doi.org/10.1190/1.1444893

Simpson, F. & Bahr, K. (2005). *Practical Magnetotellurics*. Cambridge: Cambridge University Press.

Tester, J. W., Anderson, B. J., Batchelor, A. S., Blackwell, D. D., DiPippo, R., Drake, E. M., ... & Toksoz, M. N. (2006). The future of geothermal energy. Massachusetts Institute of Technology, 358. https://naturalresources.house.gov/uploadedfiles/testertestimony04.19.07.pdf

Tietze, K. & Ritter, O. (2013). Three-dimensional magnetotelluric inversion in practice—the electrical conductivity structure of the San Andreas Fault in Central California. *Geophysical Journal International,* 195(1), 130-147. https://doi.org/10.1093/gji/ggt234

Tikhonov, A.N. (1950). On Determining Electrical Characteristics of the Deep Layers of the Earth's Crust. *Doklady. 73,2:* 295-297.

Umhoefer, P.J. (1987). Northward translation of "BAJA British Columbia" along the Late Cretaceous to Paleocene margin of western North America. *Tectonics*, *6*(4), 377-394. https://doi.org/10.1029/TC006i004p00377

Unsworth, M.J. (2019a). D1: Theory of magnetotellurics over a 1-D Earth. [GEOPH 424 course notes]

Unsworth, M.J. (2019b). D2: Theory of magnetotellurics over a 2-D Earth. [GEOPH 424 course notes].

Unsworth, M.J. (2019c). D3: Magnetotellurics – field techniques. [GEOPH 424 course notes].

Unsworth, M.J. (2019d). B: Resistivity of rocks and minerals. [GEOPH 424 course notes].

Unsworth, M.J., Egbert, G., Booker, J. (1999). High-resolution electromagnetic imaging of the San Andreas fault in Central California. *Journal of Geophysical Research 104*(B1): 1131-1150. https://doi.org/10.1029/98JB01755

Unsworth, M.J., Malin, P.E., Egbert, G.D., Booker, J.R. (1997). Internal structure of the San Andreas fault at Parkfield, California. *Geology*, *25*(4), 359-362. https://doi.org/10.1130/0091-7613(1997)025<0359:ISOTSA>2.3.CO;2

Ussher, G., Harvey, C., Johnstone, R., Anderson, E. (2000, May). Understanding the resistivities observed in geothermal systems. *In proceedings world geothermal congress* (pp. 1915-1920). Japan: Kyushu. http://www.lovegeothermal.org/pdf/IGAstandard/WGC/2000/R0279.PDF

Van Horn, A., Amaya, A., Higgins, B., Muir, J., Scherer, J., Pilko, R., & Ross, M. (2020). New opportunities and applications for closed-loop geothermal energy systems. *GRC Transactions*, *44*, 1123-1143.https://www.researchgate.net/profile/Andrew-Van-Horn/publication/344935261_New_Opportunities_and_Applications_for_Closed-Loop_Geothermal_Energy_Systems/links/621d25f29947d339eb70b9ec/New-Opportunities-and-Applications-for-Closed-Loop-Geothermal-Energy-Systems.pdf

Wang, C.L., Cheng, W.L., Nian, Y.L., Yang, L., Han, B.B., Liu, M.H. (2018). Simulation of heat extraction from CO2-based enhanced geothermal systems considering CO2 sequestration. *Energy 142*: 157-167. https://doi.org/10.1016/j.energy.2017.09.139

Wang, E., Unsworth, M.J., & Chacko, T. (2018). Geoelectric structure of the Great Slave Lake shear zone in northwest Alberta: implications for structure and tectonic history. *Canadian Journal of Earth Sciences*, *55*(3), 295-307. https://doi.org/10.1139/cjes-2017-0067

Witter, J.B. (2022). Analysis of Geoscience Data for Geothermal Exploration in Watson Lake, Yukon. *Yukon Geological Survey, Open File* 2022-8, 50 p. plus digital appendices. https://data.geology.gov.yk.ca/Reference/95965#InfoTab

Witter, J.B., Miller, C.A., Friend, M., Colpron, M. (2018). Curie point depths and heat production in Yukon, Canada. *Proceedings, 43rd Workshop on Geothermal Reservoir Engineering*. California. https://pangea.stanford.edu/ERE/pdf/IGAstandard/SGW/2018/Witter2.pdf

Wu, X., Ferguson, I.J. and Jones, A.G. (2002). Magnetotelluric response and geoelectric structure of the Great Slave Lake shear zone. *Earth and Planetary Science Letters*, *196*(1-2), 35-50. https://doi.org/10.1016/S0012-821X(01)00594-5

Yin, Y., Unsworth, M.J., Liddell, M., Pana, D. and Craven, J.A. (2014). Electrical resistivity structure of the Great Slave Lake shear zone, northwest Canada: implications for tectonic history. *Geophysical Journal International*, *199*(1), 178-199. https://doi.org/10.1093/gji/ggu251

Yukon Geological Survey. (2020). A digital atlas of terranes for the northern Cordillera. *Yukon Geological Survey,* Retrieved Sept 07, 2022, from https://data.geology.gov.yk.ca/Compilation/2

Yukon Geological Survey. (2022). Yukon digital bedrock geology. *Yukon Geological Survey*, Retrieved March 01, 2023, from https://data.geology.gov.yk.ca/Compilation/3

Appendix A: Apparent Resistivity, Phase, and Tipper Curves for Watson Lake 2021 Stations

The following figures display the apparent resistivity, phase, and tipper curves for the MT data collected during the Watson Lake 2021 survey. The station names are listed as wl0xx, where "xx" is the station number. Stations with multiple data runs had their spectra data stacked to produce one data file for use in data analysis and inversions, these stations are indicated as wl0xxab, or wl0xxabc, with the letters "a", "b", and "c" indicating which data runs were used. Names with the format wl0xxRRyy, indicate that station wl0xx was processed using a remote reference with "yy" indicating the remote reference station number. Names ending in "coh" indicate that coherence sorting was used during processing.

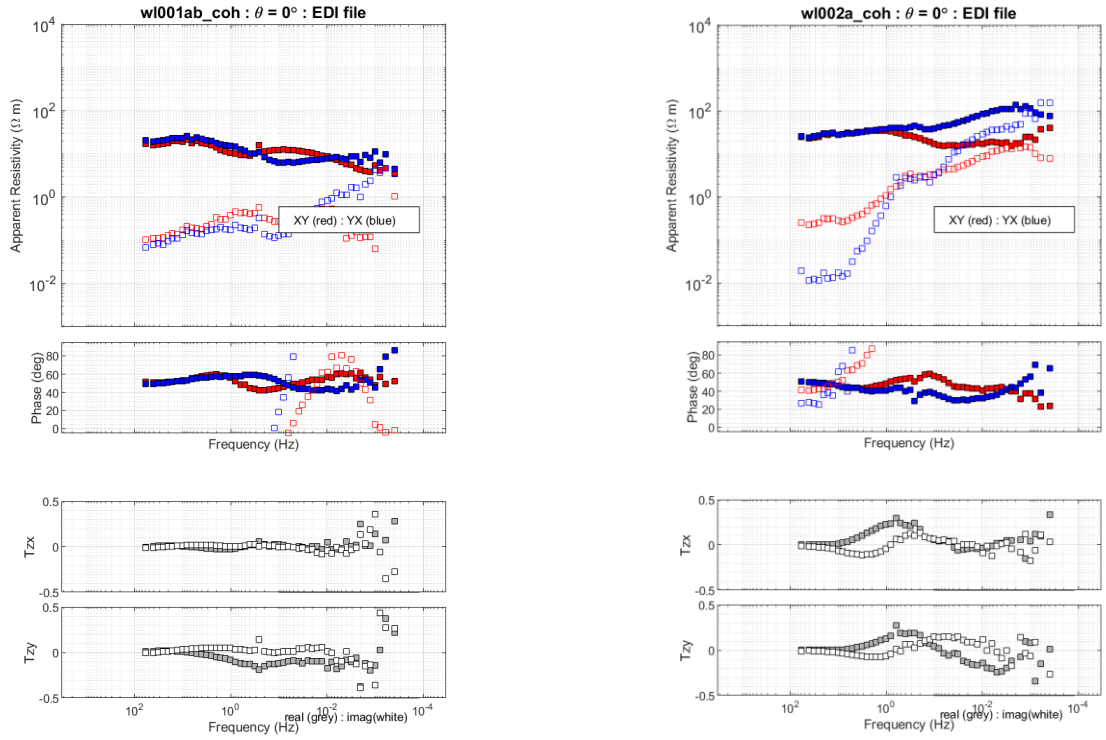

Figure A.1: Apparent resistivity, phase, and tipper curves for stations WL001 and WL002.

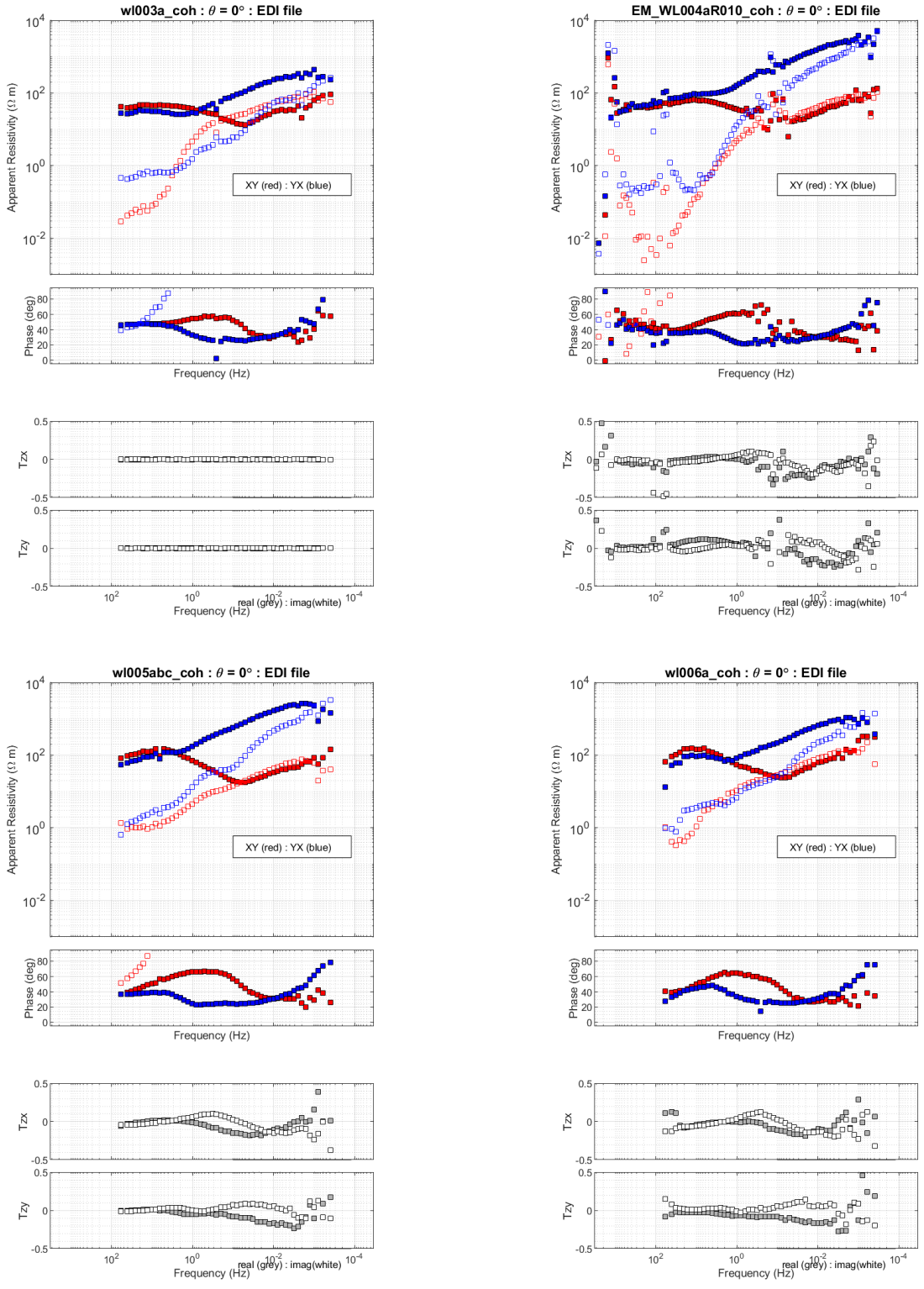

Figure A.2: Apparent resistivity, phase, and tipper curves for stations WL003, WL004, WL005, and WL006.

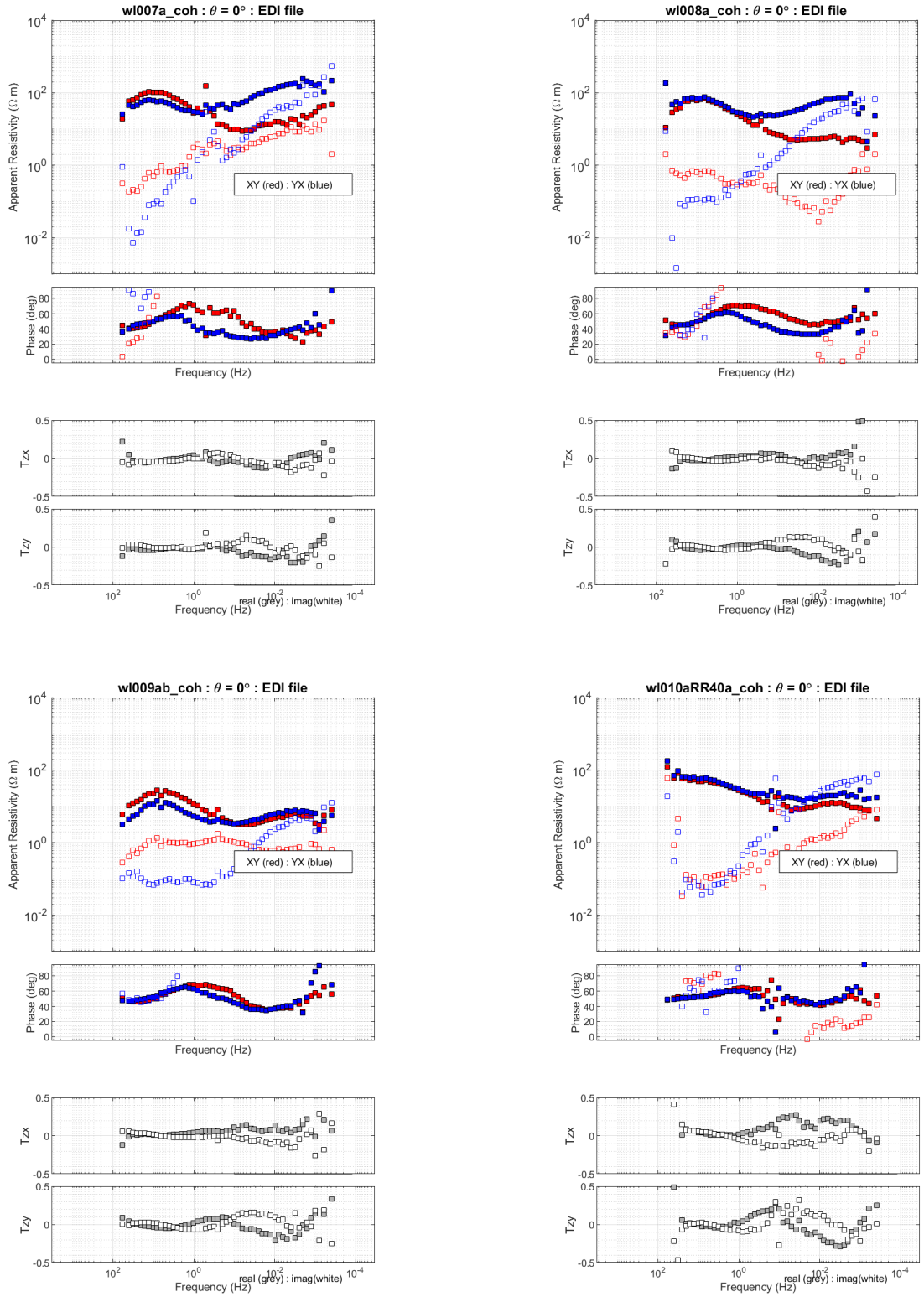

Figure A.3: Apparent resistivity, phase, and tipper curves for stations WL007, WL008, WL009, and WL010.

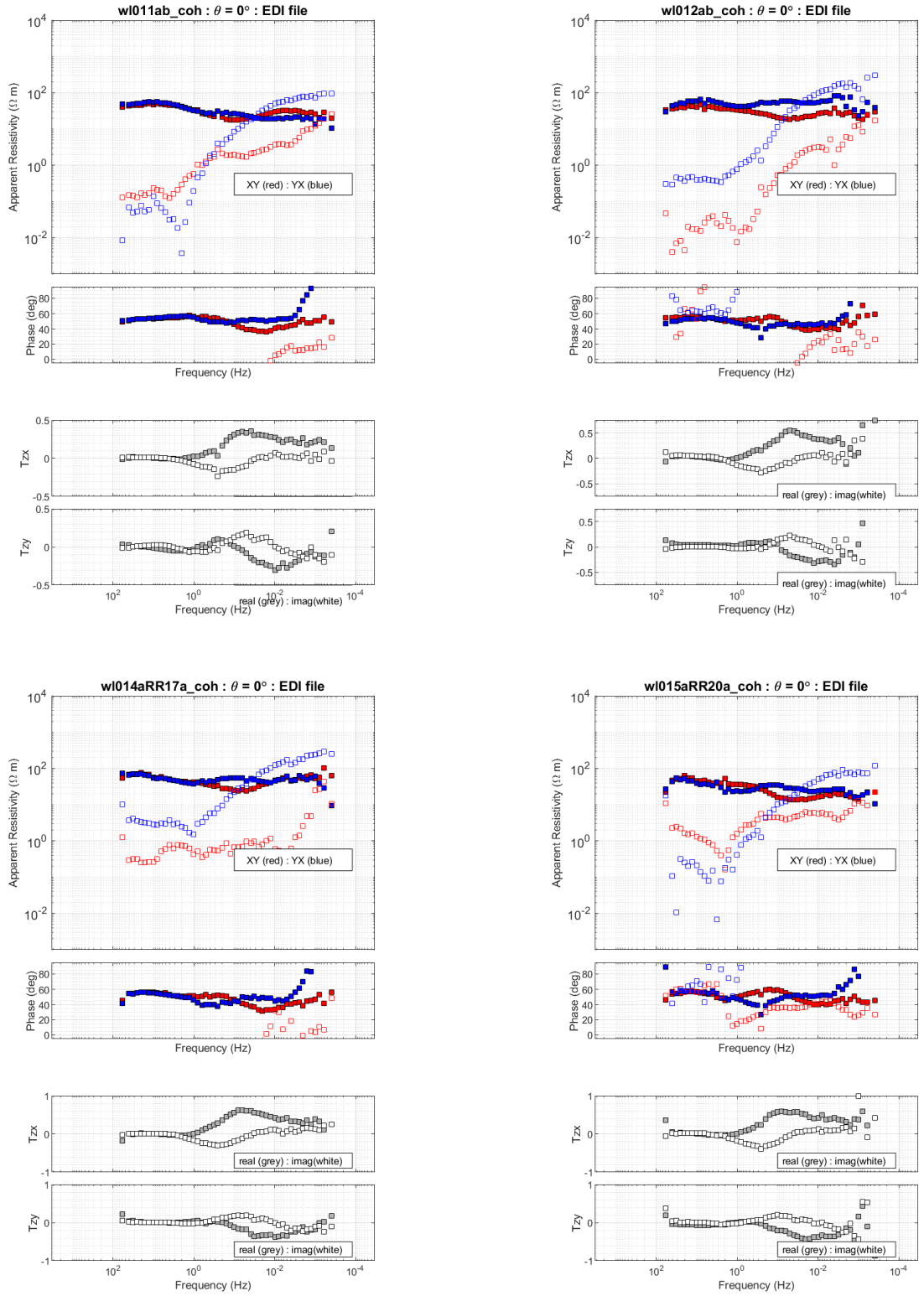

Figure A.4: Apparent resistivity, phase, and tipper curves for stations WL011, WL012, WL014, and WL015.

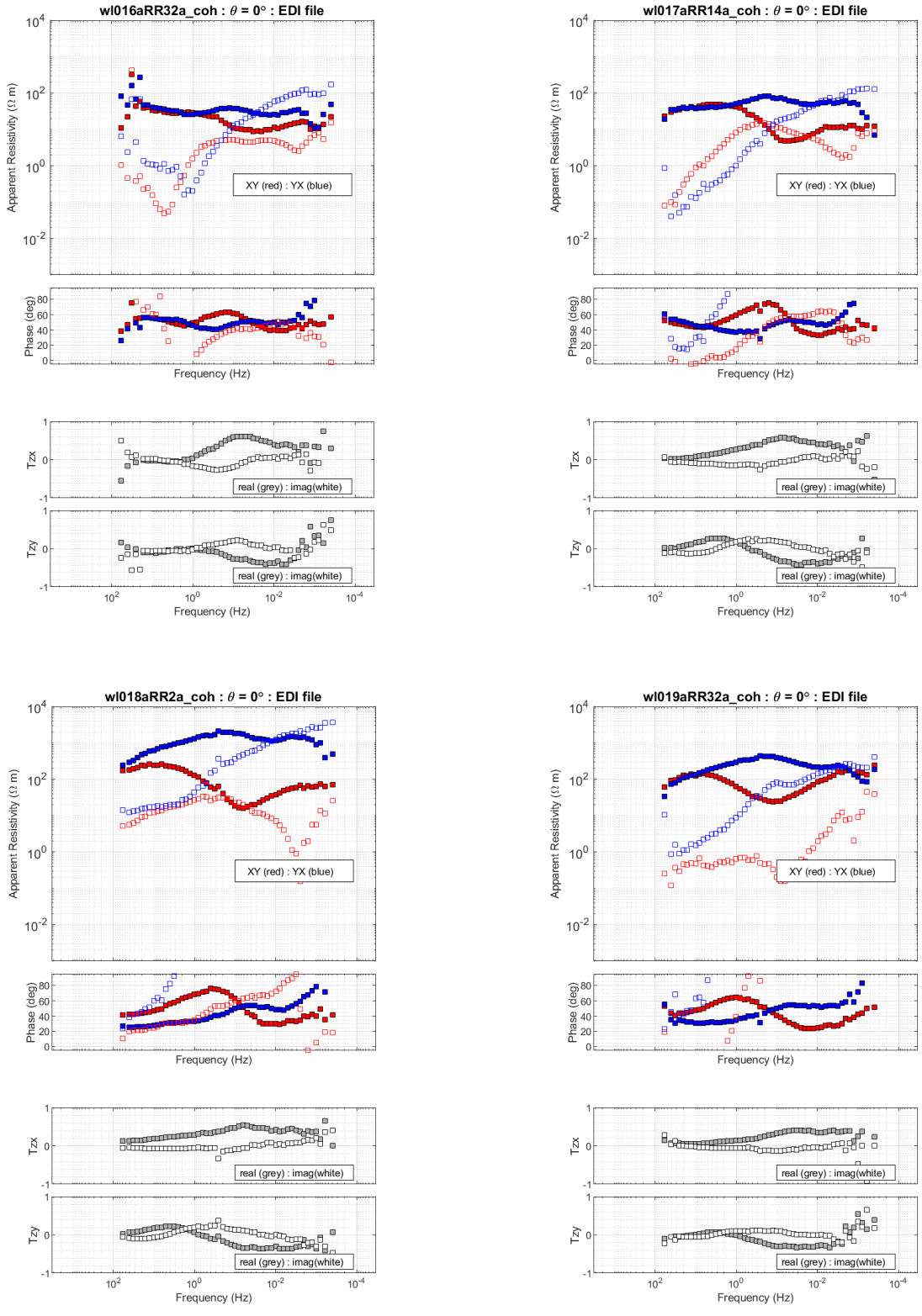

Figure A.5: Apparent resistivity, phase, and tipper curves for stations WL016, WL017, WL018, and WL019.

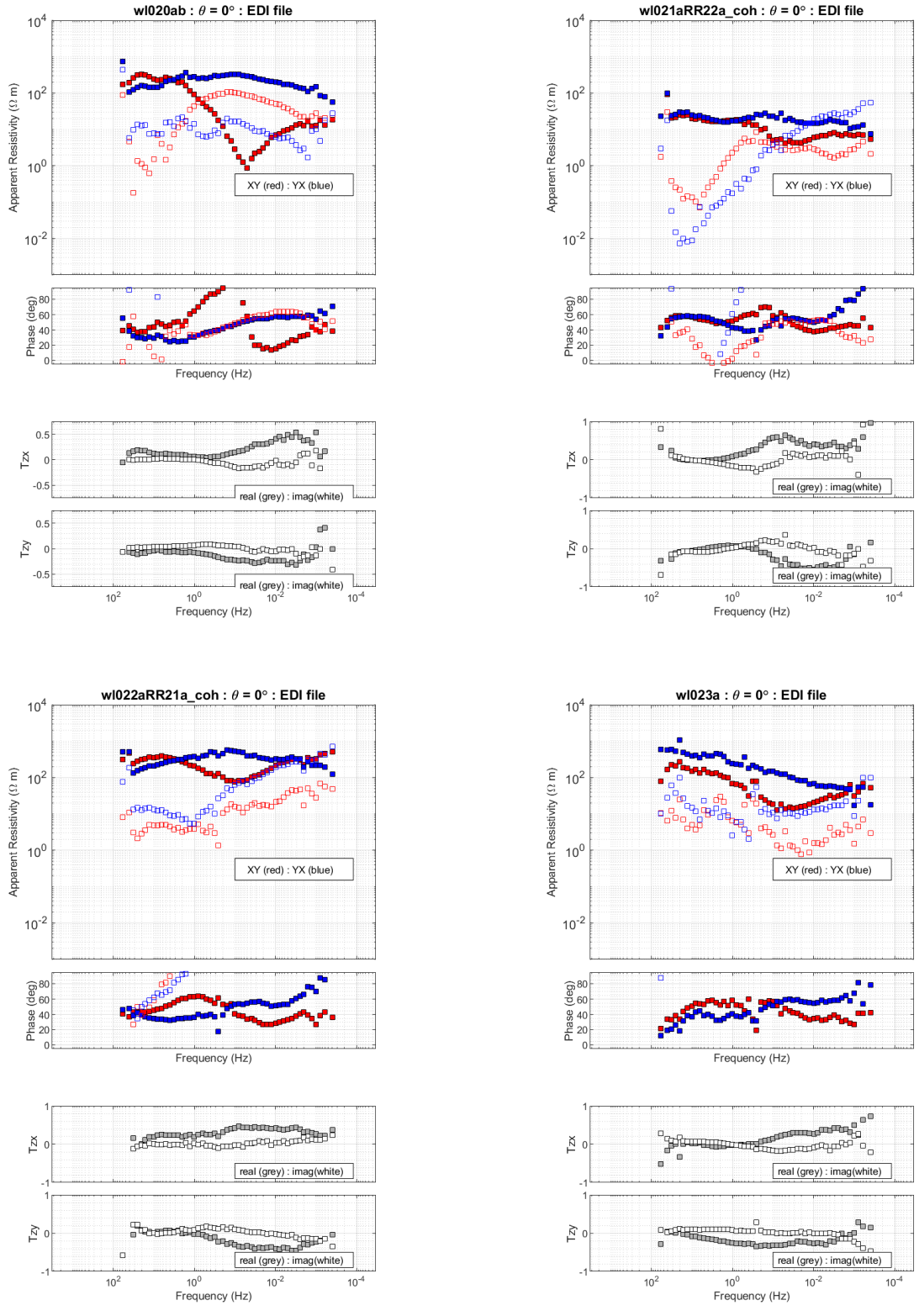

Figure A.6: Apparent resistivity, phase, and tipper curves for stations WL020, WL021, WL022, and WL023.

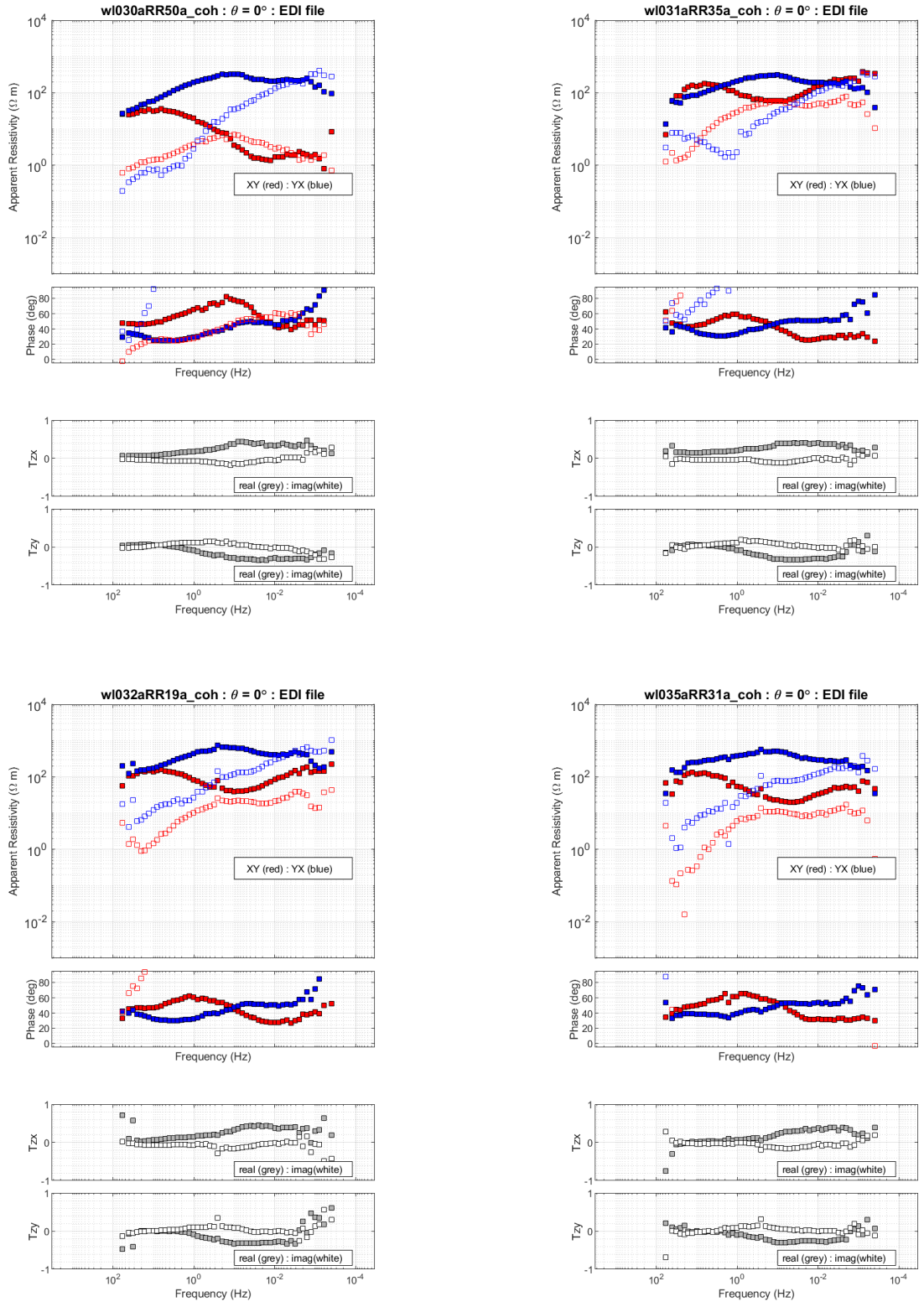

Figure A.7: Apparent resistivity, phase, and tipper curves for stations WL030, WL031, WL032, and WL035.

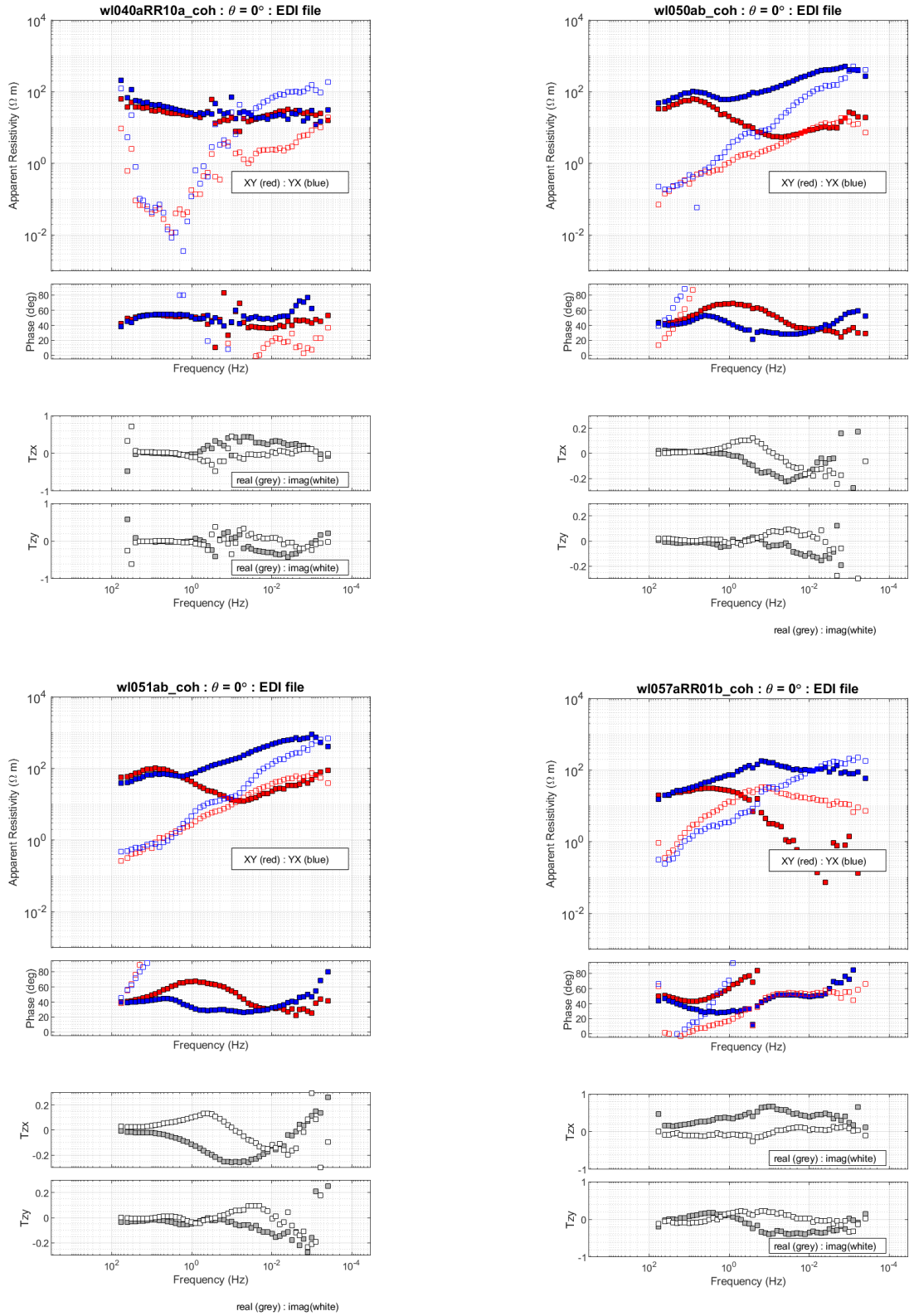

Figure A.8: Apparent resistivity, phase, and tipper curves for stations WL040, WL050, WL051, and WL057.

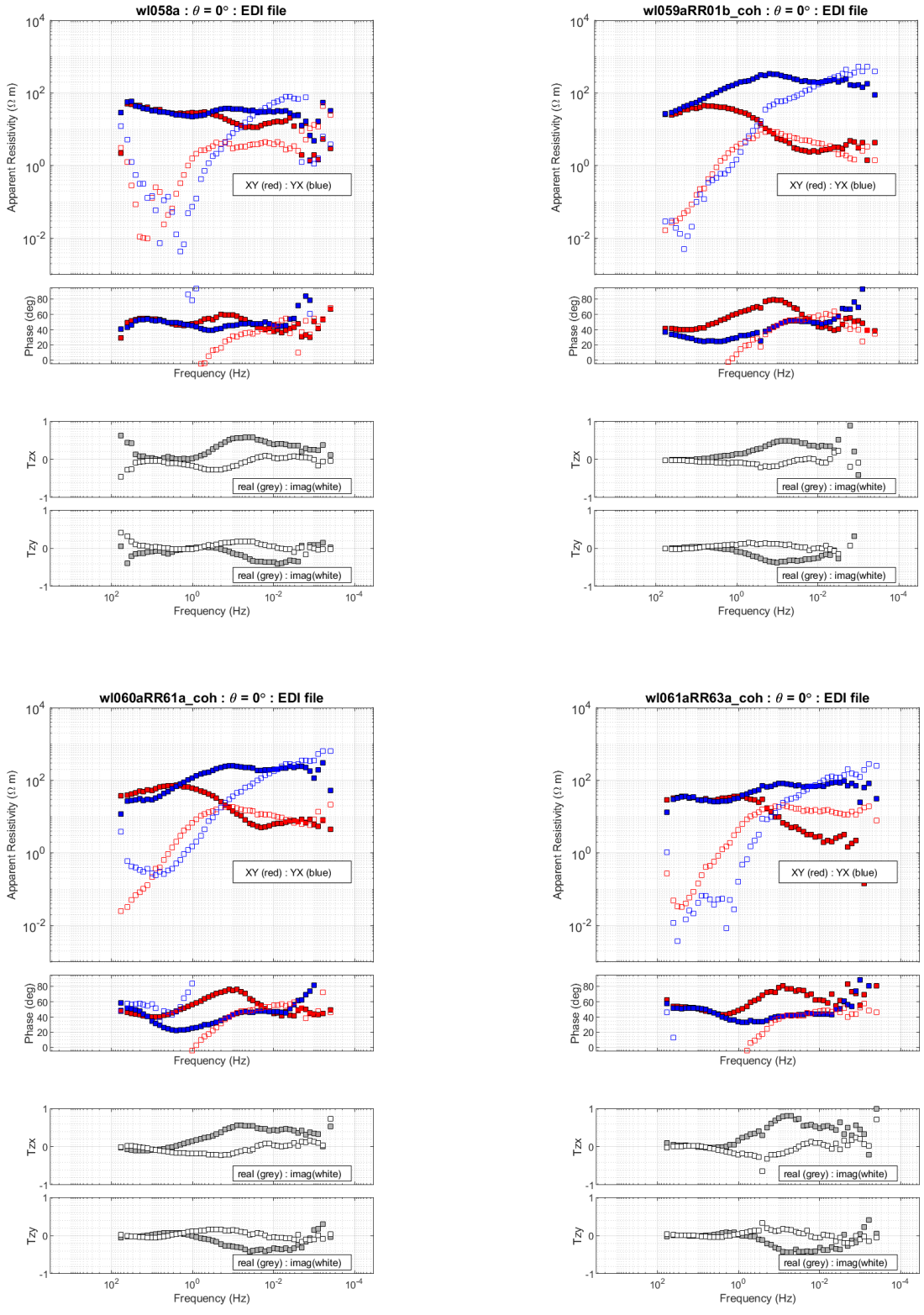

Figure A.9: Apparent resistivity, phase, and tipper curves for stations WL058, WL059, WL060, and WL061.

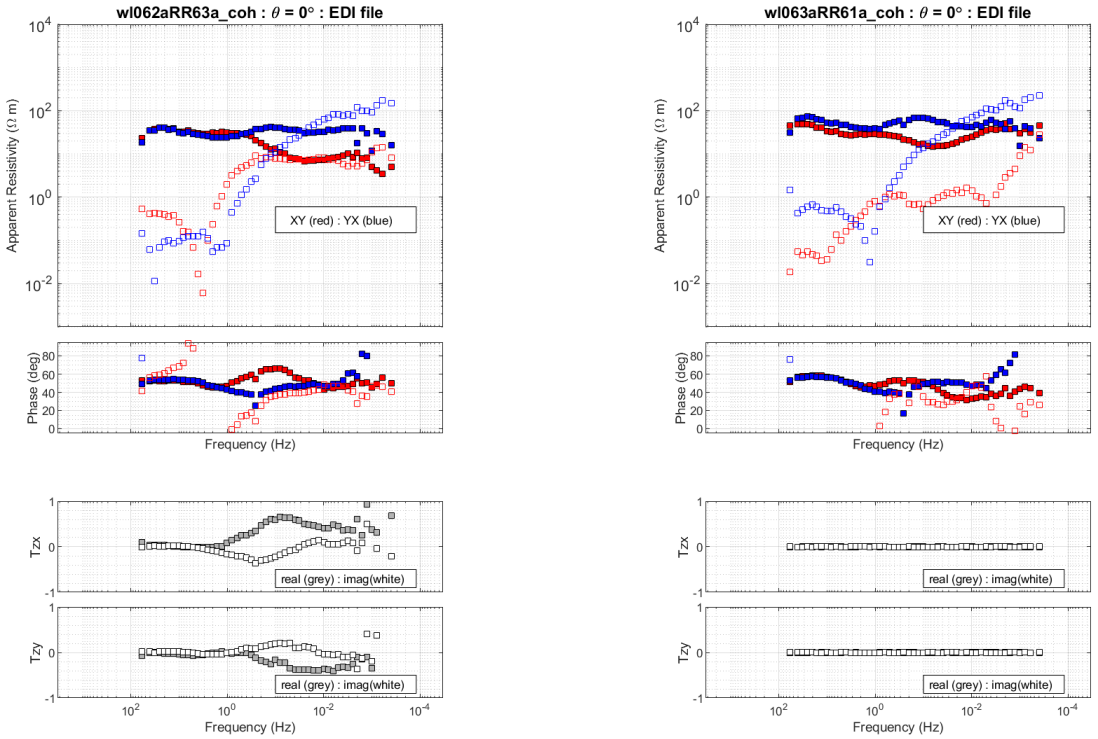

Figure A.10: Apparent resistivity, phase, and tipper curves for stations WL062 and WL063.